Graphene-based Polymer Nanocomposite Hydrogels

A thesis submitted to the University of Sheffield for the award of the degree of Doctor of Philosophy

Yongzhe Piao

Department of Materials Science and Engineering
University of Sheffield

April 2017

Declaration

I declare that I am the sole author of this thesis, and that this thesis has not been submitted to another university in full or in part for another degree or qualification. I declare that the work within this thesis is my own, unless otherwise referenced or acknowledged. Permission has been granted from copyright holders to replicate figures or data within this thesis.

Yongzhe Piao,

April 2017

Acknowledgements

First of all, I would like to sincerely thank my supervisor, Dr. Biqiong Chen, for her valuable advices, guidance, discussions and continued support throughout my doctoral study. I really appreciate the University of Sheffield for granting me the stipend, also allowing me to access to the facilities for my research work. I would like to thank my colleagues in our research group who have helped me with my research, in particular, Justin Richard, Martin Frydrych and Tongfei Wu during my Ph.D. study. I would like to thank my brother, Xuezhe Piao, and some friends in Sheffield for their support. Finally, I would like to thank my dear wife, Wenhong Zhang, who has been fully encouraged and supported me with her heart, and wish her to recover soon from the current illness.

I give great thanks to all the staff of the Department of the Materials Science and Engineering who have been very kind and supportive during my study at the University of Sheffield, specifically to the technical staff for their technical support. I would like to thank Dr. Nik Reeves-McLaren, Dr. Le Ma, Miss Dawn Bussey, Ms Beverley Lane, Mr Ben Palmer, Dr. Peng Zeng and Dr. Peter Korgul for your assistance in testing and characterisation. I would like to thank Dr. Oleksandr Mykhaylyk of the Department of Chemistry, who assisted me with rheometry at the beginning of my work. I would like to thank Ms Susan Bradshaw and Dr. Simon Thorpe of the Department of Chemistry, who undertook the NMR spectroscopy and Mass Spectrometry within this thesis. I would like to thank Tongfei Wu, for assisting me for synthesising dendrimers used in Chapter 5.

Abstract

As unique soft materials, hydrogels have received remarkable attention, due to their high water content and flexibility of materials design that make them able to well mimic biological tissues. This PhD project focused on the development of strong hydrogels for potential biomedical applications. Four types of novel nanocomposite hydrogels were prepared, characterised and studied in depth, namely graphene oxide (GO)-gelatin nanocomposite hydrogels, reduced graphene oxide (RGO)-gelatin nanocomposite hydrogels, GO-polyamidoamine (PAMAM) dendrimer nanocomposite hydrogels and double crosslinked GO-gelatin nanocomposite hydrogels.

GO-gelatin nanocomposite hydrogels were synthesised by self-assembly *via* physical crosslinking bonds (namely, electrostatic interaction and hydrogen bonding). This technique avoided using any organic crosslinking agents, and thus would benefit a high biocompatibility. The hydrogels showed good mechanical properties, thanks to multiple crosslinking sites on GO nanosheets and gelatin chains, exhibiting a relatively high storage modulus of up to 114.5 kPa. Drug release tests showed that the drug release from the GO-gelatin nanocomposite hydrogel was pH-dependent.

RGO-gelatin nanocomposite hydrogels were further prepared from physically crosslinked GO-gelatin nanocomposite hydrogels *via* a facile one-pot synthesis, again without using an organic crosslinker. In this synthesis, gelatin acted as a reducing agent to convert GO to RGO and consequently was chemically grafted onto the adjacent RGO surfaces. The resultant chemically crosslinked RGO-gelatin nanocomposite hydrogels showed a significant increase in the storage modulus, 50% higher than that of GO-gelatin nanocomposite hydrogels with the same original composition. Chemically crosslinked RGO-gelatin nanocomposite hydrogels

demonstrated an enzyme-favourite degradation, which lost up to 29% of their original weight after degradation for 24 h, compared to 17% without enzyme.

GO-PAMAM dendrimer nanocomposite hydrogels were developed using a similar method to that for physically crosslinked GO-gelatin nanocomposite hydrogels. GO-PAMAM dendrimer nanocomposite hydrogels showed a significantly improved mechanical performance and self-healing property. Both GO and PAMAM dendrimer possess abundant functional groups which can induce multiple strong crosslinking networks. The highest storage modulus was 284 kPa, that is, 2.5 times of that for GO-gelatin nanocomposite hydrogels. The storage modulus of the GO-PAMAM dendrimer nanocomposite hydrogels increased with increasing GO or polymer concentration, but GO provided a higher modulus than PAMAM dendrimers at a comparable concentration.

To develop mechanically strong hydrogels, the double crosslinked GO-gelatin nanocomposite hydrogels were synthesised through a one-pot synthesis. Gelatin was crosslinked by two crosslinking agents, glutaraldehyde (GTA) and GTA modified GO sheets, at a low water content (90 wt.%) which was much lower compared to the above nanocomposite hydrogels. In contrast to the neat gelatin hydrogel, double crosslinked GO-gelatin hydrogels exhibited significant improvements in mechanical properties, for instances, by up to 288% in compressive strength and 160% in shear storage modulus. That was ascribed to the novel double crosslinked network structure in which GTA-grafted GO sheets function as multifunctional crosslinking agents. While the mechanical strength increased with increasing crosslink degree, the swelling capability of double crosslinked GO-gelatin hydrogels decreased.

The results show that the graphene-based nanocomposite hydrogels could have potential in soft tissue engineering and drug delivery.

Contents

Declaration ……... i

Acknowledgements …… ii

Abstract …….. iii

List of abbreviations …….. ix

List of symbols ……. xii

List of figures ……... xiv

List of schemes ……..... xxi

List of tables …… xxii

List of publications ……. xxiii

Chapter 1. Introduction ……... 1

Chapter 2. Literature review ……... 4

2.1 Introduction …… 4

2.2 Covalently bonded hydrogels …… 4

2.2.1 Double network hydrogels …….. 5

2.2.2 Slide-ring gels …… 7

2.2.3 Microsphere reinforced composite hydrogels ……... 9

2.2.4 Tetra-poly(ethylene glycol) hydrogels …… 12

2.2.5 Other covalently crosslinked tough hydrogels ……. 14

2.3 Physically crosslinked hydrogels ……... 15

2.3.1 Nanocomposite hydrogels ……. 15

2.3.2 Hydrophobic association hydrogels …….. 18

2.3.3 Other physically crosslinked hydrogels ……... 20

2.4 Graphene-polymer nanocomposite hydrogels ……. 25

2.4.1 Graphene and graphene oxide (GO)..... 25

2.4.2 Graphene (or RGO) based hydrogels 29

2.4.3 Graphene oxide based hydrogels 31

2.5 Gelatin and graphene-gelatin nanocomposite 33

2.5.1 Introduction to gelatin 33

2.5.2 Graphene-gelatin nanocomposite and hydrogels 34

2.6 Polyamidoamine dendrimer-based hydrogels and hybrids 35

2.6.1 Introduction to polyamidoamine (PAMAM) dendrimer 35

2.6.2 Graphene-PAMAM dendrimer nanocomposite and hydrogels 36

2.7 Other graphene-cationic polymer nanocomposites and hydrogels 37

2.8 Summary 38

Chapter 3. Self-assembled graphene oxide-gelatin nanocomposite hydrogels 39

3.1 Introduction 39

3.2 Experimental section 40

3.2.1 Materials 40

3.2.2 Preparation of graphene oxide 40

3.2.3 Preparation of GO-gelatin nanocomposite hydrogels 41

3.2.4 Structural characterisation 41

3.2.5 Rheological measurements 42

3.2.6 *In vitro* drug release tests 43

3.3 Results and discussion 44

3.3.1 Structure and properties of GO-graphene nanocomposite hydrogels. 44

3.3.2 Gelation mechanisms of GO-gelatin nanocomposite hydrogels 58

3.3.3 pH-sensitive drug release behaviour of GO-gelatin nanocomposite hydrogels 61

3.4 Conclusions 64

Chapter 4. Reduced graphene oxide-gelatin nanocomposite hydrogels 66

4.1 Introduction 66

4.2 Experimental section 67

4.2.1 Materials 67

4.2.2 Preparation of RGO-gelatin nanocomposite hydrogels 67

4.2.3 Structural characterisation 68

4.2.4 Rheological measurements 69

4.2.5 Swelling tests 69

4.2.6 *In vitro* Biodegradation 69

4.3 Results and discussion 70

4.4 Conclusions 87

Chapter 5. Graphene oxide-polyamidoamine dendrimer nanocomposite hydrogels 89

5.1 Introduction 89

5.2 Experimental section 89

5.2.1 Materials 89

5.2.2 Preparation of PAMAM dendrimer G4.0 90

5.2.3 Preparation of GO-PAMAM nanocomposite hydrogels 90

5.2.4 Structural characterisation 91

5.3 Results and discussion 92

5.3.1 Characterisation of PAMAM dendrimer G4.0 92

5.3.2 Characterisation of GO 95

5.3.3 Characterisation of GO-PAMAM nanocomposite hydrogels 97

5.4 Conclusions 108

Chapter 6. Double crosslinked graphene oxide-gelatin hydrogels 109

6.1 Introduction ……... 109

6.2 Experimental section …… 110

6.2.1 Materials …….. 110

6.2.2 Preparation of GO-gelatin hydrogels …….. 110

6.2.3 Structural characterisation …… 111

6.2.4 Compression tests …… 111

6.2.5 Rheological measurements …….. 111

6.2.6 Swelling tests ……... 112

6.3 Results and discussion …….. 112

6.4 Conclusions ……... 124

Chapter 7. Overall conclusions and suggestions for future work ……... 126

7.1 Overall conclusions ……... 126

7.2 Suggestions for future work …….. 128

Bibliography ……... 130

Appendix 1. Supplemental figures …… 155

List of abbreviations

AA	Acrylic acid
AFM	Atomic force microscopy
AM	Acrylamide
AMPS	2-acrylamido-2-methylpropane sulfonic acid
ASAP	Sodium polyacrylate
C18	Stearyl methacrylate
C22	Dococyl acrylate
ca	circa
CNC hydrogel	Covalently crosslinked nanocomposite hydrogel
CNSs	Clay nanosheets
DGI	Dodecylglyceryl itaconate
DN	Double network
D-NC hydrogel	Poly(N,N-dimethylacrylamide)-clay nanocompsite hydrogel
dsDNA	Double stranded DNA
EDA	Ethylenediamine
FT-IR	Fourier transform infrared spectroscopy
GGHs	Graphene oxide-gelatin nanocomposite hydrogels
GO	Graphene oxide
GTA	Glutaraldehyde
HA	Hydrophobic association
HRM	Hydrophilic reactive microgel
iPR-C	The ionic carboxyl groups on the polyrotaxane crosslinkers
MMC hydrogel	Macromolecular microsphere composite hydrogel

MPTC	3-(methacryloylamino)propyl-trimethylammonium chloride
MS	Mass spectrometry
NaSS	Sodium p-styrenesulphonate
NC	Nanocomposite
NIR	Near-infrared
NM	Nanomicelle
NMR	Nuclear magnetic resonance spectroscopy
NOCC	N,O-carboxymethyl chitosan
OP-4-AC	Octyl phenol polyethoxy (4) ether acrylate
OP-7-AC	octylphenol polyoxyethylene (7) ether acrylate
OP-10-AC	Alkylphenol polyoxyethylene (10) ether
PA	Polyampholyte
PAA	Poly(acrylic acid)
PAM	Polyacrylamide
PAMAM	Polyamidoamine
PAMPS	Poly(2-acrylamido-2-methylpropanesulfonic acid)
PDGI	Polymetric-dodecylglyceryl itaconate
PDMS	Polydimethylsiloxane
PEG	Poly(ethylene glycol)
PEDOT	Poly(3,4-ethylenedioxythiophene)
PMAA	Poly(methacrylic acid)
PMMA	Poly(methyl methacrylate)
pMIC	Peroxidised micelles initiated and crosslinked
PNIPA	Poly(N-isopropylacrylamide)
PR	Polyrotaxane

PVA	Poly(vinyl alcohol)
γ -CD	γ -cyclodextrin
RGO	Reduced graphene oxide
RN hydrogels	Poly(N-isopropylacrylamide) hydrogels
SANS	Small-angle neutron scattering
SDS	Sodium dodecyl sulfate
SEM	Scanning electron microscopy
SLS	Static light scattering
SR	Swelling ratio
SR gel	Slide-ring gel
ssDNA	Single stranded DNA
TA-PEG	Tetra-amine-terminated PEG
Tetra-PEG	Tetra-poly(ethylene glycol)
TGA	Thermogravimetric analysis
TN-PEG	Tetra-NHS-glutarate-terminated PEG
tP-NC hydrogels	Tetra-PEG based nanocomposite hydrogels
XRD	X-ray diffraction

List of symbols

A	Ampere, SI unit of electric current
c	Concentration of the polymer solution
℃	Degree Celsius
δ	Delta, symbol for phase angle
D	Diffusion coefficient
E	Static Young's modulus
E'	Dynamic Young's modulus
g	Gram, often prefixed with m for milli-, or k for kilo-
G	Static shear modulus
G′	Storage modulus
G″	Loss modulus
h	Hour
Hz	Hertz
θ	Theta, symbol for the incident angle of X-ray beam
I_D	Intensity of D band of Raman spectra
I_G	Intensity of G band of Raman spectra
J	Joule
k	Boltzmann constant
K	Kelvin, unit of temperature
L	Thickness of the specimens
λ	Lamda, symbol for wave length
m	Metre, often prefixed with n for nano-, μ for micro-, m for millimetre, or c for centimetre

M	Average molecular weight of the polymer
min	Minute
mol	Mole
M_{eq}	Equilibrium swelling degree
M_t	Swelling degree at time t
mL	Millilitre
N	Crosslinking density of hydrogels
ν	Poisson's ratio
Pa	Pascal, SI unit of pressure
pH	Potential of hydrogen, a logarithmic scale for the acidity or basicity
R	Gas constant
rad	Radian, unit of angle
s	Second
S	Siemens
t	Time
T	Absolute temperature
V	Volt
W	Watt
wt.%	Weight percentage
W_s	Weight of the swollen hydrogel
W_d	Weight of the dried hydrogel

List of figures

Figure 2.1 Schematic of the structure and mechanism resisting crack growth in the PAMPS/PAM DN hydrogel. ξ_{void} and ξ_{ave} are assigned as the mesh size of void and the average mesh size of PAMPS network, respectively. The black arrows refer to the cracks and the hollow arrows indicate the deformation [46] 6

Figure 2.2 Comparison between (a) a conventional chemical gel model and (b) a SR gel model under tensile deformation. The short polymer chains in the conventional chemical gel break gradually by cause of the heterogeneous distribution of crosslinks. The polymer chains of the SR gel can move through crosslinks and then equalise the stress to prevent breaking [65] 8

Figure 2.3 Schematic of an organic/inorganic NC hydrogel. χ is the flexible polymer chains connected to two neighbouring clay sheets. g is the flexible polymer chain with only one end grafted to one clay sheet. D_{ic} is inter-crosslinking distance between the neighbouring clay particles [95] 17

Figure 2.4 Self-healing illustration of the NC hydrogel (D-NC3 indicates poly(N,N-Dimethylacrylamide)-clay hydrogel), (a) before damage, (b) after damage (with several sharp cuts), (c) after self-healed [98] 18

Figure 2.5 Schematic representation of the structural model of HA gels formed by hydrophobic association [100] 19

Figure 2.6 Schematic of the gelation mechanism of the hydrogel, (a) stacked CNSs, (b) homogeneously dispersed CNSs by interaction with ASAP, (c) the

formed hydrogel network by CNSs crosslinking dendritic macromolecules. d-f, Optical images corresponding to the different status of a-c [21] …….. 22

Figure 2.7 Schematic model of a physical polyampholyte hydrogel, (a) a network with strong and weak ionic bonds at original and stretched status. The strong ionic bonds render undamaged backbone of the network upon stretching, whereas, the weak ionic bonds sacrifice to break. (b) The chemical structures of optional cationic monomers of MPTC and DMAEA-Q, and anionic monomers of NaSS and AMPS [123] …….... 25

Figure 2.8 Schematic of all forms of the graphitic materials. Graphene, a 2D primary building material, can be transformed into 0D buckyballs, 1D nanotubes and 3D graphite [124] …… 26

Figure 2.9 Schematic of the structural model of GO [138] ……. 28

Figure 2.10 Formation mechanism proposed for the hydrothermal reduced GO hydrogel [157]…….... 30

Figure 2.11 Schematic of the preparing procedure and gelation mechanism of the GO-DNA hydrogel [170] ……. 32

Figure 2.12 Illustration of the self-healing: (A) the initial free-standing hydrogel, (B) three small blocks (cut with a razor), and (C) the self-healed blocks [170] ……... 33

Figure 3.1 XRD patterns of (a) graphite, (b) graphite oxide and lyophilised GO-gelatin nanocomposites: (c) G10G5H, (d) G10G7.5H and (e) G10G10H, respectively …… 44

Figure 3.2 Tapping mode AFM topographic image and height profile of a single layer of GO which shows the vertical distance is about 1.0 nm …….. 45

Figure 3.3 TGA curves of graphite and GO …… 46

Figure 3.4 FT-IR spectra of (a) graphite, (b) GO, (c-e) lyophilised GO-gelatin hydrogels: (c) G10G5H, (d) G10G7.5H and (e) G10G10H, and (f) gelatin powder ……... 47

Figure 3.5 Raman spectra of (a) graphite, (b) GO, (c-e) lyophilised GO-gelatin nanocomposites (c) G10G5H, (d) G10G7.5H and (e) G10G10H ……. 49

Figure 3.6 SEM images of (a) a lyophilised GO aqueous suspension (10 mg mL^{-1}) (no hydrogel is formed at this concentration), and lyophilised (b) G10G5H, (c) G10G7.5H and (d) G10G10H hydrogels. Orange arrows indicate the gelatin-coated GO sheets and blue arrows show gelatin linking GO sheets together ……... 50

Figure 3.7 Photos of (a) GO-gelatin hydrogel (G10G5H) (pH: ~4.6), which (b) turns to sol when pH > 9.0, and (c) gels again when pH < 9.0. Inner diameter of the bottle: 15 mm ……. 52

Figure 3.8 Storage moduli *G′* (solid) and loss moduli *G″* (hollow) of hydrogels: (A) G10G5H, G10G7.5 and G10G10H …….. 53

Figure 3.9 Storage moduli *G′* (solid) and loss moduli *G″* (hollow) of hydrogels: G6G10H, G8G10H and G10G10H ……... 54

Figure 3.10 (A) Viscosities of the mixtures of an aqueous GO suspension (10 mg mL^{-1}) and a gelatin solution with varying concentration from zero to 4.0 mg mL^{-1}, and of the hydrogels with 5.0, 7.5 and 10 mg mL^{-1} gelatin; the plateau at the initial part of the viscosity curve of G10G10H may be a result of a sliding between the imperfect surface of the hydrogel and one of the parallel plates upon application of a force; (B) The correlation between viscosity and

the concentration of gelatin at the shear rate of 0.8 s^{-1}, derived from the results in Fig. 3.10A. (C) Proposed gelation mechanism of GO-gelatin hydrogels in different stages of gelation; black lines and blue curves indicate GO nanosheets and polymer chains, respectively. Stage I: low gelatin concentration, stage II: medium gelatin concentration forming clusters, and stage III: relatively high gelatin concentration forming a hydrogel …… 60

Figure 3.11 Drug releasing profiles in neutral PBS (pH = 7.4) and acidic HCl solutions (pH = 1.7) …….. 62

Figure 3.12 SEM images of the cross section of the lyophilised hydrogels after immersion in (a) neutral PBS (pH = 7.4) and (b) acidic HCl (pH = 1.7) solutions for 45 h …….. 62

Figure 4.1 FT-IR spectra of (a) graphite, (b) GO, and (c-e) lyophilised RGO-gelatin hydrogels: (c) RGG2H, (d) RGG5H, (e) RGG10H, and (f) gelatin ….. 72

Figure 4.2 Raman spectra of (a) graphite, (b) GO, and (c-e) lyophilised RGO-gelatin hydrogels: (c) RGG2H, (d) RGG5H, and (e) RGG10H. The ratios of I_D/I_G for the hydrogels are also shown in the figure ……. 74

Figure 4.3 XRD patterns of (a) graphite, (b) GO, and (c-e) lyophilised RGO-gelatin hydrogels: (c) RGG2H, (d) RGG5H, (e) RGG10H, and (f) gelatin …...75

Figure 4.4 Tapping mode AFM topographic images of (A) single-layer nanosheets of GO and (B) RGO extracted from RGG10H with the height profile ……. 76

Figure 4.5 UV-Vis absorption spectra of (a) GO and (b) RGO (extracted from RGO-gelatin hydrogel, RGG10H) aqueous suspension at a concentration of 0.1 mg mL^{-1} ……. 77

Figure 4.6 TGA curves of (a) GO, (b-d) RGO (extracted from corresponding RGG2H, RGG5H and RGG10H, respectively), and (e) gelatin …… 78

Figure 4.7 Illustration of the evolution of the formation of the hydrogels: (A) RGG2H, (B) RGG5H and (C) RGG10H before and after heat treatment during the hydrogel synthesis. Diameter of the containers: 15 mm ….. 79

Figure 4.8 (A) Storage moduli *G'* (solid) and loss moduli *G''* (hollow), and (B) loss factor tan δ of lyophilised hydrogels …….. 80

Figure 4.9 Storage moduli comparison between the physically crosslinked GO-gelatin nanocomposite hydrogels (G10G5H and G10G10H) and RGO-gelatin nanocomposite hydrogels (RGG5H and RGG10H)……82

Figure 4.10 SEM images of cross-section surfaces of (A) lyophilised GO suspension (10 mg mL^{-1}), (B) lyophilised precursor mixture of RGG2H before gelation (containing 10 mg mL^{-1} GO and 2 mg mL^{-1} gelatin), (C) lyophilised RGG2H, (D) RGG5H, and (E) RGG10H …….. 84

Figure 4.11 (A) Swelling behaviour of a RGO-gelatin hydrogel (RGG10H), and (B) M_t/M_{eq} as a function of time *t* for RGG10H ……..... 86

Figure 4.12 Degradation profiles of the same hydrogel with and without collagenase in PBS solution ……..... 87

Figure 5.1 ^{1}H NMR spectrum of the PAMAM dendrimer G4.0 and peak assignments corresponding to the protons denoted in the fragment of a PAMAM dendrimer ……... 93

Figure 5.2 MALDI-TOF mass spectrum of PAMAM dendrimer G4.0 …….. 94

Figure 5.3 Potentiometric acid-base titration of PAMAM. The forward titration (curve a) and the back titration (curve b) were performed using a 0.1001 M HCl solution and a 0.0999 M NaOH solution, respectively ……. 95

Figure 5.4 Laser scattering particle sizing profiles of (a) graphite powder and (b) GO nanosheets in an aqueous solution, with an inset of the tapping mode AFM topographic image of two layers of GO …….. 96

Figure 5.5 Acid-base titration of GO, using a 0.1001 M HCl solution …….. 97

Figure 5.6 FT-IR spectra of (a) graphite, (b) lyophilised GO and GO-PAMAM nanocomposite hydrogels: (c) G10D1H, (d) G10D5H, (e) G10D10H, (f) G10D20H, (g) G10D30H, and (h) neat PAMAM dendrimer …… 98

Figure 5.7 Raman spectra of (a) graphite, (b) lyophilised GO and GO-PAMAM nanocomposite hydrogels: (c) G10D1H, (d) G10D5H, (e) G10D10H, (f) G10D20H, (g) G10D30H, and (h) neat PAMAM dendrimer …… 99

Figure 5.8 XRD traces of (a) graphite, (b) lyophilised GO, and lyophilised GO-PAMAM nanocomposite hydrogels: (c) G10D1H, (d) G10D5H, (e) G10D10H, (f) G10D20H, and (g) G10D30H …… 100

Figure 5.9 SEM images of lyophilised (A) GO suspension and GO-PAMAM nanocomposite hydrogels: (B) G10D1H, (C) G10D5H, (D) G10D10H, (E) G10D20H, and (F) G10D30H ……101

Figure 5.10 (A) G' (solid), G'' (hollow), and (B) tan δ of GO-PAMAM hydrogels: G10D1H, G10D5H, G10D10H, G10D20H and G10D30H …… 104

Figure 5.11 (A) G' (solid), G'' (hollow) and (B) tan δ of GO-PAMAM hydrogels: G6D20H, G8D20H and G10D20H …… 106

Figure 6.1 FT-IR spectra of the lyophilised (a) GO, (b) GH0, (c) GH1, (d) GH5, (e) GH10, (f) GH30, (g) GH50, and (h) neat gelatin …… 113

Figure 6.2 FT-IR spectra comparison of (a) GO and (b) GTA surface-modified GO …….. 114

Figure 6.3 SEM images of lyophilised GO-gelatin nanocomposite hydrogels: (a) GH0, (b) GH1, (c) GH5, (d) GH10, (e) GH30 and (f) GH50……. 116

Figure 6.4 Compressive stress-strain curves of hydrogels: GH0, GH1, GH5, GH10, GH30 and GH50 ……. 118

Figure 6.5 Compressive tangent modulus versus compressive strain of hydrogels: GH0, GH1, GH5, GH10, GH30 and GH50 …… 119

Figure 6.6 (A) *G′* (solid), (B) *G″* (hollow) and (C) damping factor tan δ of hydrogels: GH0, GH1, GH5, GH10, GH30 and GH50 …… 120

Figure 6.7 Equilibrium swelling of the double crosslinked GO-gelatin nanocomposite hydrogels with various GO contents: GH0, GH1, GH5, GH10, GH30 and GH50…….. 124

List of schemes

Scheme 4.1 Illustration of the proposed main chemical reactions and physical interactions between GO nanosheets and gelatin to produce a RGO-gelatin hydrogel …… 71

Scheme 4.2 Illustration of the hydrogel formation process ……. 73

Scheme 5.1 Illustration of 3D-network GO-PAMAM nanocomposite hydrogel formed mainly by the electrostatic interactions between the deprotonated carboxyl groups of GO and protonated amino groups of PAMAM 102

Scheme 6.1 The proposed chemical reaction between GO and GTA …….. 115

Scheme 6.2 The proposed schematic structure of double crosslinked GO-gelatin nanocomposite hydrogels. Here, double crosslinkers refer to GTA and GTA-modified GO. As the physical interactions are weaker than the two chemical crosslinks, they are not considered in the term of double crosslinks ……. 115

List of tables

Table 1.1 Mechanical properties of some biological tissues…….. 1

Table 3.1 Crosslinking densities and number average molecular weights of polymer chains between the crosslinking sites in the hydrogels with varying composition ……. 57

Table 4.1 Crosslinking densities and number average molecular weights of polymer chains between the adjacent crosslinking sites in the RGO-gelatin hydrogels with varying compositions ……. 82

Table 5.1 Rheological and crosslinking data of GO-PAMAM nanocomposite hydrogels ……... 107

Table 6.1 Compressive properties of the double crosslinked GO-gelatin nanocomposite hydrogels……..... 119

Table 6.2 *N* and $\overline{M}_c$ in the double crosslinked GO-gelatin nanocomposite hydrogels with different compositions ……... 122

Table 7.1 Mechanical properties of the prepared different hydrogels and their potential applications…… 128

List of publications

Publications resulted from the thesis:

1. Yongzhe Piao and Biqiong Chen, Self-assembled graphene oxide-gelatin nanocomposite hydrogels: characterization, formation mechanisms, and pH-sensitive drug release behaviour, Journal of Polymer Science: Polymer Physics, 2015, vol. 53, pp. 356–367.
2. Yongzhe Piao and Biqiong Chen, One-pot synthesis and characterization of reduced graphene oxide-gelatin nanocomposite hydrogels, RSC Advances, 2016, vol. 6, pp. 6171–6181.
3. Yongzhe Piao, Tongfei Wu, and Biqiong Chen, One-step synthesis of graphene oxide-polyamidoamine dendrimer nanocomposite hydrogels by self-assembly, Industrial & Engineering Chemistry Research, 2016, vol. 55, pp. 6113–6121.
4. Yongzhe Piao and Biqiong Chen, Synthesis and mechanical properties of double crosslinked gelatin-graphene oxide hydrogels, International Journal of Biological Macromolecules, 2017, vol. 101, pp. 791-798.

Chapter 1. Introduction

Hydrogels are three-dimensional (3D) networks of hydrophilic polymer chains containing a large number of water molecules [1,2]. They are highly biocompatible due to their inherent physical properties which are very similar to biological tissues [3] and make them attractive materials for biomedical applications [3-5]. As a result, hydrogels have been extensively studied for applications in tissue engineering [6-8], such as cartilage repair, artificial muscles and wound dressing, as well as drug delivery [9-12] and biosensors [13,14]. The mechanical properties of some biological tissues are presented in Table 1.1.

Table 1.1 Mechanical properties of some biological tissues.

Biological tissue	Compressive strength (MPa)	Tensile strength (MPa)	Young's modulus (MPa)	Shear storage modulus (kPa)
Articular cartilage	14-59 [15]	-	0.49 [15]	-
Achilles tendon	50-125 [16]	-	500-1850 [16]	-
Posterior cruciate Ligament	-	26.8-36.4 [17]	109-345 [17]	-
Cornea	-	0.014-0.073 [18]	2.87-3.4 [19]	-
Smooth muscle	-	0.013-0.178 [20]	1.3 [21]	-
Skin	-	-	0.42-0.85 [22]	325.0-1227.9 [23]
Adipose tissue	-	-	0.0003-0.024 [24]	7.5 [25]

Hydrogels are commonly divided into two groups according to the type of driving forces to form the hydrogels, i.e., covalently bonded hydrogels and physically crosslinked hydrogels. However, there are still two issues which limit their usages: weak mechanical properties and inability of self-healing. As we know, in nature, many biological tissues and organs can self-heal upon damage. To

overcome the mechanical weakness of hydrogels, four outstanding strategies were reported: slide-ring gel (SR gel), double network hydrogel (DN hydrogel), tetra-poly(ethylene glycol) hydrogel (tetra-PEG gel) and microsphere reinforced composite gel [26,27]. These hydrogels show high mechanical strength and rubberlike properties, but they are not capable of self-healing after damage, due to their irreversible covalent bonds. So, physically crosslinked hydrogels were considered as a more promising solution to solve the two issues mentioned above, compared to covalently bonded hydrogels [28,29].

To develop physically crosslinked hydrogels with high mechanical performance, several different approaches were reported [30-32]. Back to 2002, Haraguchi [30] reported a type of nanocomposite hydrogels (NC hydrogels) which made significant improvement in mechanical performance. Since then, various NC hydrogels have been developed [31,33,34]. Furthermore, Wang and co-workers [32] reported a hydrogel consisting of dendritic macromolecule and clay nanosheets with improved mechanical properties and self-healing capability. However, design and preparation of physically crosslinked hydrogels with both excellent mechanical properties and self-healing capability were still technical challenges.

Graphene and graphene oxide (GO) based materials have been widely studied for numerous engineering and biomedical applications [35-38]. This PhD project aims to develop new types of graphene based nanocomposite hydrogels with good biocompatibility, high mechanical performance and ideally capability to self-heal after damage, which could be used for drug delivery, tissue repair and wound healing. Biocompatible hydrophilic polymers and strong and flexible atom-thick graphene sheets were used to achieve the desired hydrogels, benefiting from their instinct

biocompatibility, excellent mechanical properties of graphene [39] or GO [40], and their optimised 3D network structures. The specific objectives are outlined below:

- To develop physically crosslinked GO-gelatin nanocomposite hydrogels by a simple self-assembly process and without the usage of a toxic organic crosslinking agent, study their formation mechanisms, investigate the GO effect on their mechanical properties and study their performance on drug delivery.
- To prepare reduced graphene oxide-gelatin nanocomposite hydrogels by a green and facile method avoiding any chemical crosslinking agents and organic solvents, study their gelation mechanisms, and investigate their mechanical, swelling and degradation behaviour.
- To develop physically crosslinked GO-polyamidoamine dendrimer nanocomposite hydrogels with excellent mechanical properties by a facile one-step self-assembly method without using any chemical crosslinkers, study their formation mechanisms and mechanical and self-healing performance.
- To develop double crosslinked GO-gelatin nanocomposite hydrogels with superior mechanical properties using one-pot synthesis and a chemical crosslinker, study their gelation mechanisms and investigate the structure-property relationships.

These studies are expected to advance the field of graphene-based polymer nanocomposite hydrogels, and the novel hydrogels developed may find potential applications in tissue repair, injectable therapy and pH-controlled drug delivery.

Chapter 2. Literature review

2.1 Introduction

Hydrogels are composed of water-insoluble network of crosslinked polymer chains, which have distinctive features, *e.g.*, high water content, excellent biocompatibility and osmotic properties [41-43]. Since Kuhn reported swelling hydrogels in 1949 [44], great interests on hydrogel research have emerged.

The massively studied hydrogels can be classified into many different groups: one of them is superabsorbent hydrogels that are mostly fabricated by employing monomers of acrylic acid and acrylamide [45], having wide applications in hygienic, agriculture and bio-related areas. Another group of hydrogels, which possess excellent optical properties, have been studied for intraocular lens materials [46] and photonics researches when the hydrogels have periodic nanostructure [47]. In recent years, more and more researches have been exploring hydrogels for biomedical applications [48], including medical and biological sensors [49], controlled drug-delivery systems [50], diagnostic imaging [51], tissue repair [52,53], etc.

2.2 Covalently bonded hydrogels

Covalently bonded hydrogels have relatively high mechanical properties owing to the intrinsic strong networks. These hydrogels are commonly fabricated by polymerisation of the monomers with an organic crosslinking agent. However, in general, organic crosslinking agents are toxic to human organs and difficult to be completely eliminated from hydrogels [54]. Moreover, covalently bonded hydrogels show their limitation in the applications of load-bearing medical devices and strong tissue scaffolds. That is mainly ascribed to weak mechanical properties caused by the

inhomogeneous structure and poor crosslinking length distribution in the hydrogels [55]. Therefore, vast research have been exploring on the hydrogels with high mechanical properties. Some approaches were reported such as the DN hydrogels, the SR gels and the tetra-PEG hydrogels, which are discussed below.

2.2.1 Double network hydrogels

Gong and co-workers [56] first reported DN hydrogels comprising of two interpenetrating polymer networks with various hydrophilic polymers, which exhibited an extremely high mechanical performance, fracture strength as high as dozens of megapascals and high wear resistance. Among several optimal combinations, the poly(2-acrylamido-2-methylpropanesulfonic acid) (PAMPS)-polyacrylamide (PAM) hydrogel comprised of the first network of PAMPS and the second network of PAM. The PAMPS-PAM hydrogel had a compressive fracture strength of 17.2 MPa with 90 wt.% water content [56]. One of two crucial conditions to obtain high toughness of the hydrogel is the optimal combination of the highly crosslinked first network of rigid polyelectrolyte (PAMPS) and the linear or loosely crosslinked (or non-crosslinked) second network (PAM) of flexible neutral polymer [56]. When a crack occurs in a hydrogel, the crack energy can be absorbed by the second network, preventing the crack growth [57]. The mesh size (ξ_{void}) of PAM network void is larger than the average mesh size (ξ_{ave}) of PAMPS network (as shown in Fig. 2.1). The second crucial condition is the optimal molar ratio of the second network monomer to the first network monomer, which falls in a range of several to decades [56]. This molar ratio range distinguished from conventional interpenetrating hydrogels, which possess similar contents of two polymers but do not present extremely high mechanical strength [58]. The DN hydrogels with various

polymer combinations were extensively studied by the same group [57,59-67] and were also reviewed in their review articles [68,69], summing up their exceptional properties up to a compressive strength of 20–60 MPa at a strain of 90–95%, an elastic modulus of 0.1–1.0 MPa, a tensile strength of 1–10 MPa at a strain of 1000–2000% and tearing fracture energy of 100–4400 J m^{-2}.

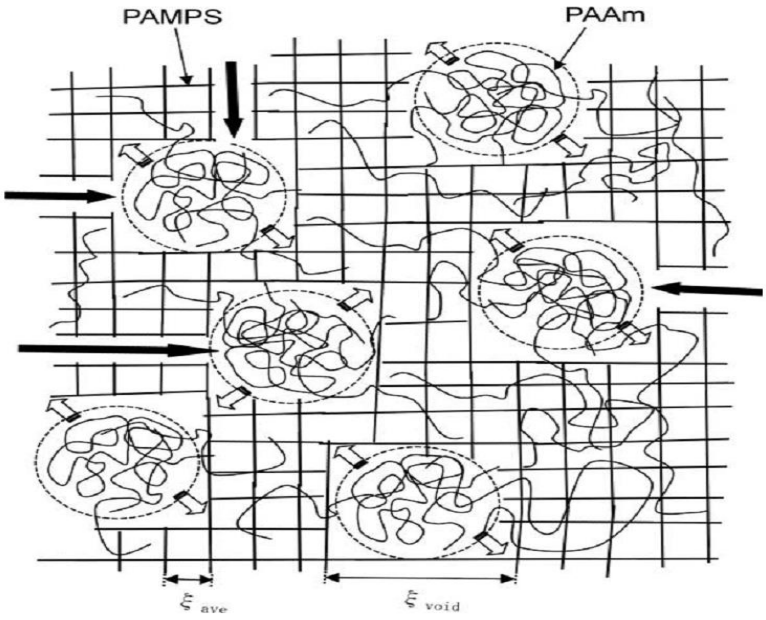

Figure 2.1 Schematic of the structure and mechanism resisting crack growth in the PAMPS/PAM DN hydrogel. ξ_{void} and ξ_{ave} are assigned as the mesh size of void and the average mesh size of PAMPS network, respectively. The black arrows refer to the cracks and the hollow arrows indicate the deformation. Reproduced with permission from [57], copyright (2004) American Chemical Society.

By utilising the similar principle, several tough DN hydrogels were also developed by other groups, such as mechanically strong DN hydrogels from N,N-dimethylacrylamide and glycidyl methacrylated hyaluronan [70], DN hydrogels with two biocompatible polymers: poly(vinyl alcohol) (PVA)-PEG hydrogels [71] and agarose and PEG diacrylate hydrogels [72], conducting hydrogels composed of PAM and poly(3,4-ethylenedioxythiophene)-poly(styrenesulfonate) [73], DN hydrogels

consisting of oxidised dextran and thiolated chitosan [74], and jellyfish (*Rhopilema esculenta Kishinouye*)-poly(acrylic acid) (PAA) hybrid hydrogels [75]. However, DN hydrogels exhibit a poor fatigue resistance, owing to the irreversibility of covalent bonds [68].

2.2.2 Slide-ring gels (SR gels)

Okumura et al. [76] reported a new topological hydrogel (defined as SR gel) made up of crosslinked polyrotaxane (PR) that comprised of long PEG chains threaded with cyclic α-cyclodextrins (α-CD) and capped with bulky groups at the ends [76]. Precisely speaking, it is the α-CDs that are chemically bonded to form α-CD dimers, figure-of-eight crosslinks, acting as linkages between PRs. These SR gels are topologically interlocked by α-CD dimers and the dimers can move along the PEG chains freely, hence upon loading the created tension of the PEG chains can be equalised, not only in isolated single chains, but also throughout the whole network. This phenomenon distinguishes from the conventional chemical gels, in which the polymer chains steadily break due to the localised stress resulting from heterogeneity of their polymer network, illustrated in the Fig. 2.2. This SR gel showed exceptional properties, such as high swelling ratio (ca 400), an optical transmittance of 95% [76], a high elongation at break of up to 24 times in length without hysteresis, a tensile strength of over 100 kPa [77], as well as 500 Pa for the shear modulus [76]. The structural studies on the SR gel using small-angle neutron scattering (SANS) and small-angle X-ray scattering show a solvent-dependent pulley effect, that is, the pulley effect is active in a good solvent, whereas inactive in a poor solvent [78,79]. The SR gel exhibits a J-shaped curve in the stress-strain plot in contrast to the S-shaped curve for a conventional chemical gel [77]. The SR gel membrane has the

ability to control fluid permeation by a fashion of on-off switch by changing the imposed pressure, which could be promising materials for separation membranes and novel drug delivery [80].

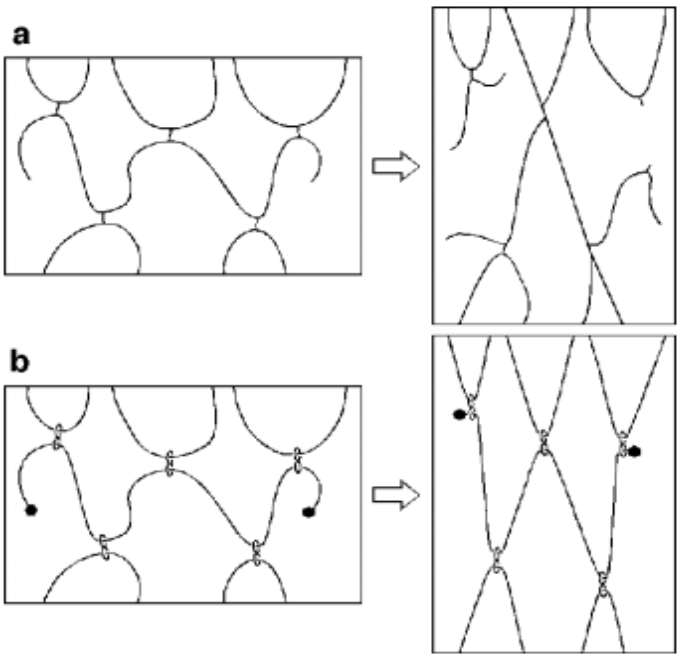

Figure 2.2 Comparison between (a) a conventional chemical gel model and (b) a SR gel model under tensile deformation. The short polymer chains of the conventional chemical gel break gradually by cause of the heterogeneous distribution of crosslinks. The polymer chains of the SR gel can move through crosslinks and then equalise the stress to prevent breaking. Reproduced with permission from [76], copyright (2001) John Wiley and Sons.

Exploiting the principle of SR gels, Ito's group developed a couple of different hydrogels by using various materials and approaches. A novel SR gel was synthesised by crosslinking PRs which consisting of inorganic poly(dimethylsiloxane) (PDMS) and organic γ-cyclodextrin (γ-CD) [81]. Successful synthesis of this SR gel provided a new route to achieve organic-inorganic hybrid materials. The group also developed new SR gels [82], in which the crosslinking

agent was PR modified with vinyl. The PR, containing a-cyclodextrin (α-CD), was modified by 2-acryloyloxyethyl isocyanate providing vinyl groups to the α-CD of the PR to become the crosslinker. Poly(N-isopropylacrylamide) (PNIPA) gels (RN gels) were synthesised by polymerisation of NIPA monomer in the presence of active modified-PR. This method to prepare RN gels could be applied to various polymer chains. Based on the concept of RN gels, they further incorporated ionic groups to the hydrogel to create extremely stretchable thermo-sensitive PNIPA hydrogels [83]. The ionic carboxyl groups on the polyrotaxane crosslinkers (iPR-C) made them water soluble and become well stretched in the hydrogel. The hydrogels had a maximum stretchability of 1463% and tensile strength of 31.4 kPa. When the iPR-C content was low (< 3 wt.%), the hydrogels exhibited little pH-sensitivity on their swelling behaviour, and the transition temperature was not affected significantly by the ionic groups.

2.2.3 Microsphere reinforced composite hydrogels

To achieve tough hydrogels with homogenous structure, a new tough hydrogel, namely, macromolecular microsphere composite hydrogel (MMC hydrogel) was reported by Huang et al. [84]. The MMC hydrogel was made up of acrylic acid (AA), which was initiated and crosslinked by the pre-peroxidised macromolecular microsphere. The abundant PAA chains grew on the macromolecular microspheres and were chemically crosslinked by them; and some chains with one free end can entangle each other. The abundant PAA chains grafted to the adjacent macromolecular microspheres, along with the additional contribution of strong intermolecular hydrogen bonds between those polymer chains, rendered the high toughness of the MMC hydrogel. The hydrogel showed a compression strength of

78.6 MPa at a strain of 99.3% with 70 wt.% water, which are comparable to an articular cartilage [84]. However, continuous swelling restricts the hydrogel's potential as a successful candidate material for biomedical applications, though a second network was suggested by the authors to solve the problem bearing the principle of the DN hydrogel. The group [85] later reported mechanically strong and thermosensitive MMC PNIPA hydrogels. The optimal hydrogels showed a compression strength higher than 10 MPa (at 95% strain) at about 60 wt.% water content. They [86] also systematically studied the mechanism behind the exceptional toughness of the MMC hydrogels. The results from several mechanical tests reveal that the chemical bonding regulates the compression strength and toughness of MMC hydrogels, whereas the physical interactions including hydrogen bond and chain entanglement mainly account for the modulus of the hydrogels. Furthermore, the disassociation of physical interactions causes energy loss in the network, exhibiting the hysteresis in the cyclic tensile tests.

Adapting the similar strategy of the MMC hydrogel, several hydrogels were reported using various materials or structures as an initiator and a crosslinking centre. For example, He et al. [87] developed a new PAA hydrogel by polymerisation of AA monomer, which was peroxidised micelles initiated and crosslinked (pMIC) instead of macromolecular microspheres. The irradiation-peroxidised micelles (formed from alkylphenol polyoxyethylene (10) ether (OP-10)) first initiated the grafting polymerisation of hydrophilic monomers AA onto them to form microgels; and further polymerisation of monomers AA resulted in the bulk hydrogels. The hydrogels showed a high transparency of 95%, a high compression strength up to 86 MPa and a fracture strain of 95% without break [87]. The hydrogels can recover their original dimensions quickly after off-loading, showing excellent shape recovery.

The pMIC hydrogel is similar to the MMC hydrogel both in microstructure and energy dissipation mechanism. The pMIC hydrogel possesses effective polymer chains with fairly even length between the adjacent micelles, ascribed to the small size and the well distribution of peroxidised micelles in the polymer matrix [87]. Thus, the stress can be equalised among the crosslinked polymer chains upon loading, leading to exceptional mechanical performance. Sun et al. [88] reported super tough nanomicelle (NM) hydrogels with vinyl-functionalised Pluronic F127 micelles as multifunctional crosslinking agents. The NM hydrogels were synthesised by copolymerisation of acrylamide (AM) monomers in the existence of the multifunctional micelles, showing extraordinary mechanical properties. The NM hydrogels exhibited a tensile strength of 276 kPa at a fracture strain above 2265%, and a fracture energy of 2.34 MJ m^{-3} [88]. Moreover, these hydrogels can sustain stress up to 62 MPa (at 98% strain) without fracture [88].

Tan et al. [89] reported high mechanical strength and thermo-responsive PNIPA hydrogels in which starch-based nanospheres acting as crosslinkers. The nanospheres with active allyl groups were formed from acetylated allylic starch. The hydrogels showed a maximum compressive strength of 8.44 MPa and a fracture strain of 89.3% with 90 wt.% water [89]. The hydrogels also exhibited a high thermo-response rate by deswelling almost eight times faster than that of a counterpart conventional hydrogel. Qin et al. [90] reported a hydrophilic reactive microgel (HRM) with high mechanical strength prepared by copolymerisation of AM monomers and crosslinker of 2-acrylamido-2-methylpropane sulfonic acid (AMPS). HRMs were chemically modified by N-methylolacrylamide to obtain active double bonds prior to be used in the hydrogel synthesis. The resulting HRM hydrogels had a high compressive stress up to 4.6 MPa at 90% strain with 93.4 wt.% water; and after the load release, its

deformation could be recovered at room temperature [90]. The hydrogels exhibited excellent tensile properties, *i.e.*, a fracture tensile strength up to 2.55 kPa at a break strain of 323% at a water content of 96.3 wt.% [90]. Wu et al. [91] proposed an approach to fabricate homogeneous MMC-like covalently crosslinked nanocomposite hydrogels (CNC hydrogels) with extraordinary mechanical strength and magnetic property. Free-radical polymerisation was carried out to form the various CNC hydrogels using the monomers, n-vinyl pyrrolidone and AA or AM. Among them, PAM CNC hydrogels demonstrated the highest fracture tensile strength up to 230 kPa and remarkable elongation of 1837% [91]. The additional magnetic property was realised by incorporation of Fe_3O_4 nanoparticles into the polystyrene nanoparticles during the preparation.

2.2.4 Tetra-poly(ethylene glycol) (Tetra-PEG) hydrogels

Sakai et al. [92] produced a novel tough Tetra-PEG hydrogel with a homogeneous structure from symmetrical tetrahedron-like macromonomers, tetra-amine-terminated PEG (TA-PEG) and tetra-NHS-glutarate-terminated PEG (TN-PEG). The tetra-PEG hydrogel obtained a homogeneous network since its nanostructure was determined by the same length of tetra-PEG arms, leading to high mechanical properties. The maximum compressive strength of 9.6 MPa was achieved for the tetra-PEG hydrogels. [92]. To obtain the highest mechanical properties under compression, the optimal molar ratio of the macromonomers was equal and even a small deviation leads to weakening in their mechanical properties. The structure of tetra-PEG gel was investigated by SANS and static light scattering (SLS) experiments [93,94]. No significant scattering was observed to suggest heterogeneity of the crosslinking structure in tetra-PEG gels, giving evidence of extremely uniform structure of tetra-

PEG gels. Only negligible topological defects, such as loops and entanglements, were detected in the tetra-PEG gel, which were different with the conventional hydrogels [95]. The authors suggested this highly homogeneous structure was formed due to three important factors: (1) the tetra-PEG macromolecule's unique behaviour as impenetrable sphere in aqueous solution; (2) one-node and four-chain structure of tetra-PEG macromolecule; and (3) the homogeneous mixing of two tetra-PEG macromolecules facilitated by electrostatic repulsion between the amine-terminated tetra-PEG macromolecules [96]. This ideal structure accounts for its intriguing properties, *i.e.*, a high transparency of ca 100%, a tensile strength of ca 150 kPa at a high stretching elongation at break of ca 900%, a high compressive strength of 27 MPa (whereas half specimens without break), and an average compressive modulus of 99.7 kPa [96].

Fukasawa et al. [97] introduced clay into the gel to prepare tetra-PEG based nanocomposite gels (tP-NC gels) with excellent optical property and high mechanical performance. The authors discovered that the buffer solution for reaction was critical to obtain the homogeneous distribution of the exfoliated clay and had a control on viscosity in the clay suspensions. They found the best option was pyrophosphate-Na buffer. The best mechanical properties were achieved by the following optimal preparative steps: clay suspension was mixed with TA-PEG before mixed with TN-PEG. The tP-NC gels showed a high transparency of 83%, a tensile strength of 300–560 kPa (beyond double the corresponding neat tetra-PEG gel) at a strain of 900–1000% [97].

2.2.5 Other covalently crosslinked tough hydrogels

Appreciating excellent regioselectivity and high yielding of copper-catalysed reaction of azides and terminal acetylenes [98], Malkoch et al. [99] reported a new PEG-based hydrogel prepared by this Click chemistry, possessing well-defined microstructure and high mechanical performance. The hydrogels were synthesised of by cycloaddition reaction of diacetylene-functionalised and tetra-azide-functionalised PEG derivatives in aqueous solutions by copper (I) catalysis. The hydrogels exhibited a high tensile strength of 2.39 MPa and a strain of 1550% [99], which was ascribed to their ideal structure networks. Moreover, remaining azide and acetylene groups were available for further functionalisation of the hydrogel by incorporation of bioactive molecules.

Tough hydrogels containing lamellar bilayer structure were created by Haque et al. [100], which were formed into a plate-like shape by free radical polymerisation of surfactant dodecylglyceryl itaconate (DGI) and AM monomer in the aqueous solution. The polymer matrix of PAM was chemically crosslinked network but no chemical crosslinking between PAM and polymetric-dodecylglyceryl itaconate (PDGI). During the preparation, DGI self-assembled into lamellar bilayers with unidirectional alignment parallel to the top surface of the hydrogel, rendering the gel strong mechanical anisotropy, *i.e.*, a 10-fold elastic modulus in the direction of the lamellar layers compared to that in perpendicular direction. Along with the direction parallel to the bilayers, the ultimate strength of 600 kPa and fracture strain of 2200% were obtained for the PDGI-PAM gel [101]. Since the stacked lamellar bilayers were formed by reversible hydrophobic association, they could dissociate to dissipate the energy upon deformation, showing capability of self-recovery and fatigue resistance, and large hysteresis. Furthermore, crack blunting was formed to effectively inhibit

crack propagation due to lipid-like mobile structure of lamellar bilayers [101]. Interestingly, the periodical oriental stricture of the bilayers induced the PDGI-PAM gel to exhibit structural colour, even reversibly tunable by a controlled manner of applied stress or strain which giving potential applications in advanced stress or strain sensors.

2.3 Physically crosslinked hydrogels

The covalently bonded hydrogels could exhibit relatively high mechanical strength; however, generally they are lack of adaptivity or self-healing and they are non-recyclable. Furthermore, the toxicity of the crosslinker used in the synthetic process may limit their potential in biomedical area. Hence, physically crosslinked hydrogels with excellent mechanical performance and self-healing ability have been drawing vast interest. The physical interactions to form hydrogels include ionic strength, hydrogen bonding, hydrophobic association, π–π stacking interaction, coordination and physical tanglement effect [28,102,103].

2.3.1 Nanocomposite hydrogels

In 2002, Harahuchi and Takehisa [30] first reported high strength nanocomposite hydrogels (NC hydrogels), which were synthesised from NIPA monomer and clay nanosheets. In the hydrogel, clay sheets acted as multifunctional physical crosslinkers. Fig. 2.3 illustrates the organic-inorganic structure of the PNIPA NC hydrogel. The optimised hydrogel exhibited an extraordinary toughness, *i.e.*, a tensile strength of 109 kPa, a modulus of 9.9 kPa and a fracture strain of 857%, which were significantly improved compared to the conventional crosslinked counterpart hydrogel [30]. With highly increased clay content the hydrogels had a

compressive strength up to 5 MPa with a strain of 80% [104]. High mechanical properties were interpreted attributable to the complex combination of ionic interactions between clay, initiator and PNIPA, and also due to homogenous structure of hydrogel as a consequence of well dispersion of clay nanosheets in the initial reaction solution [105]. Unlike in the conventional hydrogel, in the NC hydrogel, the crosslinker density and the chain lengths between crosslinking points are independently controlled [106]. The clay sheets are uniformly distributed in the hydrogel and the distance between adjacent clays (D_{ic}, in Fig. 2.3) is the same as the polymer chain length between the relevant crosslinking points. Liu et al. [33] developed PNIPA-clay hydrogels with a high clay content, obtaining significantly improved mechanical properties (*i.e.*, a tensile strength of 1 MPa and a fracture strain of 1400%). Some other minerals were also used for the development of nanocomposite hydrogels. For example, poly(methacrylamide) nanocomposite hydrogels [107] with water-soluble rigid polysiloxane as the crosslinker, and poly(acrylic acid-co-N-isopropylacrylamide)-hydrotalcite nanocomposite hydrogels using hydrotalcit as the crosslinker [108], were reported.

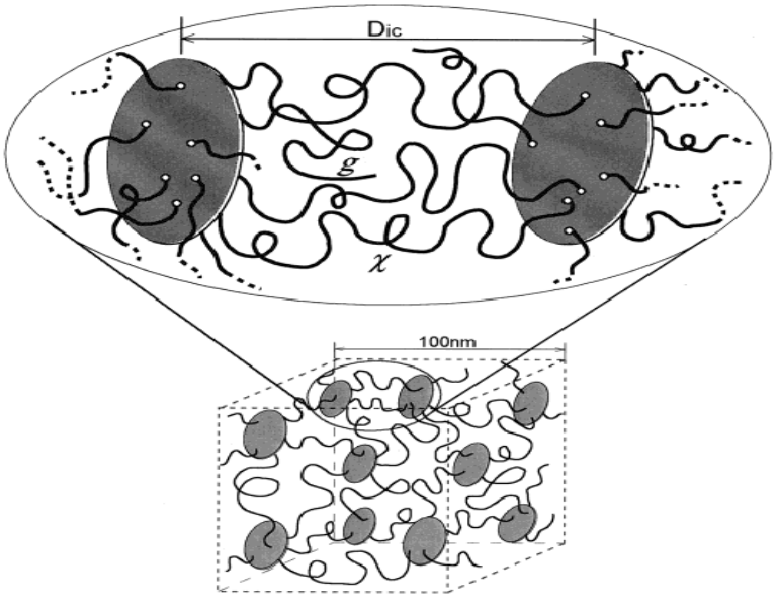

Figure 2.3 Schematic of an organic/inorganic NC hydrogel. χ is the flexible polymer chains connected to two neighbouring clay sheets. g is the flexible polymer chain with only one end grafted to one clay sheet. D_{ic} is inter-crosslinking distance between the neighbouring clay particles. Reproduced with permission from [106], copyright (2002) American Chemical Society.

NC hydrogel is such an extraordinary network not only because of its high transparency and mechanical strength, but also of unique feature of self-healing. Its self-healing materialises by autonomously reconstructing crosslinks across the damaged interfaces or between fractured surfaces without a healing agent [109]. A poly(N,N-dimethylacrylamide)-clay nanocompsite hydrogel (D-NC hydrogel) is used to demonstrate the self-healing. The adhesion of two cutting surfaces was achieved by the long polymer chains from either cutting side interacting with clay surfaces through physical bonding [109]. This NC hydrogel showed an advantage of its self-healing property that the separated parts could be completely healed by pressing the fractured surfaces together only at a mild temperature (Fig. 2.4). The

self-healed D-NC hydrogel with medium clay content can completely recover (100%) its tensile strength at an optimal condition.

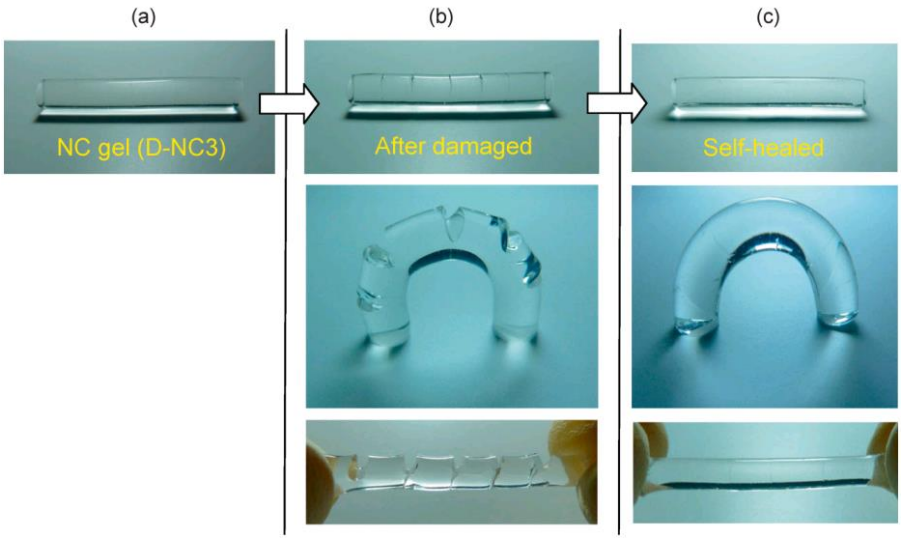

Figure 2.4 Self-healing illustration of the NC hydrogel (D-NC3 indicates poly(*N*,*N*-Dimethylacrylamide)-clay hydrogel), (a) before damage, (b) after damage (with several sharp cuts), (c) after self-healed. Reproduced with permission from [109], copyright (2011) John Wiley and Sons.

2.3.2 Hydrophobic association hydrogels

Jiang and co-workers [110] successfully developed a hydrophobic association hydrogel (HA gel) by micellar copolymerisation of AM and octyl phenol polyethoxy ether acrylate (OP-4-AC) in the presence of sodium dodecyl sulfate (SDS). The hydrogel was formed with the associated micelles acting as physical crosslinking points (Fig. 2.5), which was mechanically strong, excellent in transparency and capable of self-healing and remoulding. Their group further studied the HA gels in the later reports [111-114]. The maximum tensile strength of 212.79 kPa, elastic modulus of 4.98 kPa and elongation at break of 1281.41% were achieved [111]. Especially, the reversible dissociation of the associated micelles renders the self-

healing ability of HA gels. The cut hydrogel specimen can self-heal after putting the two cut parts together at a wet environment and ambient temperature [112]. Temperature-responsive poly(AA-AM) gels with exceptional mechanical strength were also reported by the same group [113]. The monomers AA and AM accounted for the majority in the polymer copolymerisation during the preparation, while a small portion of octylphenol polyoxyethylene ether acrylate with seven ethoxyl units (OP-7-AC) was used to create hydrophobic segments. The transparency of the HA gels was greatly affected by the phase transition. Thus, the transparency could be controlled by regulating the phase transition temperature through varying the ratio of AA to AM, monomer concentration, and fraction of hydrophobic monomer OP-7-AC and surfactant SDS in the synthesis.

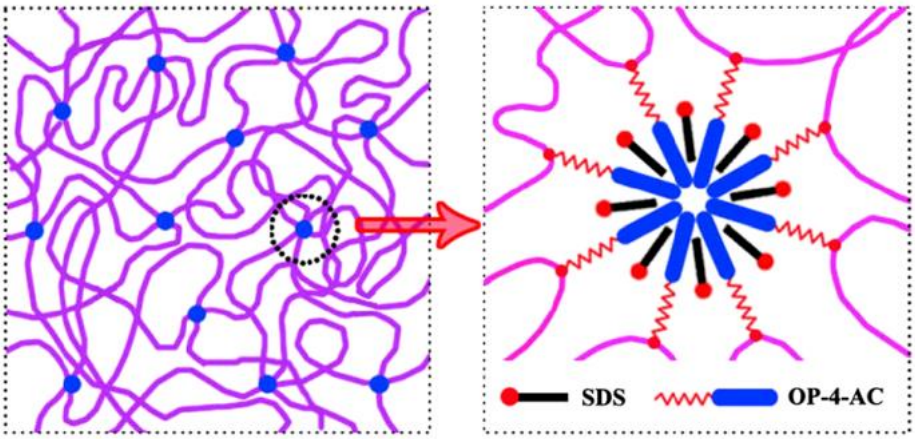

Figure 2.5 Schematic representation of the structural model of HA gels formed by hydrophobic association. Reproduced with permission from [111], copyright (2010) Elsevier Ltd..

Several other HA gels studies were also reported by different groups [115-118]. Tough and self-healing PAM HA gels [115] were prepared by copolymerising stearyl methacrylate (C18) or dococyl acrylate (C22) with AM monomer in a sodium

dodecyl sulfate (SDS) solution. These hydrogels exhibited a shear storage modulus of around 1 kPa (at 1 Hz), and elongation at break of 3600% for C18 gel and 1300–1700% for C22 gel, respectively [115]. The fractured C18 hydrogels can self-heal by pressing together at room temperature, and exhibit the similar extensibility as the original hydrogels, indicating a complete repair. The exceptional self-healing capability owes to the free, non-associated C18 blocks in the hydrogels. The structural studies [116,117] on the PAM HA gels reveal that the self-healing capability are determined by the length of alkyl side chains and the concentration of the surfactant. 18-carbon methacrylates on the side chain are optimal for self-healing efficiency. On the other hand, the decrease in the surfactant SDS concentration leads to weakening of self-healing ability, however, benefits a significant improvement in the mechanical strength.

2.3.3 Other physically crosslinked hydrogels

Apart from aforementioned strong physically crosslinked hydrogels, there are some other successful approaches towards synthesising mechanically reinforced physical hydrogels. PVA has been used in the biomedical applications and its hydrogel materials have become significantly interesting since exceptionally strong PVA hydrogels [119,120] were produced by a number of freezing-thawing cycles, without utilisation of a chemical crosslinking or a reinforcing agent. The process of densification of the macromolecular structure saw a strong physical hydrogel. Peppas and Stauffer's findings [119,121] suggested that the properties of PVA hydrogels, such as the strength, stability and swelling ratio, depended on the solution concentration, the polymer molecular weight, freezing time, processing temperature and the repeating times of freezing-thawing process. The strongest gel was achieved

when a 15 wt.% PVA solution was subject to five freezing-thawing cycles: freezing at −20 ℃ for 24 h and subsequently thawing at 23 ℃ for 24 h. The dependence of mechanical performance on water content were compared in two sets of hydrogels [122]: the hydrogels with 75 wt.% water content exhibited a compressive strength of 2.1 MPa at the strain range of 60–62%, and compressive modulus of 1–18 MPa (comparable to that of natural articular cartilage) and those with a higher water content of 80 wt.% exhibited a compression strength of 1.4 MPa at the strain range of 45–47% and compressive modulus of 0.7–6.8 MPa. Three concepts of hydrogen bonding, polymer crystallisation and phase separation were commonly accepted to interpret the gelation mechanism of the PVA hydrogels [121]. However, the phase separation was suggested to contribute more to their excellent mechanical properties than the polymer crystallisation [123,124]. Adopting the above concept, more studies on PVA based hydrogels synthesised by freezing-thawing method were reported for biomedical applications, such as PVA hydrogel nanoparticles for drug delivery [125], cellular PVA hydrogels with enhanced swelling and mechanical performance [126]. Furthermore, several nanofiller reinforced mechanically strong PVA nanocomposite hydrogels were reported, such as carbon nanotube-PVA nanocomposite hydrogels with an increase in tensile strength by 94% and tensile modulus by 78% compared with the neat PVA hydrogel [127], clay-PVA nanocomposite hydrogels with a tensile modulus increased by 27% [128], and GO-PVA nanocomposite hydrogels with a tensile strength increase by 132% and a compressive strength by 36% [129].

Wang et al. [32] produced dendritic macromolecule nanocomposite hydrogels. The hydrogels were formed by crosslinking clay nanosheets (CNSs) pre-treated with sodium polyacrylate (ASAP). The crosslinking agent was dendritic macromolecules (G3-binder). Clay sheets can be bonded by the adhesive dendron-terminated ends of

crosslinking agent through electrostatic attraction [32], as shown in Fig. 2.6. This hydrogel had a high storage modulus of 0.5 MPa, good biocompatibility, and rapid and complete self-healing. A few freshly cut hydrogel blocks could self-heal by simply pressing them together. The fresh surfaces of the hydrogel were essential for their adhesion.

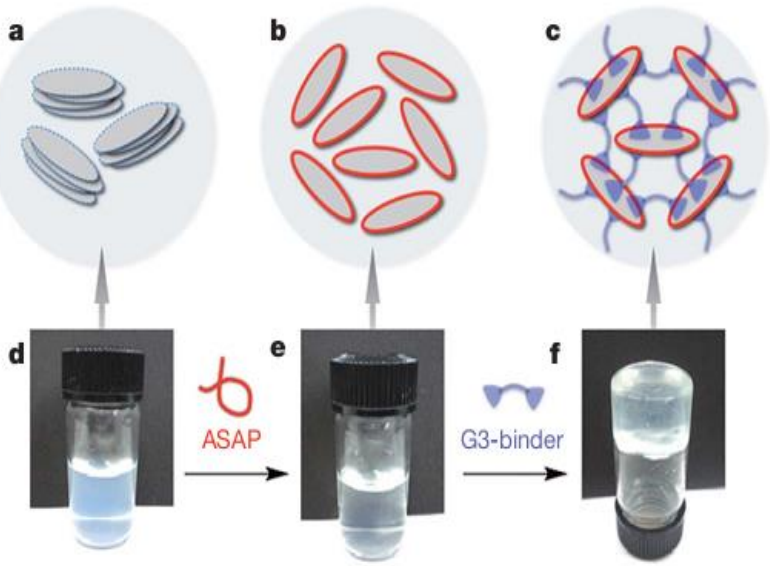

Figure 2.6 Schematic of the gelation mechanism of the hydrogel, (a) stacked CNSs, (b) homogeneously dispersed CNSs by interaction with ASAP, (c) the formed hydrogel network by CNSs crosslinking dendritic macromolecules. d-f, Optical images corresponding to the different status of a-c. Reproduced with permission from [32], copyright (2010) Nature Publishing Group.

Besides the different tough hydrogels, ionically crosslinked polyelectrolytes hydrogels were also an important strategy to achieve tough, resilient and self-healable hydrogels. Henderson et al. [130] reported ionically crosslinked hydrogels, exhibiting a high fracture stress (up to ~1 MPa). The hydrogels were formed by crosslinking hydrophobic poly(methyl methacrylate) (PMMA) and hydrophilic

poly(methacrylic acid) (PMAA) triblock copolymers with divalent ions (Zn^{2+}, Ca^{2+}, Ni^{2+}, Co^{2+}, and Cu^{2+}) in pH-buffered solutions. The hydrogels ionically crosslinked by Zn^{2+} show maximum ultimate strength of 0.86 MPa at 170% strain, Young's modulus up to 21 MPa, and the strain energy density of 1.4 MJ m^{-3} [130]. The optimal mechanical performances were achieved on the appropriate conditions, which were relevant to the type and concentration of cations, and pH value of the matrix. Some PMAA midblocks are associated with adjacent PMAA midblocks by divalent ions, whereas, the PMMA backbones are crosslinked by physical association. The ionical links, relatively stronger than physical association, can first break to dissipate energy upon deformation, and the commitment is reversible. The ionically crosslinking and physical association in the system synergistically contributes to the remarkable increase in their mechanical properties.

There were other reported polymer hydrogels that could be classified as ionically crosslinked hydrogels, precisely speaking, physically and chemically crosslinked hydrogels. For example, alginate/N,O-carboxymethyl chitosan (NOCC) hydrogels crosslinked mainly by ionic bonds were reported with potentials for oral drug delivery, where microencapsulated hydrogel beads were prepared by adding aqueous blend of alginate and NOCC into a Ca^{2+} solution [131]. PAA-alginate-silica hydrogels with interpenetrating networks structure were prepared by UV polymerisation [132]. The hydrogels consisted of alginate network ionically crosslinked by calcium ions and chemically crosslinked PAA network; that were interpenetrated to each other. The mechanical properties were further improved due to addition of nano-silica into these hydrogels. Sun et al. [133] reported PAM-alginate hydrogels comprising of ionically and covalently crosslinked networks, exhibiting exceptional mechanical properties. They were excellent models of the

double network systems, comprising of a primary ‘alginate’ network ionically crosslinked by calcium ions and a secondary covalently crosslinked PAM network. The hydrogels were greatly enhanced, showing a fracture energy of ~9 kJ m^{-2}, a fracture strength of 156 kPa and a fracture strain of 2300%, at a water content of 90% [133].

Sun et al. [134] reported physical polyampholytes (PA) hydrogels prepared by the random copolymerisation of anionic and cationic monomers, showing high toughness and viscoelasticity. Among various combinations, one typical combination of such an ionic monomer pair is 3-(methacryloylamino)propyl-trimethylammonium chloride (MPTC) and sodium p-styrenesulphonate (NaSS). The randomly distributed charges during synthesis render strong and weak ionic bonds throughout the hydrogel by inter and intra-chain fashion. When the hydrogels are under deformation, the weak ionic bonds preferentially break; meanwhile, the strong ionic bonds preserve the structure of the network. The energy dissipation by the rupture and reform of the reversible weak bonds results in reinforcement of fracture strength, fatigue resistance, toughness and self-healing capability, as illustrated in Fig. 2.7. The PA hydrogels exhibit extraordinary mechanical properties, *i.e.*, ultimate strength of 1.8 MPa at a strain of 750%, a high fracture energy of 4 kJ m^{-2}, and 100% self-heal [134].

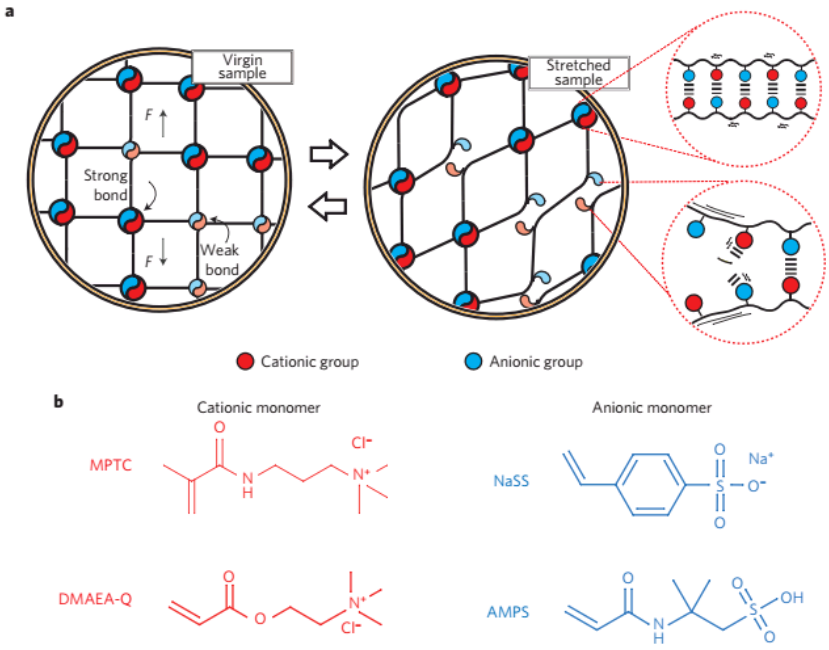

Figure 2.7 Schematic model of a physical polyampholyte hydrogel, (a) a network with strong and weak ionic bonds at original and stretched status. The strong ionic bonds render undamaged backbone of the network upon stretching, whereas, the weak ionic bonds sacrifice to break. (b) The chemical structures of optional cationic monomers of MPTC and DMAEA-Q, and anionic monomers of NaSS and AMPS. Reproduced with permission from [134], copyright (2013) Nature Publishing Group.

2.4 Graphene-polymer nanocomposite hydrogels

2.4.1 Graphene and graphene oxide

Graphene is a flat monolayer of carbon atoms with honeycomb lattice structure [135]. The length of carbon-carbon bond in graphene is 0.142 nm [136]. It has been one of the most exciting materials to be studied since its free-standing form was first discovered by Novoselov and Geim [137] in 2004. Graphene is considered as the parental form of all graphitic materials, *e.g.*, fullerenes, carbon nanotubes and graphite (Fig. 2.8), though it is distinctly different from them [135]. Graphene has a strength at break of 42 N m^{-1}, a Young's modulus of 1.0 TPa [39] and a specific

surface area of 2630 m^2 g^{-1} [138]. It also possesses an electron mobility of 10,000 cm^2 V^{-1} s^{-1} [137] and a thermal conductivity value of ~4.8–5.3 kW m^{-1} K^{-1} [139] at room temperature. There are several techniques reported to prepare graphene. The first attempt was the exfoliation method, also known as scotch tape method by Novoselov and Geim [137]. Chemical vapour deposition method [140] which produces graphene on metallic substrates, and liquid-phase exfoliation method [141] which disperses and exfoliates pristine graphite in organic solvents were also developed. However, a practical and scalable approach to produce graphene is chemical reduction of graphene oxide [142,143]. This product is known as reduced graphene oxide (RGO) or chemically converted graphene [144], which inherits most interesting properties of graphene.

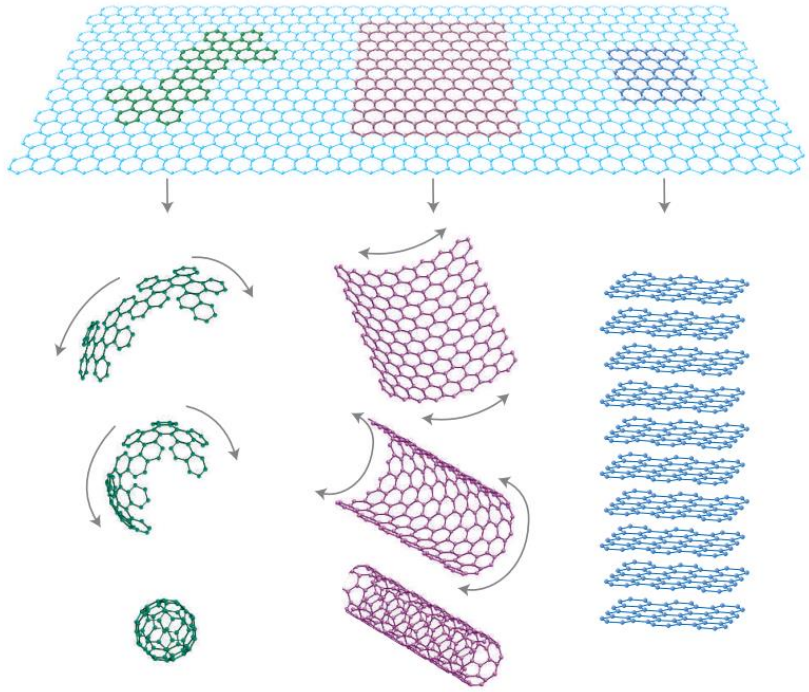

Figure 2.8 Schematic of all forms of the graphitic materials. Graphene, a 2D primary building material, can be transformed into 0D buckyballs, 1D nanotubes, and 3D graphite. Reproduced with permission from [135], copyright (2007) Nature Publishing Group.

Because of its exceptional properties, including high electron mobility, mechanical properties and surface area, graphene has recently attracted tremendous attention in various applications, such as optoelectronics, energy storage, catalysis, gas sensing, super-capacitors, thermoelectric devices, composites, tissue engineering and drug delivery [37,145-148].

GO is a derivative oxidised from graphite, possessing abundant hydroxyl, epoxy and carboxyl groups. Its precise chemical structure has been a debatable subject due to the complexity of the material and the lack of satisfied characterisation techniques [142]. Fig. 2.9 shows the most commonly accepted schematic structure of GO, the Lerf-Klinowski model, in which the hydroxyl, epoxy groups are grafted on the planar surface, whereas carboxyl groups appear at the edge of GO sheets [149]. GO can be prepared by chemical exfoliation using three primary methods. In Brodie's method [150], graphite is oxidised in the reaction involving potassium chlorate and fuming nitric acid. Staudenmaier's method [151] is an improved approach of Brodie's preparation, also adding concentrated sulfuric acid, which can achieve a similar extent of oxidation by one-step synthesis in contrast to Brodie's multiple oxidations. The latest primary one is Hummers' method [152], in which GO is obtained through the vigorous reaction between graphite, concentrated sulphuric acid and potassium permanganate. Several modified approaches [153-155] were developed to improve the primary methods. GO has a similar one-atom thickness of ~0.6–1.2 nm slightly higher than the thickness of 0.345 nm for a monolayer of graphene. GO has a Young's modulus of 207.6 GPa (for a monolayer thickness of 0.7 nm) [40]. In contrast to graphene of excellent electrical conductivity, the GO monolayers are almost insulator, with differential conductivity values of $1–5 \times 10^{-3}$ S cm^{-1} at a bias voltage of 10 V (for a monolayer of GO with a thickness of 1 nm).

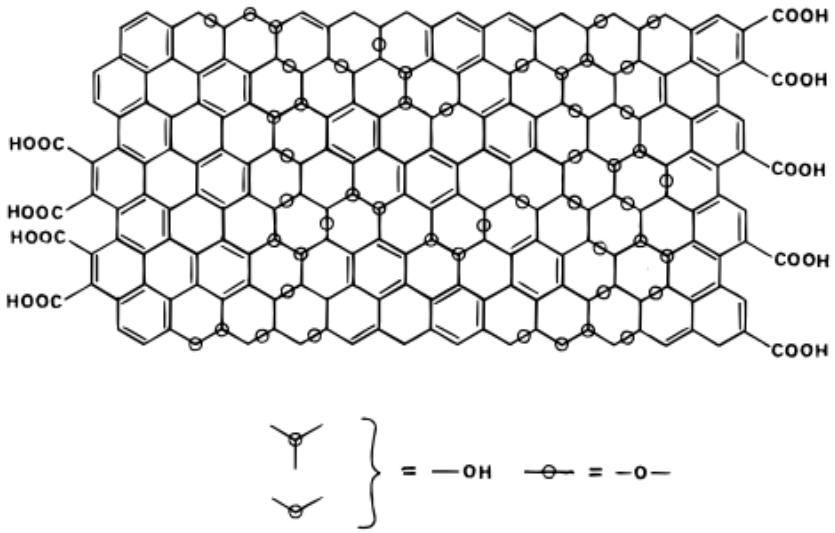

Figure 2.9 Schematic of the structural model of GO. Reproduced with permission from [149], copyright (1998) American Chemical Society.

GO has exceptional properties such as high mechanical strength, superb solution processability and high surface activity. The oxygen-containing groups of GO are available for covalent and non-covalent functionalisation [156] which afford opportunities for various and flexible designs in new material development. The hydroxyl and carboxyl groups of GO are hydrophilic and make it excellent in water dispersion [157]. In addition, GO is cost competitive compared to carbon nanotubes, owing to the low-cost raw material of graphite. In recent years, graphene-based materials have been extensively explored for biomedical applications, such as drug delivery, biosensing and tissue engineering [37,158].

To be used in biomedical applications, the toxicity of graphene and GO is concerned. In the literature, the cytotoxicity of graphene and GO is reported to be influenced by their concentration, size, shape, type of dispersants despite of some mixed findings [158,159]. A recent *in vitro* study [160] showed that GO was no noncytotoxic by promoting mammalian cell growth and also bacterial growth.

Furthermore, surface-functionalisation of graphene or GO with a biopolymer improves biocompatibility and reduces cytotoxicity because it can reduce the strong hydrophobic interactions of graphene or GO with cells and tissues [161]. For instance, chitosan-functionalised GO nanosheets promoted the growth of human mesenchymal stem cells [162]. Gelatin-functionalised GO nanosheets (a size range of 80–3000 nm) showed no toxicity at 200 μg mL^{-1} to human breast adenocarcinoma cells [163]. The PEG coated nanographene sheets were confirmed as an excellent photothermal therapy agent without showing appreciable toxicity to the tested mice [164]. *In vivo* toxicity test to mice did not show obvious toxicity for PEGylated nanographene sheets when the mice were injected with the dose of 20 mg kg^{-1} for 40 days [164]. *In vivo* toxicology with mice demonstrated that PEG-functionalised GO nanosheets had insignificant toxicity and could be excreted from the body by metabolism after intravenous and intraperitoneal administration, with little retention in reticuloendothelial systems [165,166]. Thus, modification and functionalisation of graphene and its derivatives can promote them to be used in potential biomedical applications, though the long-term toxicity of these materials needs further deep studies.

2.4.2 Graphene (or RGO) based hydrogels

Graphene (or RGO) hydrogels have been investigated for applications in energy storage, electronics, electrochemistry and healthcare [167-170]. A self-assembled RGO hydrogel was first reported by Xu and co-workers [168] in 2010, showing high specific capacitances. In this work, GO sheets were reduced to RGO sheets through a hydrothermal process and self-assembled to a hydrogel *via* π–π stacking. The partially reduced GO sheets with remaining hydrophilic oxygenated groups can

encapsulate water in the process of self-assembly. Fig. 2.10 illustrates the formation mechanism of the hydrogel. Since then, a number of graphene-inorganic composite hydrogels, such as graphene-$Ni(OH)_2$ composite hydrogels [169] and graphene-VO_2 nanobelt composite hydrogels [170], were developed, which exhibited further improved capacitances.

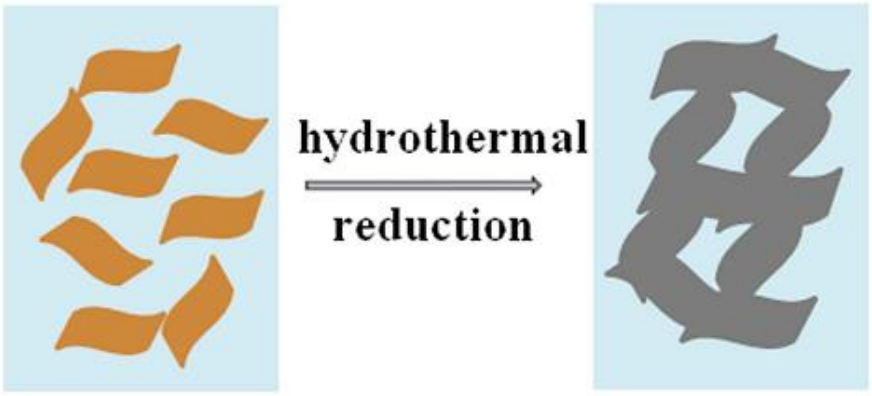

Figure 2.10 Formation mechanism proposed for the hydrothermal reduced GO hydrogel. Reproduced with permission from [168], copyright (2010) American Chemical Society.

Graphene-polymer nanocomposite hydrogels have also been investigated. Graphene-PAM hydrogels were synthesised *via in situ* polymerisation of acrylamide in an aqueous suspension of PAM-stabilised graphene, showing a compressive strength of 9 kPa and a storage modulus of 7 kPa at a water content of about 90 wt.% [171]. At a similar water content, RGO-poly(N,N-dimethylacryl-amide) (PDMAA) hydrogels were synthesised as potential tissue scaffolds by *in situ* polymerisation of DMAA within a pre-formed graphene hydrogel, giving a high compressive strength of 2.62 MPa due to their dual network structures [172]. A graphene-poly(3,4-ethylenedioxythiophene) (PEDOT) hydrogel exhibited a compressive strength of 29.6 MPa and a storage modulus of 2.1 MPa at a water content of 59.5 wt.% mainly

because of the high solid content and the strong physical interaction between PEDOT chain and graphene [173]. These nanocomposite hydrogels were synthesised by *in situ* polymerisation in which the monomer was polymerised in the presence of graphene nanosheets. Self-assembly method was also employed to synthesise RGO-polymer nanocomposite hydrogels. For example, RGO-containing dipeptide hydrogels were synthesised and showed a storage modulus of 41 kPa at a water content of 99.5 wt.% [174]. A RGO-agarose hydrogel was fabricated for miniature-scale water purification [175].

2.4.3 Graphene oxide based hydrogels

A number of GO reinforced polymer hydrogels have recently been reported [176-179]. For example, GO-PVA hydrogel [179] was formed by involving both chemical and physical bonding. In some other hydrogels, monomers were *in situ* polymerised and chemically crosslinked in the presence of GO sheets and water, where GO acted as a reinforcing filler. The hydrophilic oxygen-containing groups allowed GO to readily exfoliate and stably disperse as monolayer sheets in water, conferring good dispersion of GO in the aqueous solution of hydrophilic polymer matrix, which was critical to mechanically strong hydrogels [178]. For example, the compressive strength of a polyacrylamide hydrogel increased by 6-fold with the addition of only 1 wt.% GO sheets [176].

Physically crosslinked GO-based hydrogels could be synthesised by mixing cations, small organic molecules, macromolecules, or long chain polymers with GO suspension [157]. These hydrogels are normally reversible and also sensitive to the surrounding environment, rendering applications with stimuli-responsiveness [177,180]. The oxygenated functional groups on GO surfaces also enable it to serve

as a physical crosslinker in the formation of a hydrogel [179]. Bai et al. [180] reported a pH-sensitive GO-PVA composite hydrogel by a direct mixing method for drug delivery, which showed a storage modulus of ~200 Pa and was able to release 84% of the loaded VB12 molecules into a neutral solution after 42 h as opposed to 51% into an acidic solution. Xu and co-workers [181] prepared a GO-DNA hydrogel, which exhibited environmental stability, dye-loading capacity and self-healing ability. This hydrogel was prepared by heating the mixture of GO suspension and DNA solution at 90 ℃ for 5 min. Upon the heating, the double stranded DNA (dsDNA) was unwound into single stranded DNA (ssDNA); and then the ssDNA chains adhered the neighbouring GO sheets through multiple physical interactions (Fig. 2.11) [181]. The strong physical interactions between DNA and GO, *i.e.*, π–π stacking, hydrophobic interaction, electrostatic interaction and hydrogen bonding, render the hydrogel high environmental stability. The hydrogel obtained a storage modulus of about 4.6 kPa [181].

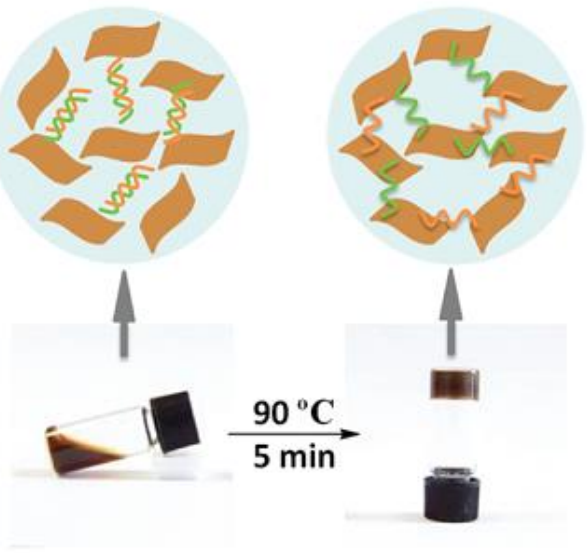

Figure 2.11 Schematic of the preparing procedure and gelation mechanism of the GO-DNA hydrogel. Reproduced with permission from [181], copyright (2010) American Chemical Society.

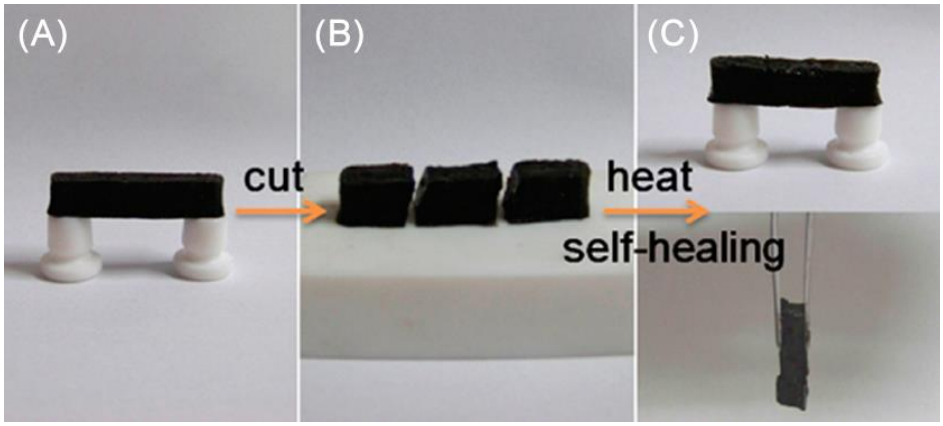

Figure 2.12 Illustration of the self-healing: (A) the initial free-standing hydrogel, (B) three small blocks (cut with a razor), and (C) the self-healed blocks. Reproduced with permission from [181], copyright (2010) American Chemical Society.

The proposed self-healing mechanism of GO-DNA hydrogel was similar to the preparation process, *i.e.*, residual dsDNA contained in the hydrogel could unwind and adhere the cutting surfaces after the hydrogel blocks were pushed together and heated at 90 ℃ for 3 min [181]. The hydrogel blocks could be adhered together and held on between two supports horizontally or hung vertically, shown in Fig. 2.12.

2.5 Gelatin and graphene-gelatin nanocomposites

2.5.1 Introduction to gelatin

Gelatin is a denatured biopolymer, derived from collagen, with abundant amino groups and carboxyl groups on its molecular chains [182]. Gelatin shows inherent cationic nature at pH values below its isoelectric point *via* protonation of amino groups [183]. It possesses distinctive characteristics, such as biocompatibility, remarkable affinity to proteins, biodegradability and low cost. Therefore, gelatin is widely used for food, cosmetic, pharmaceutical and medical applications [184,185]. Gelatin is obtained by extracting collagen-source materials, which constitute the

main organic component of animal skins, bones, tendon, and loose connective tissues [185,186]. The acid or alkaline process is applied to the raw material before gelatin is extracted. Type A and Type B gelatin denote the acid-extracted and alkaline-extracted gelatin, respectively [185].

Gelatin has three predominant groups of amino acids among some 18 amino acids that compose partially ordered linear gelatin chain with very little ramifications [185]. Glycine is the predominant N-terminal amino acid of alkaline-extracted gelatin, while alanine is the primary amino acid of acid-extracted gelatin [187]. Roughly one-third to half of the amino acid residues are glycine or alanine. Proline or hydroxyproline makes up about one-fourth of the total amino acid residues [187]. Gelatin could be enzymatically degraded *in vivo* and split to yield smaller rnolecules which could be excreted or metabolised [188].

2.5.2 Graphene-gelatin nanocomposites and hydrogels

Prior to the development of the hydrogels combined graphene and gelatin, graphene-gelatin composite and gelatin functionalised graphene nanoparticles were explored. Previous research on dry and solid GO-gelatin nanocomposites demonstrated that the presence of no more than 2 wt.% GO improved the mechanical properties and induced the growth of more calcium phosphate biominerals in contrast to pristine gelatin [189]. Furthermore, gelatin functionalised graphene nanosheets were prepared for drug delivery and cellular imaging, in which gelatin chains reduced GO and grafted onto the surface of the resultant RGO nanosheets [163]. In this case, gelatin not only improved biocompatibility of graphene nanosheets, but also acted as a reducing agent to reduce GO to RGO under mild heating (95 ℃) forming covalent bonding with RGO through its amino groups.

GO-PAA-gelatin nanocomposite hydrogels were reported, which presented a tensile strength of 150–250 kPa with ~90 wt.% water [190], and a compressive strength of 7–26 MPa with 29–51 wt.% water content [191], mainly owing to their strong semi-interpenetrating network comprising chemically crosslinked PAA and loose gelatin chains as well as the low water contents. UV crosslinked GO-gelatin methacrylate composite hydrogels were also reported, which showed a compressive strength of 91.3–976.7 kPa at a water content of 94.3–94.5 wt.% [192]. These findings indicate the possibility of creating strong nanocomposite hydrogels primarily based on graphene (or GO) and gelatin.

2.6 Polyamidoamine (PAMAM) dendrimer-based hydrogels and hybrids

2.6.1 Introduction to PAMAM dendrimer

Starburst dendrimers are highly ordered oligomeric and polymeric compounds, *i.e.*, 3D molecular architectures possessing dimensionally precise surfaces with a defined number of surface groups [193-195]. The dendrimers are synthesised by repeating reaction starting from initial cores, such as small organic molecules. Starburst dendrimers can mimic certain properties of micelles and liposomes and even those of biomolecules of biological systems [193]. Dendrimers show great potential in the biomedical applications, including drug delivery, tissue engineering, gene transfection, and therapeutic imaging [195-199]. PAMAM dendrimer is an important dendrimer family, a class of macromolecules which are synthesised through two main routes: divergent synthesis or convergent synthesis, achieving a 3D architecture with a core (ammonia or ethylenediamine (EDA)), repeating units (amidoamine) and active surface groups (amino groups for full-generation and carboxylic acid groups

for half-generation) [200-202]. PAMAM dendrimers are commercially available and have been extensively studied in biomedical field due to their low cytotoxicity, controllable size and easy functionalisation [203]. The potential applications of PAMAM dendrimers include drug carriers, pharmaceutical agents, gene transfection reagents, biosensors, etc. [204-207]. The toxicity of PAMAM dendrimers is generally influenced by the factors of their concentration, exposure duration, generation, and terminal groups [204,208,209]. PAMAM dendrimers possessing cationic termini display higher cytotoxicity than polyationic dendrimers. The peripheral amino groups of PAMAM dendrimers could be modified with other molecules to reduce the positive charge on their surface, such as partial acetylation, acylation or glycation, and cause the dendrimers less cytotoxic. The modified PAMAM dendrimers have been successfully utilised in biomedical applications [206,210].

2.6.2 Graphene-PAMAM dendrimer nanocomposite and hydrogels

Amine-terminated PAMAM dendrimer is an interesting cationic material for the biomedical research. Collagen scaffolds with incorporation of amine-terminated PAMAM dendrimer were reported, where the dendrimer was used as an additional crosslinker to improve the environmental stability of chemically crosslinked collagen scaffolds [211]. A number of PAMAM-PEG hydrogels were investigated for versatile platforms in biomedical applications, in which PAMAM was the primary building component [212,213]. The combination of PAMAM dendrimers and graphene derivatives has been introduced to develop hybrid nanomaterials in different forms. RGO nanosheets modified by PAMAM dendrimers were reported for catalysis [214,215]. RGO-PAMAM-silver nanoparticles were prepared for

electrode applications and biosensing [216]. PAMAM-modified GO nanosheets and GO-PAMAM composites, showing an excellent adsorption ability, were investigated for removing heavy metal ions from waste water [217,218]. GO and hyperbranched dimethylolpropionic acid polyester-toughened PAA hydrogels with excellent water absorbing capability and high mechanical properties were also reported [219]. PAMAM dendrimers have an advantage over linear chain polymers on hydrogel gelation, because they have much more functional end groups available for crosslinking, so the crosslinking density of the resulting hydrogels might be higher, leading to higher mechanical properties [196]. In addition, the dendrimers could be readily modified to modulate the chemical, physical and biological properties where necessary [212].

2.7 Other graphene-cationic polymer nanocomposites and hydrogels

Nanocomposites with the combination of another cationic natural biopolymer, such as chitosan and GO in different physical forms were reported. Small additions of GO enhanced the mechanical properties and drug delivery performance in dry and solid chitosan-GO nanocomposites [220,221]. Chitosan-functionalised graphene nanosheets [222,223] were investigated for potential application as pH-sensitive drug carriers. GO-chitosan nanocomposite hydrogels were reported as broad range adsorbent materials for purifying water [224]. Self-assembled chitosan hydrogel using GO nanosheets as crosslinkers was reported [225]. Graphene-chitosan conductive hydrogels were prepared which are processable, exhibit tunable swelling properties and show excellent biocompatibility [226].

2.8 Summary

Hydrogels have advanced remarkably in the past decades. However, in order for hydrogels to be successfully used for biomedical applications, there are still two major challenges to tackle, including: 1) sufficiently improving the mechanical properties. For instance, native articular cartilage can bear a compressive strength of 3–18 MPa [227], whereas most synthetic hydrogels are much lower than expected; 2) possessing self-healing ability like many biological tissues. So far the reported materials capable of self-healing require so strict conditions to heal, *e.g.*, heating at high temperature and/or fresh cut surfaces [32].

The physically crosslinked NC hydrogels and dendritic macromolecular hydrogels showed good self-healing ability and relatively higher mechanical properties in comparison with other self-healing hydrogels. Both hydrogels are crosslinked mainly by ionic interactions which are stronger than the other non-covalent interactions such as hydrogen bonding and hydrophobic effect. Thus, the strategies of using ionic interactions as crosslinking bonds to build strong and self-healing networks seem promising. That could be utilised to develop novel nanocomposite hydrogels using a cationic polymer such as gelatin or a dendritic polymer and strong graphene nanosheets to obtain desired strength, toughness and self-healing properties. Furthermore, a few other issues need be aware of, which are favourable to achieve mechanically strong hydrogels such as increasing crosslinking density and yield homogeneous nano/micro structure [91].

Chapter 3. Self-assembled graphene oxide–gelatin nanocomposite hydrogels

3.1 Introduction

The aim of this chapter is to develop a new type of polymer nanocomposite hydrogels crosslinked by physical interactions (*i.e.*, electrostatic interaction and hydrogen bonding) with high mechanical performance for potential uses in biomedical applications. Herein, novel physically crosslinked GO-gelatin nanocomposite hydrogels were prepared by a simple self-assembling approach without involving an organic crosslinker or a complex synthesis procedure. GO-gelatin nanocomposite hydrogels with various material ratios were prepared, and characterised by X-ray diffraction (XRD), Fourier transform infrared spectroscopy (FT-IR), Raman spectroscopy and scanning electron microscopy (SEM). GO was also characterised and tested by atomic force microscopy (AFM) and thermogravimetric analysis (TGA). The chemical structure, morphology, static and dynamic rheological properties, pH-sensitivity, and gelation mechanisms of the hydrogels were discussed in detail. The GO content effect on their mechanical properties was studied. The effective crosslinking densities were determined by the rheological measurements. Their potential application in pH-responsive drug release was demonstrated, in which drug release tests were carried out on a typical GO-gelatin nnanocomposite hydrogel using model drug fluorescein sodium.

3.2 Experimental section

3.2.1 Materials

Graphite powder (size < 20 μm), gelatin (type B, BioReagent, bloom strength 225, isoelectric point: 4.7–5.2, average molecular weight M_w: 50,000), potassium permanganate ($KMnO_4$), sodium nitrate ($NaNO_3$), hydrogen peroxide (H_2O_2, 30%), concentrated sulphuric acid (H_2SO_4, 98%), hydrochloric acid (HCl, 35%), phosphate buffered saline (PBS) tablets and fluorescein sodium salt (BioReagent) were all purchased from Sigma-Aldrich.

3.2.2 Preparation of graphene oxide

GO was synthesised by a modified Hummers' method [152,155]. Briefly, 69 mL concentrated H_2SO_4 and 1.5 g $NaNO_3$ was mixed with 3.0 g graphite powder at 0 ℃ in an ice bath, and afterwards 9.0 g $KMnO_4$ was gradually added into the graphite mixture and kept its temperature lower than 20 ℃ while stirring. The temperature was then raised to 35 ℃ before the mixture was stirred for 12 h. Next, an additional amount of $KMnO_4$ (9.0 g) was added gradually, and the mixture was kept stirring at 35 ℃ for a further 24 h. The resulting brown paste-like mixture was cooled down to room temperature and poured onto 400 mL ice with 20 mL H_2O_2. Through a rigorous reaction, the mixture immediately turned from brown to bright yellow. After stirring for 2 h, the resultant graphite oxide was filtered through cellulose membrane (pore size: 0.45 μm, Whatman) and washed with 1:10 HCl aqueous solution (400 mL) and filtered again. The filtrate was washed with distilled water and centrifuged (Centrifuge 5804, Eppendorf, Germany) at 4000 rpm for 30 min repeatedly until the supernatant became neutral. The solid graphite oxide was

dispersed in distilled water (~1 mg mL^{-1}) and exfoliated under sonication (Elmasonic S 30 H, Elma, Germany) for 1 h. The fully exfoliated GO suspension was dialysed to remove the remaining acid and metal species for at least one week. Finally, the GO suspension was freeze-dried (FreeZone Triad Freeze Dry System, Labcoco Corporation) to obtain GO powder for future use.

3.2.3 Preparation of GO-gelatin nanocomposite hydrogels

GO-gelatin nanocomposite hydrogels (GGHs) were prepared by self-assembly. A typical synthesis of hydrogels is described below. The GO aqueous suspension (10.9 mg mL^{-1}) was prepared by mixing pre-determined amounts of GO and water by 1 hour's stirring and 30 minutes' sonication. Gelatin solutions with varying concentrations were prepared by stirring desired amounts of gelatin and water for 1 h at 60 ℃. Hydrogel samples were created by directly mixing 5.5 mL of the GO suspension with 0.5 mL of a gelatin solution at 37 ℃. During this process, the gelatin solution was added drop-wise into the GO suspension while the mixture was stirred, and hydrogels formed in about 20 s. The hydrogels are designated as G*m*G*n*H, where *m* and *n* define the concentration of GO and gelatin, respectively, in the final hydrogel with the unit of mg mL^{-1}. For example, G10G5H is a hydrogel comprising 10 mg mL^{-1} GO and 5 mg mL^{-1} gelatin.

3.2.4 Structural characterisation

AFM was performed by using a Veeco Instruments Dimension 3100 atomic force microscope operated in tapping mode. A diluted GO aqueous suspension was dropped onto a freshly cleaved mica surface and left overnight to dry in air. SEM was carried out using an FEI Inspect F scanning electron microscope

at 10 kV. An aqueous GO suspension (10 mg mL^{-1}) and GO-gelatin hydrogels were first frozen in liquid nitrogen, and then subjected to freeze-drying under vacuum at −10 ℃ for two days. The lyophilised GO and GO-gelatin hydrogels were fractured carefully and fixed on aluminium stubs. All samples were coated using a gold sputter coater (Emscope SC500A) and the fracture surfaces were observed under SEM. FT-IR of gelatin, graphite, lyophilised GO and lyophilised GO-gelatin hydrogels was carried out on a Perkin Elmer Spectrum 100 spectrometer with a diamond attenuated total reflectance (diamond-ATR) unit at a resolution of 4.0 cm^{-1} and an accumulation of 5 scans. Raman spectroscopy was conducted on a Renishaw inVia Raman Microscope with 514 nm laser excitation operating at 1.0 mW. XRD was achieved with an X-ray diffractometer (STOE STADI P) with Cu $K\alpha_1$ radiations (λ = 0.15406 nm) at 40 kV and 35 mA. Diffraction patterns were recorded at a scan speed of 0.27^{o} s^{-1} and with a step size of 0.03^{o} (2θ). TGA was performed under nitrogen atmosphere with a Perkin Elmer Pyris 1 Thermal Analyser at a heating rate of 5 ℃ min^{-1}.

3.2.5 Rheological measurements

Rheological measurements were performed on an AR2000 Advanced Rheometer (TA Instruments). Oscillatory shear measurements were carried out at 25 ℃ to determine the storage moduli (G') and loss moduli (G'') of the GO-gelatin hydrogels over an angular frequency range from 0.1 to 100 rad s^{-1} under a fixed strain of 0.1% (in the linear viscoelastic region pre-determined by dynamic strain sweep tests). All measurements were performed with a parallel-plate geometry (diameter 40 mm) equipped with a solvent trap to

avoid evaporation. The gap between two parallel plates was fixed to be 1.0 mm.

A series of shear viscosity measurements were also carried out on the rheometer to study the formation mechanisms of the hydrogels. Samples, including the precursor solutions of the hydrogels and the mixtures of these solutions at various ratios, were measured over a shear rate range from 0.01 to 1 s^{-1} at 25 ℃.

3.2.6 *In vitro* drug release tests

The drug-encapsulated nanocomposite hydrogel was prepared as follows. First, a model drug, fluorescein sodium, was mixed into a gelatin solution under stirring for 1 h, which was subsequently introduced into a GO suspension to form a drug-loaded hydrogel comprising of 10.0 mg mL^{-1} GO, 10.0 mg mL^{-1} gelatin and 3.0 mg mL^{-1} fluorescein sodium. For each test, 0.4 mL drug-loaded hydrogel was deposited into a small plastic tube before it was immersed into 100 mL of a neutral PBS solution (pH = 7.4) or an acidic HCl solution (pH = 1.7). The release test was kept undisturbed at body temperature (37 ℃) throughout the whole period. The tests were repeated three times. The concentrations of fluorescein sodium in the PBS solution and HCl solution were determined by UV–Vis absorbance intensities from two calibration curves of fluorescein sodium in PBS at the wavelengths of 490 nm and in HCl solution at 437 nm, respectively. UV-Vis Spectroscopy was performed on a UV/VIS/NIR Spectrometer (Lambda 900, Perkin Elmer), with a scan interval of 1 nm.

3.3 Results and discussion

3.3.1 Structure and properties of GO-graphene nanocomposite hydrogels

Fig. 3.1 illustrates the XRD patterns of graphite, graphite oxide and lyophilised GO-gelatin hydrogels. A strong diffraction peak of graphite oxide appears at 2θ = 10.6 °, corresponding to an interlayer spacing of 0.83 nm, which is consistent with the previous report [181]. As a comparison, the pristine graphite has a diffraction peak at 26.4 °, corresponding to an interlayer spacing of 0.34 nm. The results indicate that graphite oxide has been successfully synthesised and the oxygenated functional groups are present on the surface of graphene sheets expanding the interlayer spacing of graphite [228].

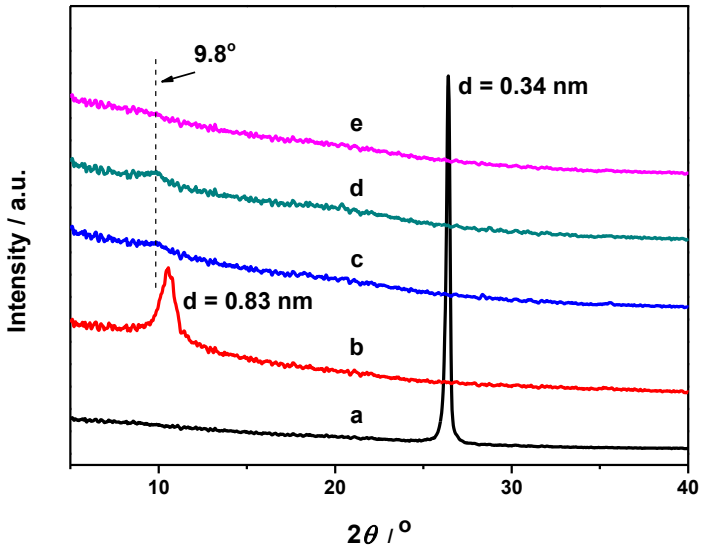

Figure 3.1 XRD patterns of (a) graphite, (b) graphite oxide and lyophilised GO-gelatin nanocomposites: (c) G10G5H, (d) G10G7.5H and (e) G10G10H, respectively.

XRD results are supported by the observation of single GO nanosheets under AFM. The thickness of GO nanosheets is about 1.0 nm and the typical lateral dimension is one to several micrometres (Fig. 3.2). This thickness is similar to those

reported by others [155,229], and much greater than the thickness of single-layer graphene (0.35 ± 0.01 nm) measured by AFM [230]. The thickness of single-layer GO determined under AFM is also greater than the interlayer spacing of graphite oxide determined by XRD, which may be due to the presence of a water layer between GO and the substrate and/or the resolution of the AFM tip [231].

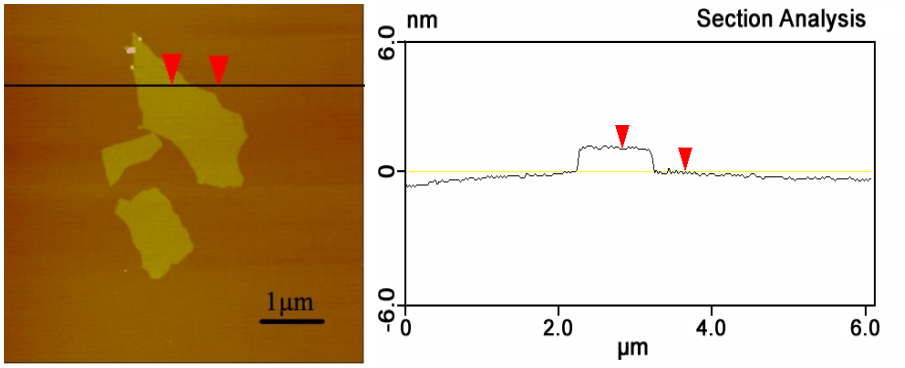

Figure 3.2 Tapping mode AFM topographic image and height profile of a single layer of GO which shows the vertical distance is about 1.0 nm.

The oxidisation degree of the GO was estimated by TGA (Fig. 3.3). The TGA curve of graphite is almost flat, exhibiting little mass loss from room temperature to 800 ℃. In contrast, there is 61% mass loss for GO during the same temperature range. The first mass loss of 14% is found below 100 ℃, which is attributed to the loss of water molecules absorbed into the GO bulk material. The major mass loss occurs at around 210 ℃, corresponding to the main peak observed in the derivative weight curve, due to pyrolysis of the labile oxygen-containing functional groups, yielding CO, CO_2, and steam [149]. The subsequent mass loss at above 250 ℃ is owing to elimination of remaining functional groups. Therefore, one can estimate the oxygen-containing functional groups of the dried GO to be approximately 55% after the elimination of water from GO.

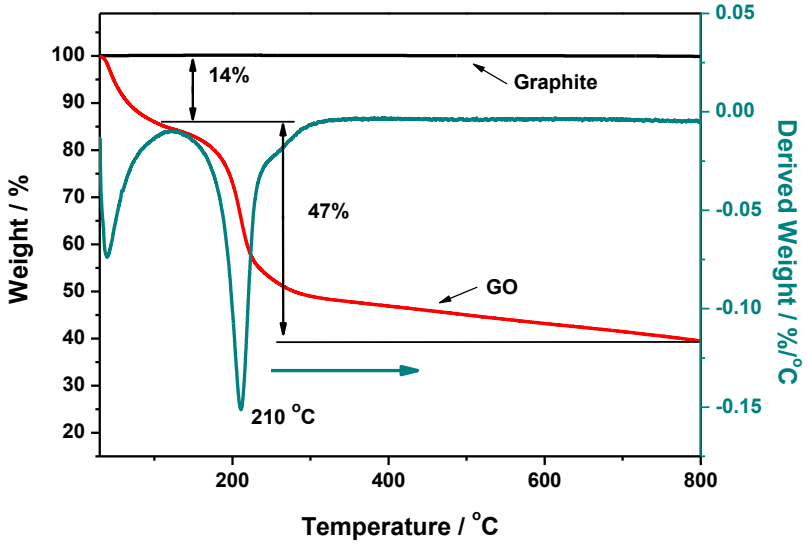

Figure 3.3 TGA curves of graphite and GO.

Compared to the evident XRD peaks in graphite oxide and graphite, small broad peaks centred at 9.8° are observed in curves c and d (Fig. 3.1) of the lyophilised hydrogels G10G5H and G10G7.5H, which indicates good dispersion of GO in the hydrogels with only a low degree of re-aggregation of some GO single sheets during the hydrogel formation. However, there is no observable peak in the curve e of G10G10H comprising the highest content of gelatin and the lowest content of GO, suggesting that exfoliated GO remain as individual sheets in the polymer matrix [232] even though the amount of GO in lyophilised G10G10H nanocomposite is as high as 50 wt.%.

Fig. 3.4 shows FT-IR spectra of graphite, gelatin, lyophilised GO and GO-gelatin hydrogels with different gelatin contents and a fixed GO content. The spectrum of the pristine graphite only shows a weak absorbance centred at 3400 cm^{-1}, which could be O–H stretching bond from absorbed water. The spectrum of GO reveals the presence of C=O carbonyl stretching at 1731 cm^{-1}, C=C aromatic carbon vibration at 1619 cm^{-1}, C–OH stretching vibration at 1360 cm^{-1}, C–O–C epoxy at

1276 cm^{-1} and C–O alkoxy at 1050 cm^{-1} [233,234], O–H stretching vibration and the intercalated water molecules at 3100–3400 cm^{-1} [235]. The peaks in the gelatin spectrum can be assigned to the C=O stretching vibration of amide I (1631 cm^{-1}), the N–H bending of amide II (1519 cm^{-1}), amide III (1232 cm^{-1}), and N–H stretching of primary amine (3264 cm^{-1}), respectively [236,237]. After incorporation of gelatin into the GO, the C=O vibration peak of GO at 1731 cm^{-1} becomes weaker and disappears completely in G10G10H (curve e) with the highest gelatin content (50 wt.%), which can be interpreted by the formation of ammonium carboxylate complex through the protonated amino groups of gelatin and carboxyl groups of GO [238,239], arising from the electrostatic forces between the two materials.

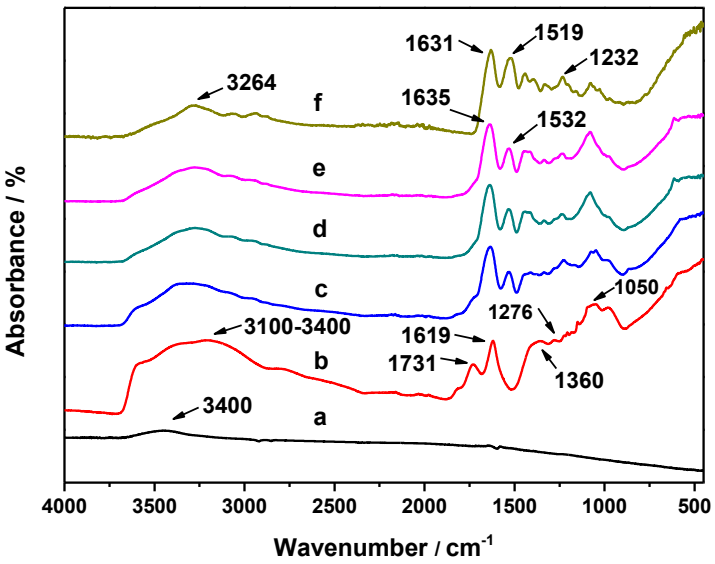

Figure 3.4 FT-IR spectra of (a) graphite, (b) GO, (c-e) lyophilised GO-gelatin hydrogels: (c) G10G5H, (d) G10G7.5H and (e) G10G10H, and (f) gelatin powder.

In the FT-IR spectra of the nanocomposites (curves c-e), the in-plane bending peak (amide II in gelatin) occurs and is blue-shifted from 1519 cm^{-1} to 1532 cm^{-1}. Meanwhile, the N–H stretching vibration (3264 cm^{-1}) of gelatin becomes broader and its intensity increases with increasing gelatin amount. Both of these are ascribed

to the formation of hydrogen bonds between $–NH_2$ of gelatin and oxygen-containing groups on the GO sheets. The amide I vibration is also blue-shifted from 1631 to 1635 cm^{-1}, again indicating the hydrogen bonding between gelatin and GO. These are clear evidence that strong physical bonding exists between the two components in the GO-gelatin hydrogels.

Fig. 3.5 shows Raman spectra of graphite, lyophilised GO and lyophilised GO-gelatin nanocomposite hydrogels with various contents of gelatin. Curve a is a typical Raman spectrum of raw graphite, showing a sharp G band at 1579 cm^{-1} in relation to the in-phase vibration (E_{2g} mode) of the graphite lattice, and a weak D band at 1358 cm^{-1} corresponding to the symmetric A_{1g} mode of lattice [240]. A broad peak at 2723 cm^{-1} is assigned to 2D band [241]. After the oxidation, the G band and D band of graphite become broader in GO. A significantly increased intensity ratio of GO, I_D/I_G (0.81), is also observed compared to that (0.06) of graphite, due to a higher level of disorder of the graphene layers and the increased defects [242,243]. Moreover, the G band of GO is blue-shifted to 1599 cm^{-1}, which is mainly due to the presence of higher energy functional groups with isolated double bonds on GO sheets [244] and the newly appeared D' band (at 1620 cm^{-1}) [240,245]. The Raman spectra of the lyophilised GO-gelatin hydrogels show similar profiles to that of GO except that G band of GO sheets is gradually red-shifted from 1599 to 1590 cm^{-1} in the hydrogel with the highest content of gelatin. This shift is owing to the charge transfer from the amino groups of the branched chains of gelatin to GO sheets [181]. Both FT-IR and Raman spectra of lyophilised hydrogels confirm the existence of hydrogen bonding and electrostatic forces, or in other words physical crosslinking between gelatin and GO.

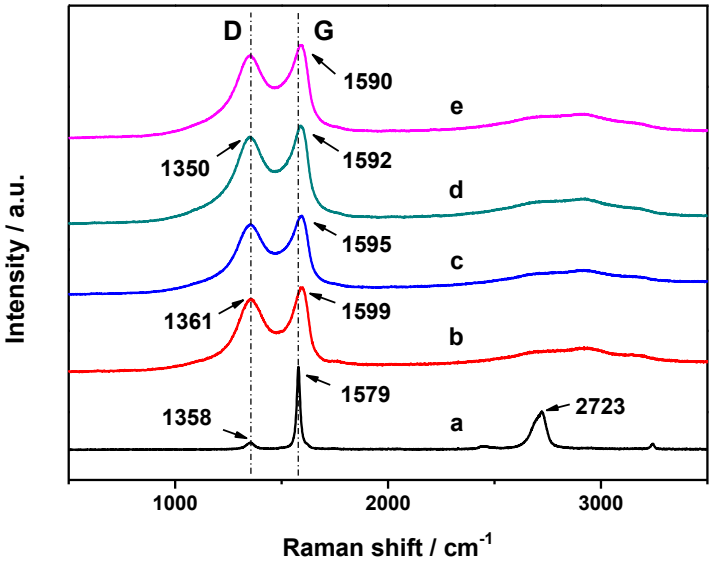

Figure 3.5 Raman spectra of (a) graphite, (b) GO, (c-e) lyophilised GO-gelatin nanocomposites (c) G10G5H, (d) G10G7.5H and (e) G10G10H.

The interior morphology of the lyophilised GO aqueous suspension (10 mg mL^{-1}) and GO-gelatin hydrogels is investigated by SEM. SEM images (Fig. 3.6) show that the lyophilised GO suspension and GO-gelatin hydrogels exhibit open and interconnected porous structures. The interconnected structure of GO (7.2 ± 3.1 μm) is formed due to the structural changes during the drying stage in which the GO sheets become contacted to each other (Fig. 3.6A); the hydrogen bonding between GO sheets and the residual hydrogen-bonded water molecules between GO sheets [246] may have facilitated the formation of this interconnected network. When GO is mixed with gelatin to form a nanocomposite hydrogel, the porous structure turns less uniform and the surface of the pore walls and edges becomes rougher. In the nanocomposite samples (Figs. 3.6B-D), the walls of the porous structure consist of GO sheets (shown by the orange arrows) with coated gelatin, similar to the morphology of the reported GO-hemoglobin hydrogel [247]. Gelatin is also

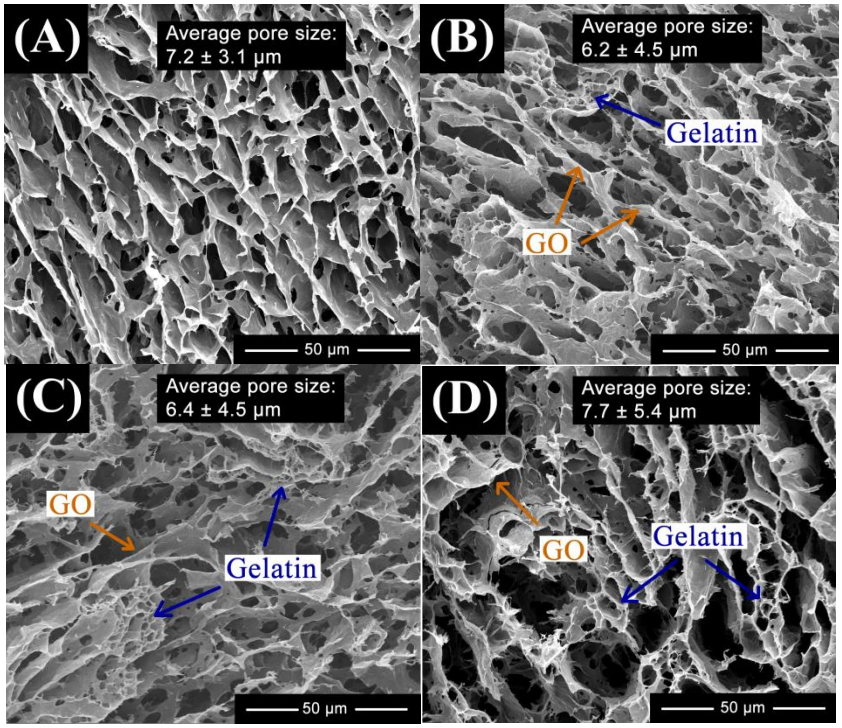

Figure 3.6 SEM images of (a) a lyophilised GO aqueous suspension (10 mg mL^{-1}) (no hydrogel is formed at this concentration), and lyophilised (b) G10G5H, (c) G10G7.5H and (d) G10G10H hydrogels. Orange arrows indicate the gelatin-coated GO sheets and blue arrows show gelatin linking GO sheets together.

found to link GO sheets in the nanocomposite hydrogels (shown by the blue arrows). With increasing gelatin content, more gelatin links can be observed in the G10G7.5H and G10G10H (Figs. 3.6C and D). The average pore sizes for G10G5H, G10G7.5H and G10G10H are 6.2 ± 4.5 µm, 6.4 ± 4.5 µm and 7.7 ± 5.4 µm, respectively. The inhomogeneity of the structure increases with increasing gelatin content (Figs. 3.6B-D) due to a more rapid gelling process and a less thorough mixing of the two components during the preparation of the hydrogel. The $-NH_2$ groups of the gelatin chains become protonated by –COOH groups from GO, leading to strong electrostatic attractions between the two materials and the formation of a robust hydrogel. In addition, hydrogen bonding between the amino groups of gelatin and oxygen-containing

functional groups on GO surfaces contributes to the forces to form the hydrogels.

The nanocomposite hydrogels are pH-sensitive, which can be confirmed by a tube inversion method [248] that shows a gel-sol transition (Fig. 3.7). When the pH value of the GO-gelatin hydrogel is increased from ~4.6 to beyond 9.0 by an ammonia solution, the hydrogel turns to a sol. Subsequently, as an HCl solution is added into the sol to decrease the pH value to below 9.0, the sol converts back to a gel. The sol-gel transition is reversible and repeatable. It is believed that pH value can modulate protonation and de-protonation of the amino groups of gelatin [249] and hence the electrostatic forces between gelatin and GO nanosheets. When the pH value of the hydrogel increases, the amino groups of gelatin gradually deprotonate, which results in the weakening of electrostatic forces between the two opposite charged components [249], that is, positively charged amino groups of gelatin and negatively charged carboxyl groups of GO nanosheets. Such a process releases the carboxyl groups on GO sheets from the coordination with the amino groups of gelatin, which could increase electrostatic repulsion between GO nanosheets. When the repulsive forces overcome the binding force, the gel-sol transition happens [180]. Conversely, decreasing the pH value of the sol causes further protonation of amino groups of gelatin, and thus ammonium carboxylate complex restores between the amino groups of gelatin and carboxyl groups on GO nanosheets. When the binding forces dominate, the sol-gel transition takes place [180].

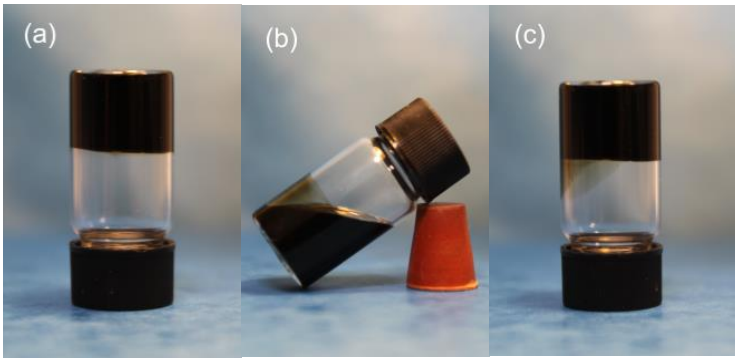

Figure 3.7 Photos of (a) GO-gelatin hydrogel (G10G5H) (pH: ~4.6), which (b) turns to sol when pH > 9.0, and (c) gels again when pH < 9.0. Inner diameter of the bottle: 15 mm.

Small deformation oscillatory measurements (Fig. 3.8) reveal that the nanocomposite hydrogels have a substantial elastic response, and that shear storage modulus (*G′*) is generally frequency independent within the test range (0.1–100 rad s^{-1}). Furthermore, *G′* is significantly higher than loss modulus (*G″*). This result indicates that the GGH has a stable and continuous network with a high degree of crosslinking [181]. Although the GGH contains 98–98.5 wt.% water, its mechanical property is still impressive, with maximum storage modulus up to 114.5 kPa. This is probably due to the cooperative contributions of inherently superior stiffness of GO and strong interactions between gelatin chains and GO sheets.

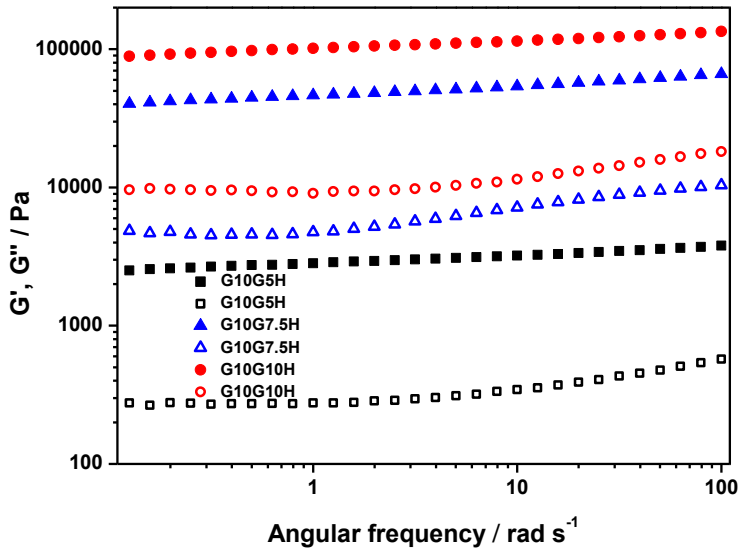

Figure 3.8 Storage moduli *G'* (solid) and loss moduli *G''* (hollow) of hydrogels: (A) G10G5H, G10G7.5 and G10G10H.

The rheological properties of the resulting hydrogels depend on the concentrations of both GO and gelatin. As shown in Fig. 3.8, the storage modulus of the nanocomposite hydrogel increases with increasing gelatin concentration when the concentration of GO is fixed at 10 mg mL^{-1}. The values are 3.2, 54.0 and 114.5 kPa for G10G5H, G10G7.5H and G10G10H, respectively. G10G7.5H has a 50% increase in gelatin content compared to G10G5H, resulting in a ~16-fold increase in storage modulus. More significantly, G10G10H double the gelatin content of G10G5H, resulting in a ~35-fold increase in storage modulus.

The increase of the gelatin content introduces more effective polymer chains between the neighbouring GO nanosheets, enhancing the robustness of the 3D network significantly. It is worth noting that hydrogels could not be formed by either GO or gelatin alone at the same or even doubled concentrations. As previously discussed, GO-gelatin hydrogel network is achieved through physical interactions, that is, electrostatic forces between protonated amino groups of gelatin and carboxyl groups on GO sheets [250], as well as hydrogen bonding between the amino groups

of gelatin and oxygen-containing functional groups on GO surfaces. The abundant functional groups on GO nanosheets and gelatin chains induce multiple crosslinking sites on each GO nanosheet and gelatin chain, which account for the high mechanical performance of the GO-gelatin hydrogel. As expected for most physical hydrogels [109,118], these GO-gelatin hydrogels also exhibit self-healing ability. The freshly-cut pieces of hydrogel can self-heal into a whole block after they are gently pressed together for 3 minutes (pictures not shown).

The storage modulus values of 54.0 and 114.5 kPa reported herein for GO-gelatin nanocomposite hydrogels with water contents of 98.25 wt.% and 98 wt.% are significantly higher than the value (~0.7 kPa) obtained for self-assembled GO-chitosan hydrogels with a lower amount of water (91.7 wt.%) reported by Han et al. [225]. They fall within the range of the values (10–400 kPa) for other self-assembled GO-chitosan hydrogels with a higher amount of water (99.4–99.5 wt.%) reported by Chen at el. [224].

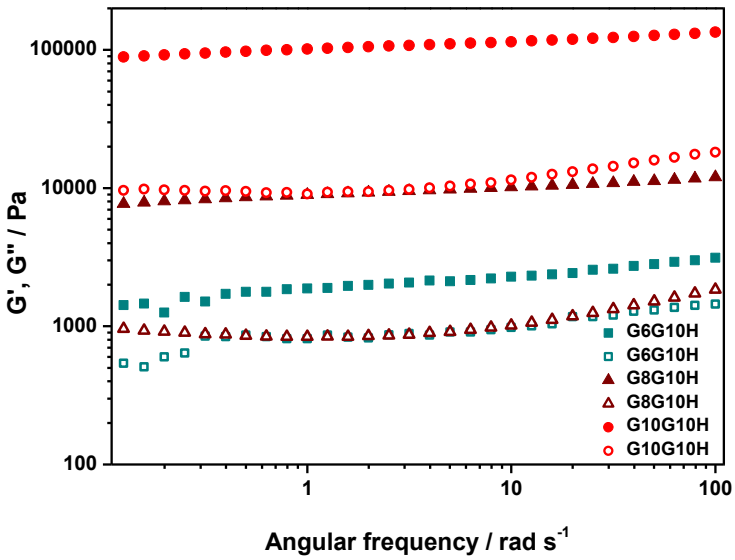

Figure 3.9 Storage moduli *G′* (solid) and loss moduli *G″* (hollow) of hydrogels: G6G10H, G8G10H and G10G10H.

In order to understand the contribution of GO loading to the rheological properties, another set of hydrogels were prepared and tested. Fig. 3.9 shows the shear moduli of GO-gelatin hydrogels with a constant gelatin concentration (10 mg mL^{-1}) and various GO concentrations (6, 8 and 10 mg mL^{-1}, respectively). The storage modulus increases with the increase in the concentration of GO, being 2.3 kPa for G6G10H and 10.2 kPa for G8G10H in contrast to 114.5 kPa for G10G10H. The storage moduli are generally independent of the frequency and much higher than their corresponding loss moduli over the entire test range. These are similar to the results discussed above for the hydrogels with various gelatin contents. By comparing these two sets of data, it is found that the storage modulus of G10G7.5H is much greater than that of G8G10H, and G10G5H is stiffer than G6G10H. All of these hydrogels have a similar water content (98–98.5 wt.%). This indicates that GO will make more contribution to the mechanical performance of the hydrogels than gelatin when at the same concentration, because of its higher intrinsic mechanical properties.

The rheological data are also used to determine the crosslinking density, *N*, and the number average molecular weight of polymer chains between the crosslinkers in the hydrogel, $\overline{M}_c$. *N* is defined as the number of active polymer chains per unit volume in the network. A well-known rubber elasticity theory (equation 3.1) [251] is used to determine the *N* and $\overline{M}_c$ of the hydrogels,

$$G = NkT = \frac{cRT}{\overline{M}_c}\left(1 - \frac{2\overline{M}_c}{M}\right) \quad (3.1)$$

where *G* is the static shear modulus, *T* is absolute temperature (298 K), *k* is Boltzmann constant (1.38065×10^{-23} J K^{-1}), *R* is the gas constant (8.31 m^3 Pa K^{-1}

moL^{-1}), *c* is the polymer concentration, and *M* is the average molecular weight of the polymer. To apply equation 1, the synthesised GO-gelatin hydrogels are assumed as homogeneous Gaussian networks, in which well dispersed GO nanosheets crosslink gelatin chains, and gelatin chains with an average molecular weight of 50,000 are considered to be sufficiently long and have freely rotating links [251].

To obtain *N* and $\overline{M}_c$, static shear modulus *G* needs to be identified. Table 3.1 lists the dynamic shear moduli of GO-gelatin hydrogels determined by oscillation rheological measurements as above discussed. According to the literature [252], static Young's modulus (*E*) of elasticity is highly correlated to dynamic Young's modulus (*E'*), which is represented by an empirical equation 3.2:

$$E = 0.629E' - 1.586 \tag{3.2}$$

For homogeneous isotropic materials, a simple relation exists between static Young's modulus and shear modulus (equation 3.3), which also applies to dynamic moduli [253].

$$G = \frac{E}{2(1+\nu)} \tag{3.3}$$

where *v* is Poisson's ratio. Because the hydrogels are assumed as ideal rubbers, *v* is taken as 0.5 [254]. By combining equations 3.2 and 3.3, the dynamic shear modulus *G'* (i.e., storage modulus) can be converted to the desired static shear modulus *G*, in equation 3.4.

$$G = 0.629G' - \frac{1.586}{2(1+\nu)} \tag{3.4}$$

Thus, N and $\overline{M}_c$ for GO-gelatin hydrogels can be determined by equations 3.1 and 3.4, with the values of dynamic shear modulus. The results are shown in Table 3.1. For the hydrogels with a fixed GO content, N increases from 4.9×10^{23} m^{-3} for G10G5H to 175.0×10^{23} m^{-3} for G10G10H. Correspondingly, $\overline{M}_c$ drops from 4,938 to 339 g moL^{-1}. The lowest crosslinking density (4.9×10^{23} m^{-3}) could be considered as a threshold crosslinking density because 5 mg mL^{-1} is the critical concentration of gelatin to form the hydrogel (see next section). For the hydrogels with a fixed gelatin content, N increases from 3.5×10^{23} m^{-3} for G6G10H to 15.5×10^{23} m^{-3} for G8G10H. Correspondingly, $\overline{M}_c$ drops from 10,213 to 3,358 g moL^{-1}.

Table 3.1 Crosslinking densities and number average molecular weights of polymer chains between the crosslinking sites in the hydrogels with varying composition.

Sample	Gelatin (mg mL^{-1})	Storage modulus (kPa)	Crosslinking density ($\times 10^{23}$ m^{-3})	Number average molecular weight (g moL^{-1})
G10G10H	10	114.5	175.0	339
G10G7.5	7.5	54.0	82.6	535
G10G5H	5	3.2	4.9	4938
G8G10H	10	10.2	15.5	3358
G6G10H	10	2.3	3.5	10213

These results suggest the mechanical properties of the GO-gelatin hydrogels can be adjusted by controlling the crosslinking density and the number average molecular weight between the crosslinking sites in the preparation process through varying the composition and/or the molecular weight of gelatin [255,256]. Furthermore, the crosslinking density and $\overline{M}_c$ affect the degradation rate of the

hydrogel and diffusivity of the encapsulated drug during drug release [256]. By manipulating the crosslinking density and $\overline{M}_c$, these properties may be tuned too.

3.3.2 Gelation mechanisms of GO-gelatin nanocomposite hydrogels

Rheological properties are commonly used to study gelation mechanism of hydrogels [257,258]. A typical hydrogel sample was prepared by adding 0.5 mL of a gelatin solution drop-wise into 5.5 mL of a GO suspension, and hydrogels formed in approximately 20 s. Self-assembly of these hydrogels is very rapid, so it is challenging to monitor and study the ongoing gelation process. Thus, a series of viscosity measurements were performed, in which the concentration of GO in the final mixture was fixed at 10 mg mL^{-1} while the concentration of gelatin increased gradually, from zero to 10 mg mL^{-1}. This series of mixtures represent the suspensions at pre-stages and the fully gelled hydrogels from the first set of three hydrogels discussed above.

Fig. 3.10A shows shear viscosities of the GO suspension, GO-gelatin suspensions (containing 1–4 mg mL^{-1} gelatin) and GO-gelatin hydrogels (containing 5–10 mg mL^{-1} gelatin) as a function of shear rate. The viscosity increases with increasing concentration of gelatin over the entire range of shear rate (0.01–1.0 s^{-1}). The evolution of viscosity (at shear rate = 0.8 s^{-1}) of the suspensions and hydrogels against the change of the concentration of gelatin is shown in Fig. 3.10B. There are minimal viscosity increases at the initial stage (0–2 mg mL^{-1} gelatin, stage Ⅰ in Fig. 3.10C), when only a small amount of gelatin chains are available to interact with the GO nanosheets. At the following stage (2–4 mg mL^{-1} gelatin, stage Ⅱ in Fig. 3.10C), with increasing polymer content, the viscosity exhibits a slightly more rapid increase (Fig. 3.10B, inset). This change may be related to the formation of abundant GO-

gelatin clusters in the suspension [259] because of the physical interactions between gelatin chains and GO sheets. When the concentration of gelatin reaches the critical value of 5 mg mL^{-1}, a steep increase in viscosity is observed. The viscosity of the hydrogel (containing 5 mg mL^{-1} gelatin) is two orders of magnitude greater than that of pure GO suspension. At this point (stage III in Fig. 3.10C), the grown GO-gelatin clusters interact to each other and long gelatin chains may bridge the adjacent GO sheets [260], as seen in the SEM images (Figs. 3.6b-d). In consequence, the gelation threshold is reached and the binding force is high enough to drive the gelation of physically crosslinked GO-gelatin hydrogel. It is noteworthy that these GO-gelatin hydrogels with 3D networks can be formed using a very low total amount of GO and gelatin in water (only 1.5–2 wt.% solid content in the hydrogel). These results confirm that GO and gelatin chains can physically crosslink together effectively, presumably *via* multiple crosslinking sites on each nanosheet and each polymer chain due to their ample functional groups.

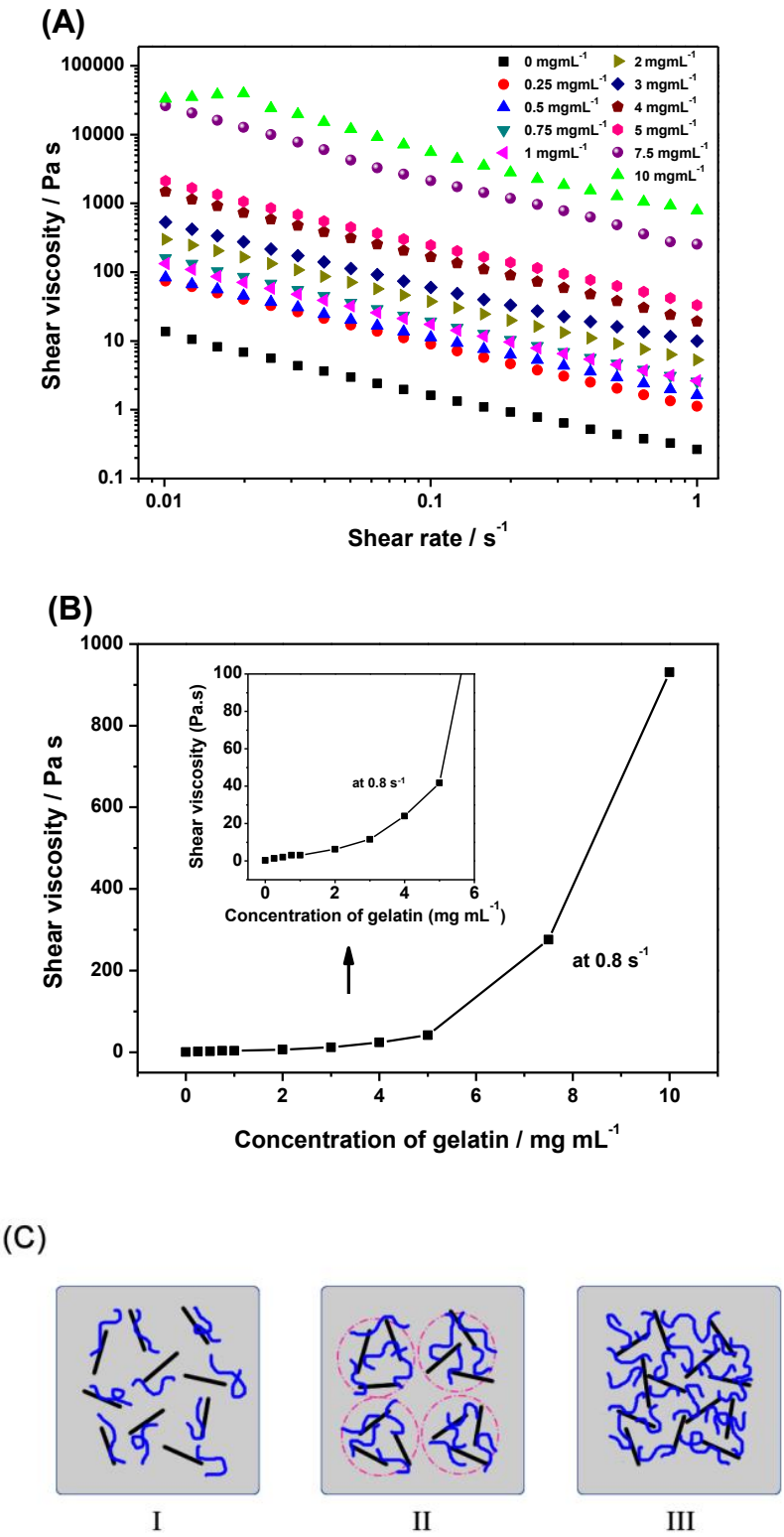

Figure 3.10 (A) Viscosities of the mixtures of an aqueous GO suspension (10 mg mL^{-1}) and a gelatin solution with varying concentration from zero to 4.0 mg mL^{-1}, and of the hydrogels with 5.0, 7.5 and 10 mg mL^{-1} gelatin; the plateau at the initial part of the viscosity curve of G10G10H may be due to

zero shear or yield stress between the imperfect surface of the hydrogel and one of the parallel plates upon application of a force; (B) The correlation between viscosity and the concentration of gelatin at the shear rate of 0.8 s^{-1}, derived from the results in Fig. 3.10A. (C) Proposed gelation mechanism of GO-gelatin hydrogels in different stages of gelation; black lines and blue curves indicate GO nanosheets and polymer chains, respectively. Stage I: low gelatin concentration, stage II: medium gelatin concentration forming clusters, and stage III: relatively high gelatin concentration forming a hydrogel.

3.3.3 pH-sensitive drug release behaviour of GO-gelatin nanocomposite hydrogels

Fig. 3.11 shows the drug release profiles of the GO-gelatin hydrogels in two different pH media. The releasing profile in PBS (pH = 7.4) shows a rapid drug release within the first 10 h, and then it turns to a plateau. The drug release in the acidic solution (pH = 1.7) has a similar trend, but the release begins to slow down just after 3 h. There is a significant difference between the equilibrium drug release amounts in neutral and acidic solutions. 96% of fluorescein sodium (cumulative drug release: 2.88 mg mL^{-1}) is diffused from the gel into the neutral solution after 45 h, which is more than triple of 28% (cumulative drug release: 0.84 mg mL^{-1}) of the drug released in the acidic medium in the same period of time.

The result indicates GO-gelatin hydrogel is a pH-sensitive drug carrier. Similar pH-sensitive drug release behaviour was previously reported for GO-poly(vinyl alcohol) hydrogels [180], chitosan-functionalised GO nanosheets [222,223], dry chitosan-GO nanocomposites [221] and dry chitosan-reduced GO nanocomposites [261]. The diffusion of the encapsulated drug in an acidic solution is unfavourable because GO sheets tend to form tightly packed aggregates [180].

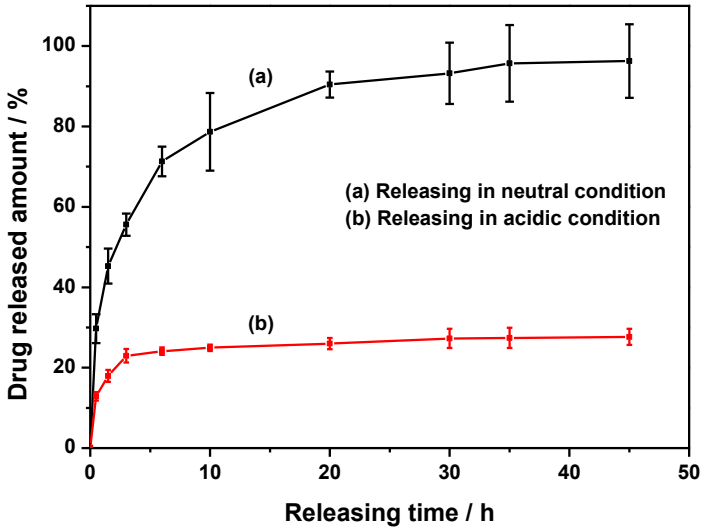

Figure 3.11 Drug releasing profiles in neutral PBS (pH = 7.4) and acidic HCl solutions (pH = 1.7). Error bar indicate standard deviation on three replicate samples.

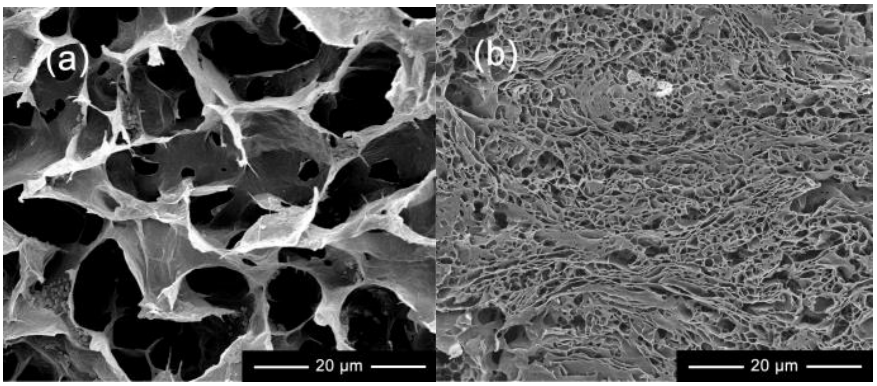

Figure 3.12 SEM images of the cross section of the lyophilised hydrogels after immersion in (a) neutral PBS (pH = 7.4) and (b) acidic HCl (pH = 1.7) solutions for 45 h.

This hypothesis is verified by the microstructure of the lyophilised hydrogels observed under SEM (Fig. 3.12). The hydrogels had been immersed in both media for 45 h during the drug release experiments. The pore size of the hydrogel from the neutral PBS immersion is significantly higher than that of the hydrogel immersed in the acidic solution. A bigger pore size in the network greatly promotes the diffusion of the encapsulated drug molecules from the hydrogel to a liquid environment [262].

This pH-sensitive drug release behaviour may allow the hydrogels to be used to selectively release a drug in the intestine (pH = 6.6–7.5), with little released in the stomach (pH = 1.0–2.5) [263], thus offering higher drug bioavailability for the treatment of diseases.

The GO-gelatin nanocomposite hydrogels described here are promising candidates for controlled drug delivery, having advantages over conventional pH-sensitive drug delivery systems (*e.g.*, enteric coated tablets, capsules) in terms of the efficacy and controlled release of the drug [264]. While the conventional systems can successfully carry drugs to a specific region of the gastrointestinal tract, they cannot protect the drug in the enzymatic environment due to their burst release of the drug, causing some of the drug to become inactivated or altered [264,265], as well as a fast and uncontrolled release of the drug. Thus, the concentration of the drug in plasma and the efficacy of the drug are difficult to maintain [266]. In contrast, the GO-gelatin hydrogels can protect the encapsulated drug from enzymatic attack much better as they will not break down immediately in an enzymatic environment. Hence, the drug efficacy can be maintained, and the drug can be released in a more steady and controllable manner with a longer release time (as shown in Fig. 3.11), avoiding multiple administrations of the drug within a short period of time. Furthermore, the drug release kinetics of these hydrogels could be optimised by manipulating the crosslinking density and pore sizes of the hydrogels [264].

Gelatin undergoes enzymatically hydrolytic degradation in the body. *In vivo* experiments with mice showed chemically crosslinked gelatin hydrogels with 98.8 wt.% water degraded completely in 10 days [267]. In this work, the drug is first bonded to gelatin, followed by mixing with GO sheets to form a drug-loaded nanocomposite hydrogel, which also leads to the coating of gelatin onto GO sheets

as previously discussed. After the hydrogel is administrated, the gelatin-coated GO nanosheets are expected to gradually dissociate from the bulk hydrogel during the course of gelatin degradation. If an oral administration is applied, gelatin-coated GO nanosheets can be excreted quickly from the body with 2–3% left in a day and almost complete excretion after a week [166].

3.4 Conclusions

Graphene oxide-gelatin nanocomposite hydrogels with various material contents were successfully prepared by self-assembly from the mixtures of an aqueous GO suspension and a gelatin solution at the desired ratios. The physical crosslinks formed between GO and gelatin *via* electrostatic forces and hydrogen bonding were confirmed by FT-IR, Raman spectroscopy, SEM and rheological tests. These hydrogels demonstrated reversible sol-gel transitions upon changing the pH value. While containing 98–98.5 wt.% water, the GO-gelatin hydrogels showed relatively high storage modulus, up to 114.5 kPa. The storage modulus of the hydrogel increased with increasing gelatin or GO concentration, and GO provided a higher modulus than gelatin at a comparable concentration. Studies on the gelation mechanisms revealed that the critical concentration of gelatin to form a hydrogel with 10 mg mL^{-1} GO was 5 mg mL^{-1}. The gelation of the hydrogel underwent three stages: 1) initial increase in viscosity; 2) formation of GO-gelatin clusters; and 3) formation of a hydrogel as the concentration of gelatin reaches the critical value. The multiple crosslinking sites on each GO nanosheet and gelatin chain rendered GO-gelatin hydrogels high mechanical performance. The drug release tests showed high efficiency on the release of a model drug, 96%, to a neutral

solution (pH = 7.4), compared with 28% release to an acidic solution (pH = 1.7). The self-assembly approach to synthesise the GO-gelatin hydrogels was simple and fast, without the need of a toxic organic crosslinker. These relatively strong GO-gelatin nanocomposite hydrogels with pH sensitivity may find potential applications in pH-controlled drug delivery.

Chapter 4. Reduced graphene oxide-gelatin nanocomposite hydrogels

4.1 Introduction

In order to further improve the mechanical properties of the physically crosslinked GO-gelatin nanocomposite hydrogels prepared in Chapter 3, RGO-gelatin nanocomposite hydrogels were prepared by one-pot synthesis *via* a mild heating process (at 95 ℃ for 24 h). It was expected that the amino groups of gelatin could react with functional groups on GO, *i.e.*, ring-opening amination of epoxy and the amidation reaction with carboxylic acid groups at an elevated temperature, and covalently bond to RGO sheets, leading to chemically crosslinked hydrogel networks. Together with the hydrogen bonding between the residual amino groups of gelatin and the residual hydroxyl groups on RGO sheets, the chemically crosslinked hydrogel networks were expected to significantly enhance their mechanical properties compared to the networks purely made up of physical interactions. Moreover, organic crosslinkers were excluded in the preparation, eliminating their toxicity. These are distinguished with the conventional chemical hydrogels. AFM, TGA and UV-Vis spectroscopy were performed to characterise RGO. FT-IR, Raman spectroscopy, XRD and SEM were utilised to characterise the RGO-gelatin nanocomposite hydrogels to study their chemical structure, morphology and gelation mechanisms. The rheological measurements were conducted to decide the rheological properties and the effective crosslinking densities. Water swelling tests of the dried hydrogels were performed and the swelling behaviour was discussed by Fick's diffusion law. The enzymatic degradation tests of the hydrogels were also conducted.

4.2 Experimental section

4.2.1 Materials

Graphite powder, gelatin, and the other chemicals used for GO preparation were the same as used in Chapter 3. Collagenase type II from *Clostridium histolyticum* (≥ 125 CDU mg^{-1} solid) and Dulbecco's phosphate buffered saline (PBS, with $MgCl_2$ and $CaCl_2$, pH = 7.4) were all purchased from Sigma-Aldrich and used as received.

4.2.2 Preparation of RGO-gelatin nanocomposite hydrogels

GO was synthesised from graphite powder using a modified Hummers' method [152,155], purified and freeze-dried as described in Chapter 3. RGO-gelatin nanocomposite hydrogels were prepared by heating mixtures of a GO aqueous suspension and a gelatin solution with desired ratios at 95 ℃ for 24 h. The required amount of GO powder was dispersed in distilled water in a glass vial and stirred for 2 h using a magnetic stirrer before it was subjected to 30 min sonication to obtain a fully exfoliated GO suspension. The gelatin solution was prepared by heating a desired amount of gelatin in distilled water at 60 ℃ for 1 h. In a typical preparation, 0.5 mL gelatin solution (24 mg mL^{-1}) was added into 5.5 mL GO suspension (10.9 mg mL^{-1}) by drop wise while stirring. Then, the mixture, sealed in the glass vial, was heated in an oil bath at 95 ℃ for 24 h. In this study, a series of RGO-gelatin hydrogels at different material ratios were synthesised. The precursor of the RGO-gelatin hydrogels was the mixture of GO dispersion and gelatin solution comprising of 10 mg mL^{-1} GO, and various concentrations of gelatin, *i.e.*, 2, 5 and 10 mg mL^{-1}, respectively. The RGO-gelatin nanocomposite hydrogels were designated as RGG*n*H, where *n* defined the concentration of gelatin in the hydrogels with a unit of mg mL^{-1}.

4.2.3 Structural characterisation

FT-IR, XRD, AFM, TGA, SEM and Raman spectroscopy were carried out on the same instruments using the settings as described in Chapter 3. An aqueous GO suspension (10 mg mL^{-1}), was prepared as described in the preparation section, and RGO-gelatin hydrogels were first frozen in liquid nitrogen, and then dried under vacuum at −10 ℃ for two days and at room temperature for 30 min in a freeze dryer. The lyophilised sponge-like samples for SEM observation were carefully deposited on aluminium stubs before they were coated with gold by a sputter coater. The average pore sizes were calculated by measuring the size of the pores (30 pores) with an ImageJ software.

For AFM characterisation, a diluted RGO aqueous suspension was dropped onto a freshly cleaved mica surface and left overnight to dry in air. UV-Vis spectroscopy was performed on a UV/VIS/NIR Spectrometer (Lambda 900, Perkin Elmer), with a scan interval of 1 nm. The RGO nanosheets used for AFM, UV-Vis spectroscopy and TGA were extracted from the RGO-gelatin hydrogels. A small fraction of hydrogel was smashed and washed three times using distilled water (80 ℃), followed by centrifugation (at 8000 rpm) at each time, to remove excess and non-grafted gelatin on the graphene surface. Some sediment was lyophilised for TGA tests. The remaining was re-dispersed in distilled water at 1 mg mL^{-1} by stirring and then sonicating for 5 min. The obtained suspension was centrifuged at a lower speed (2000 rpm) for 20 min to remove large particles. The supernatant was taken for characterisation under AFM and UV-Vis spectroscopy.

4.2.4 Rheological measurements

Oscillatory shear measurements were carried out to determine the storage moduli (G') and loss moduli (G'') of the RGO-gelatin hydrogels by the same instrument and method used in Chapter 3. The gap between two geometry parallel plates was fixed at 2 mm.

4.2.5 Swelling tests

As-prepared hydrogels were punched into discs with the same size (15 mm in diameter and 6 mm thick). The hydrogels were frozen by liquid nitrogen before freeze-drying. The freeze-dried hydrogel samples were then immersed in excess distilled water to obtain equilibrium swelling at room temperature. The samples were weighed at 0.5, 1, 3, 6, 12 and 24 h. The measurements were carried out on three replicate samples. The swelling ratio (SR) of the hydrogel was calculated according to equation (4.1):

$$SR = \frac{W_s - W_d}{W_d} \tag{4.1}$$

where W_s is the weight of the swollen hydrogel at the different time interval and W_d is the weight of the freeze-dried hydrogel before immersion in water.

4.2.6 *In vitro* Biodegradation

The hydrogel cylinders (RGG10H) with dimensions of 6 mm in height and 15 mm in diameter were placed in 8 mL PBS solution with 0.5 U mL^{-1} collagenase type II and incubated (Shaker Incubator SI500, Stuart) at 37 ℃ and a speed of 100 rpm for 2, 4, 8, 16, 24 and 32 h. At each time point, the collagenase solution was removed and the remaining hydrogels were washed with distilled water. The hydrogels were then lyophilised at −10 ℃ after frozen by using liquid nitrogen. The degradation was

calculated by dividing the lost weight of the lyophilised samples by the original weight of the untreated lyophilised hydrogels. The sample size was three per group. The control samples underwent degradation in the PBS solution without collagenase.

4.3 Results and discussion

The RGO-gelatin hydrogels were synthesised by heating the mixture of an aqueous GO suspension and a gelatin water solution at 95 ℃ for 24 h. According to the literature [163,237], gelatin chains could be grafted onto GO sheets whilst reducing them into RGO. It has been shown that different types of amine can react with some of the functional groups on GO *via* two main routes, *i.e.*, ring-opening amination of epoxy on the surface of GO and the amidation reaction of carboxylic acid groups at the edges of GO, both with the amino groups of gelatin by thermal treatment [238,268,269]. The hydrogen bonding between amine and hydroxyl on the GO was also proposed in the literature [270]. It is, therefore, hypothesised that the main interactions between GO and gelatin during the hydrogel formation process could be the same as discussed above, though the nature of chemical reactions is not totally clear due to the complexity of the GO structure [142]. These proposed main interactions are illustrated in Scheme 4.1 [268]. Through the chemical and physical interactions between GO and gelatin, GO sheets are expected to crosslink with gelatin chains and form a hydrogel whilst being reduced to RGO.

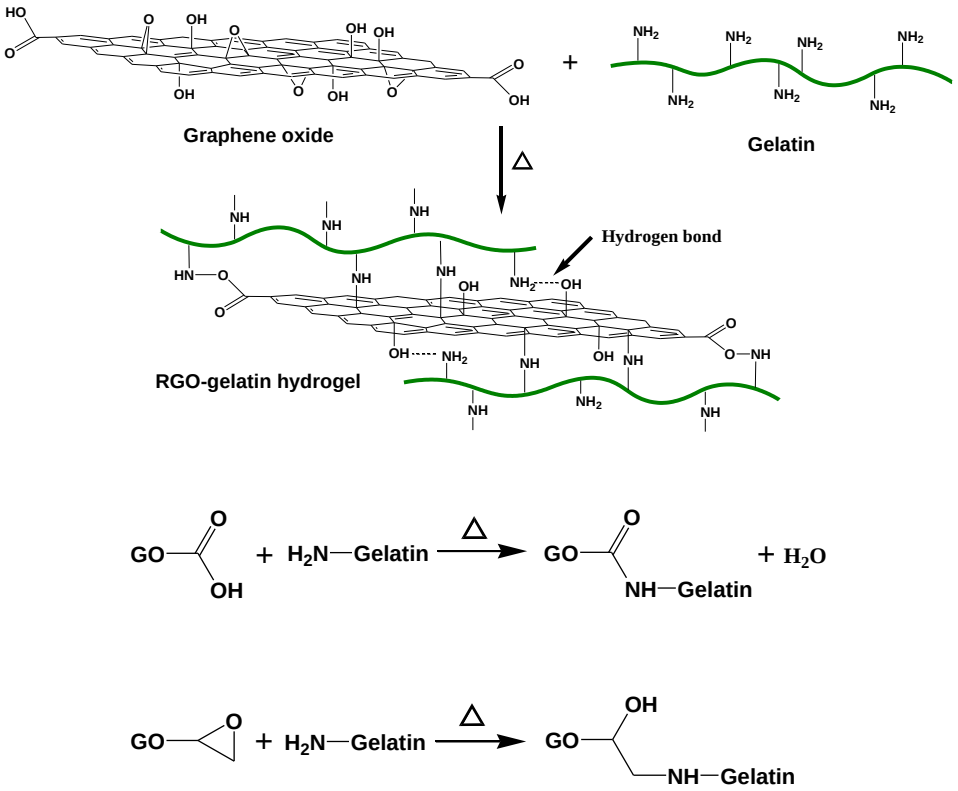

Scheme 4.1 Illustration of the proposed main chemical reactions and physical interactions between GO nanosheets and gelatin to produce a RGO-gelatin hydrogel.

In order to verify the above hypotheses, changes to the chemical structure of gelatin and GO during the synthesis were first investigated by FT-IR spectroscopy. Fig. 4.1 shows FT-IR spectra of graphite, GO, gelatin and lyophilised RGO-gelatin hydrogels with different gelatin contents. The spectrum of the graphite (curve a) only shows a weak absorbance of O–H stretching at 3400 cm^{-1} caused by the absorbed water. The spectrum of GO (curve b) reveals the presence of different types of oxygenated functional group: O–H stretching bond at 3200–3400 cm^{-1}, C=O carbonyl stretching at 1729 cm^{-1}, C–OH stretching vibration at 1361 cm^{-1}, C–O–C epoxy at 1225 cm^{-1} and C–O alkoxy at 1046 cm^{-1}, as well as C=C vibrations from aromatic structure domains at 1621 cm^{-1} [234,271,272]. The spectrum of gelatin (curve f) is recorded as a control, and its characteristic groups are identified: amide I

vibration (C=O, 1627 cm^{-1}), amide II bending vibration (N–H, 1521 cm^{-1}), amide III (1238 cm^{-1}), and N–H stretching (3262 cm^{-1}) [273]. Eliminating the intensity varying due to the various GO weight ratio in the nanocomposites, the epoxy vibration (1225 cm^{-1}) of GO is weakened in RGG5H and RGG10H (curves d and e) confirming the ring-opening reaction between epoxy groups of GO and amino groups of gelatin [268]. Similarly, the C=O stretching vibration of GO gradually decreases in its intensity as the gelatin content increases and almost disappears in RGG10H. This illustrates the amidation of carboxyl groups at the edge of GO with amino groups of gelatin, which agrees well with the previous report [269]. These FT-IR results confirm the proposed chemical reactions illustrated in Scheme 4.1 [268]. The ring-opening reaction between epoxy groups and amino groups is a nucleophilic substitution reaction resulting in the creation of hydroxyl groups and formation of C–N bonds. The amidation of carboxyl groups of GO with amino groups of gelatin is a condensation reaction which requires heat.

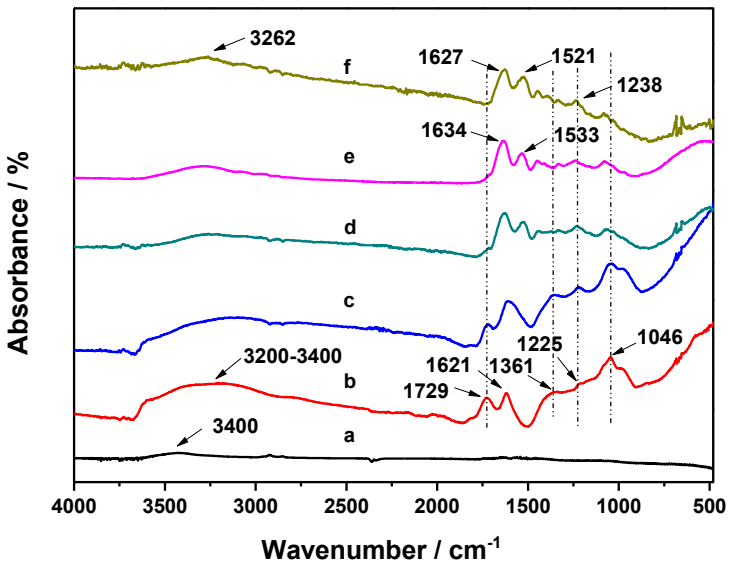

Figure 4.1 FT-IR spectra of (a) graphite, (b) GO, and (c-e) lyophilised RGO-gelatin hydrogels: (c) RGG2H, (d) RGG5H, (e) RGG10H, and (f) gelatin.

It is also found that the modest vibration C–OH centred at 1361 cm^{-1} and the strong C–O vibration at 1046 cm^{-1} in GO become weaker with an increasing amount of gelatin in the hydrogel, indicating partial elimination of the hydroxyl groups of RGO during the synthesis of the hydrogel [163,237]. Furthermore, gelatin has residual $–NH_2$ groups, $–NH_3^+$ and $–COO^–$ ions on its macromolecular chains and these functional groups can form hydrogen bonding and electrostatic attractions with the residual hydroxyl and carboxyl groups of RGO as well as with their adjacent gelatin molecules [238]. Thus, the chemical and physical bonds between the RGO sheets and gelatin chains are the driven forces to link the two components together to form a 3D continuous network, *i.e.* a RGO-gelatin hydrogel, as illustrated in Scheme 4.2.

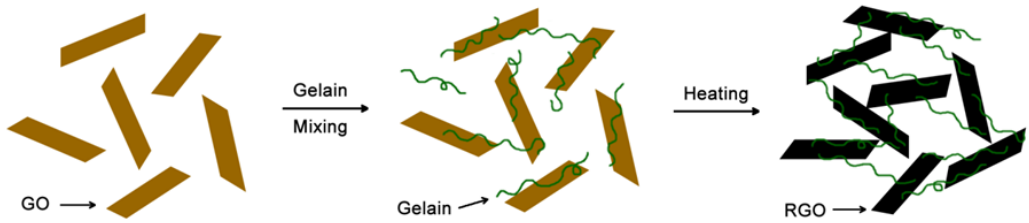

Scheme 4.2 Illustration of the hydrogel formation process.

The structural changes of graphene materials in the hydrogels could also be identified in Raman spectra, as shown in Fig. 4.2. The pristine graphite (curve a) shows a sharp G band at 1579 cm^{-1} in relation to the in-phase vibration of the graphite lattice, and a weak D band is found at 1355 cm^{-1}, which is induced by structural disorder and defects [240,274]. After oxidation, the D band becomes stronger and broader in GO (curve b). As a result, the intensity ratio of D band to G band, I_D/I_G (0.79), increases significantly compared to that of graphite (0.08), which

is associated with a marked decrease in the graphite crystal size arising from a considerably higher level of disorder of the graphene structure and increased defects [243,275]. The G band becomes slightly asymmetric in GO due to its overlap with the defect-related *G'* band at 1620 cm^{-1} [243]. As depicted in Fig. 4.2, the lyophilised RGO-gelatin hydrogels (curves c-e) have similar profiles to that of GO. With the increase of gelatin content in the RGO hydrogels, the intensity ratio of I_D/I_G increases slightly from 0.79 to 0.85. This variation is lower compared to the values found for the reduction of GO by other chemicals reported in the literature [276,277], which may be due to the partial reduction of GO as described subsequently and hence only a small change to the graphite crystal size.

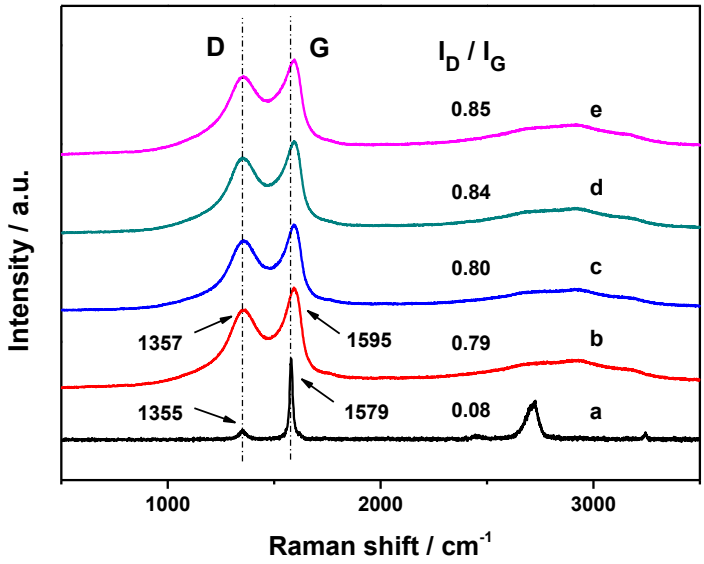

Figure 4.2 Raman spectra of (a) graphite, (b) GO, and (c-e) lyophilised RGO-gelatin hydrogels: (c) RGG2H, (d) RGG5H, and (e) RGG10H. The ratios of I_D/I_G for the hydrogels are also shown in the figure.

XRD patterns of graphite, graphite oxide, gelatin and the lyophilised RGO-gelatin hydrogels are shown in Fig. 4.3. Graphite (curve a) shows a sharp and strong peak at 26.4 °, corresponding to a typical interlayer spacing (*d*) of 0.34 nm [278].

Gelatin powder typically exhibits two broad peaks centred at 20.4 ° and 7.2 °, due to the crystalline structure originated from a-helix and triple-helical structure [279]. A slightly broader 2θ peak for GO (curve b) appears at 10.6 °, corresponding to an interlayer spacing of 0.83 nm. A weak broad peak centred at 8.1° (d = 1.09 nm) is observed for the freeze-dried RGG2H with the least gelatin content (16.7 wt.%). The presence of this weak peak suggests there are a small amount of stacks of not fully dispersed RGO sheets in the hydrogel presumably due to the insufficient gelatin content. In contrast, there is no observable diffraction peak for the lyophilised RGG10H which comprises the highest gelatin content (50.0 wt.%) (curve d), indicating that graphite and gelatin have completely lost their order in the crystal structure and RGO nanosheets are dispersed in the hydrogel as exfoliated single nanosheets [105].

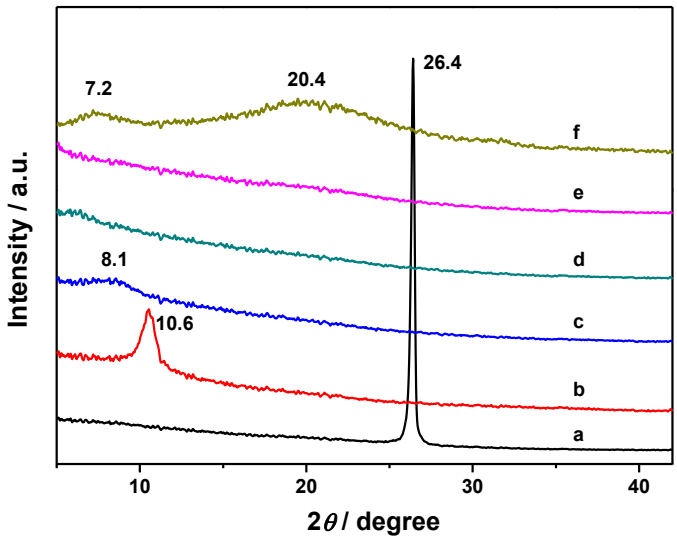

Figure 4.3 XRD patterns of (a) graphite, (b) GO, and (c-e) lyophilised RGO-gelatin hydrogels: (c) RGG2H, (d) RGG5H, (e) RGG10H, and (f) gelatin.

The morphology of GO and RGO nanosheets is illustrated in Fig. 4.4. AFM results show that the thickness of a single layer of GO is ~1.0 nm (Fig. 4.4A),

whereas the thickness of RGO increases to ~1.7 nm (Fig. 4.4B), confirming the grafting of gelatin molecules on the surface of GO. The thickness of the GO determined by AFM is slightly higher than that from XRD, due to the presence of a water layer between GO and the substrate and perhaps also to the resolution of the AFM tip [231]. The lateral sizes of the GO and RGO sheets are both typically in the range of several hundreds of nanometres to a few micrometres, implicating that the synthesis process did not reduce the size. RGO sheets extracted from the RGO-gelatin hydrogel were characterised by UV-Vis spectroscopy.

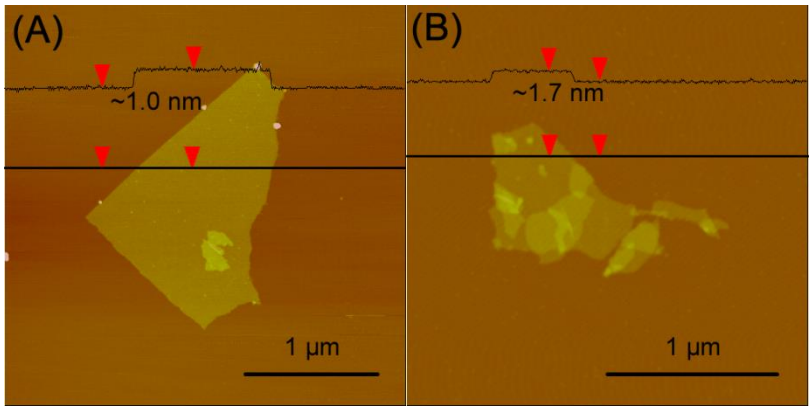

Figure 4.4 Tapping mode AFM topographic images of (A) single-layer nanosheets of GO and (B) RGO extracted from RGG10H with the height profile.

The absorption spectra confirmed the chemical reduction of GO to RGO during the hydrogel formation under the heat treatment (Fig. 4.5). The spectrum of GO shows a absorption peak at 228 nm referring to $\pi \rightarrow \pi^*$ transitions of aromatic C=C bonds and a shoulder at 300 nm ascribed to $n \rightarrow \pi^*$ transitions of C=O bonds [280,281]. In contrast, the peak at 228 nm in the spectrum of RGO shifts to 251 nm, indicating the electronic conjugation is restored [280]. This shift is smaller than that (to 270 nm) of hydrazine reduced GO [282], and that (266 nm) of GO nanosheets reduced in a gelatin solution with an excessive amount of gelatin at 95 ℃ for 24 h

[163]. It indicates a partial restoration of the sp^2 carbon network of RGO in this work, *i.e.*, partial reduction of GO as previously discussed, even at the largest gelatin content used. The disappearance of the peak at 300 nm corresponds to de-oxygenation of the C=O groups of GO nanosheets [283].

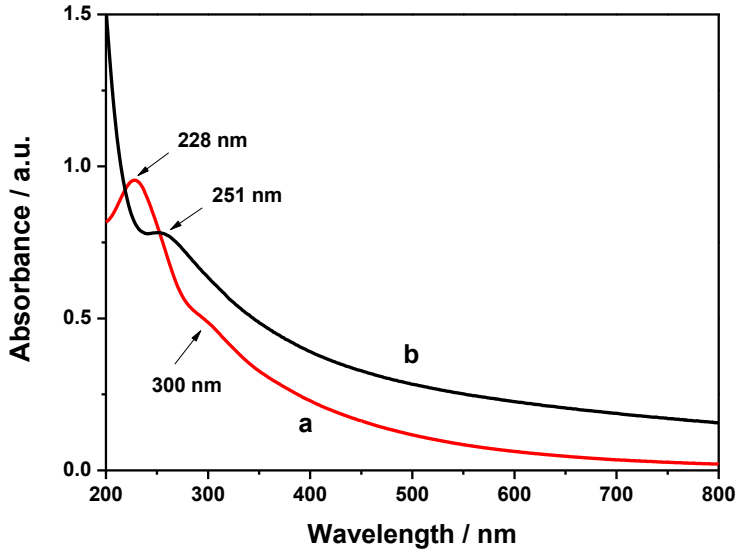

Figure 4.5 UV-Vis absorption spectra of (a) GO and (b) RGO (extracted from RGO-gelatin hydrogel, RGG10H) aqueous suspension at a concentration of 0.1 mg mL^{-1}.

TGA was used to determine the composition of the RGO sheets extracted from the RGO-gelatin hydrogels, and the results are shown in Fig. 4.6. The weight losses below 100 ℃ are all considered due to the evaporation of absorbed water. The TGA curve of GO shows its major weight loss (~34 wt.% of the dried sample) at around 210 ℃, attributed to pyrolysis of the oxygen-containing functional groups generate CO, CO_2 and steam [284]. As the temperature is further increased, it shows a very slow change in the weight. Gelatin shows a major weight loss (~64 wt.% of the dried sample) in the region from 250 ℃ to 500 ℃. The TGA curves of all the three RGOs can be divided to two major stages in terms of weight loss. The first occurs between

140 ℃ and 250 ℃, and the second appears from 250 to 500 ℃. One can deduce that the first loss is mainly attributed to the pyrolysis of the functional groups on the GO while the latter is mainly due to the pyrolysis of the gelatin chains grafted on the RGO sheets. The RGO extracted from the hydrogel with a higher gelatin content exhibits a less weight loss (RGG10 < RGG5H < RGG2H) from 140 ℃ to 250 ℃, in coordination to the pyrolysis of the relatively lower content of GO. In reverse, the corresponding RGO has a higher weight loss (RGG10 > RGG5H > RGG2H) in the range of 250–550 ℃, in accordance with the pyrolysis of the gelatin. The weight percentages of gelatin molecules grafted on the RGO sheets are calculated after the elimination of the absorbed water, which are 31.7, 46.4 and 51.5 wt.% for the hybrid nanosheets extracted from RGG2H, RGG5H and RGG10H, respectively. This further clarifies that a fraction of gelatin in the hydrogel covalently bonded to the graphene nanosheets and the rest interacted with each other and RGO through physical bonding.

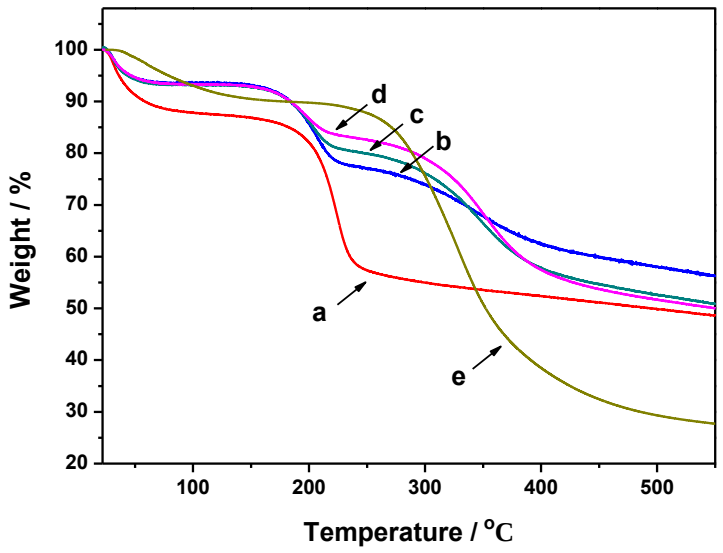

Figure 4.6 TGA curves of (a) GO, (b-d) RGO (extracted from corresponding RGG2H, RGG5H and RGG10H, respectively), and (e) gelatin.

Fig. 4.7 demonstrates that the evolution of the form of the RGO-gelatin hydrogels before and after heat treatment during the hydrogel synthesis. A precursor of RGG2H, a mixture of GO and gelatin suspension (Fig. 4.7A), remains as a sol before heating. In contrast, the precursors of RGG5H and RGG10H are hydrogels (Figs. 4.7B and C) after physically mixing the two components (confirmed by the tube inversion method), in which the physically bonding is strong enough to form the hydrogel due to the appropriate gelatin content as described in Chapter 3. After heat treatment, the three RGO-gelatin hydrogels are obtained. Their black color is also evidence of the reduction of GO in the hydrogel compared with dark brown color of their GO precursors. For all the three hydrogel precursors, chemical reactions occurred between abundant NH_2 groups on gelatin chains and carboxyl and epoxy groups on the GO nanosheets during the heating process (illustrated in Scheme 4.1), leading to the reduction of GO. In RGG2H, this also results in the formation of a stable 3D network. All the three RGO-gelatin hydrogels are formed by RGO sheets connecting the adjacent gelatin chains by the covalent bonds and hydrogen bonding as depicted in Scheme 4.2.

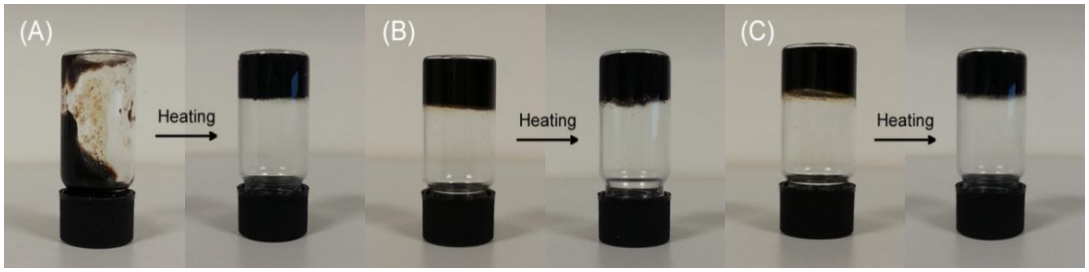

Figure 4.7 Illustration of the evolution of the formation of the hydrogels: (A) RGG2H, (B) RGG5H and (C) RGG10H before and after heat treatment during the hydrogel synthesis. Diameter of the containers: 15 mm.

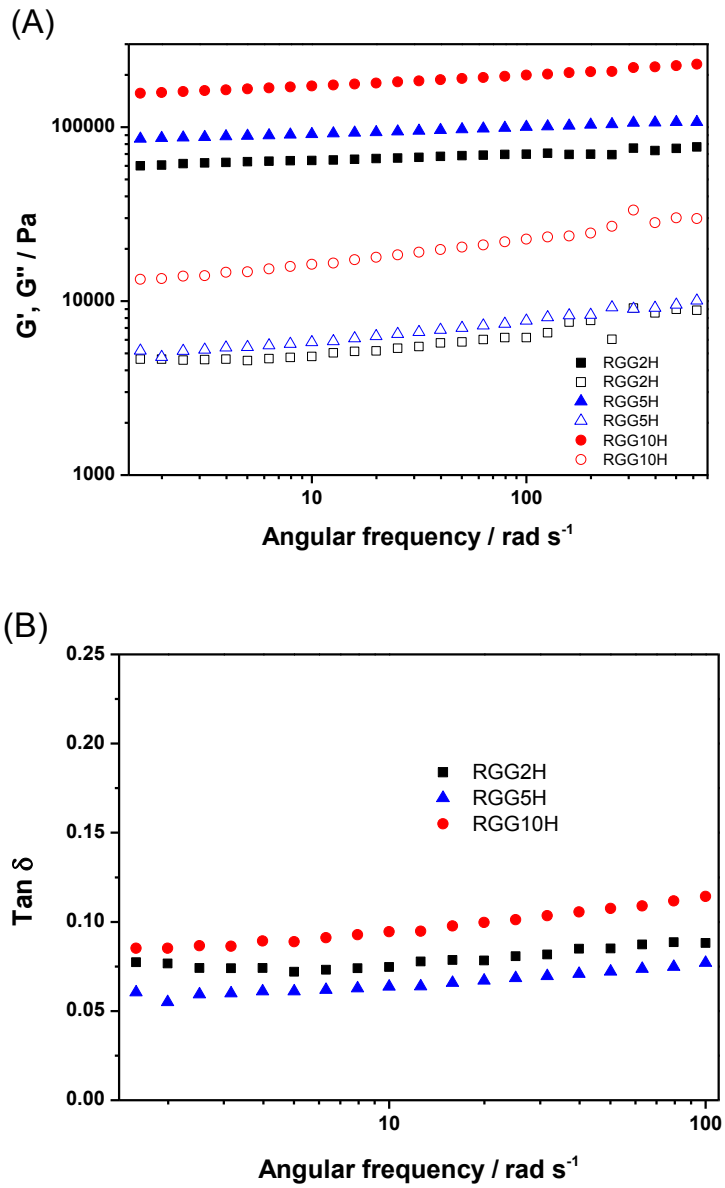

Figure 4.8 (A) Storage moduli *G'* (solid) and loss moduli *G''* (hollow), and (B) loss factor tan δ of lyophilised hydrogels.

Fig. 4.8A shows the rheological properties of RGGHs with different gelatin contents. The RGO-gelatin hydrogels exhibit typical rheological behaviour of hydrogels. The storage modulus is nearly frequency independent, showing only slight increase as the angular frequency increases. The loss factor tan δ (tan δ = *G''*/*G'*) is also relatively independent to the angular frequency in the testing range (Fig. 4.8B). The storage moduli are one order of magnitude greater than the

corresponding loss moduli, indicating the hydrogels are stable networks and more elastic than viscous [174]. The storage moduli of the RGGHs increase as the content of gelatin increases, while remaining a similar water content (~98.0–98.8 wt.%). The storage modulus of RGG10H is 172.3 kPa at 10 rad s^{-1}, which is 89% greater than 91.1 kPa of RGG5H and 169% greater than 64.4 kPa of RGG2H, respectively. The more gelatin are introduced to the system, the more chemical crosslinking sites between the gelatin chains and GO nanosheets are created, leading to a more stable network and less mobility of the macromolecular chains.

Previously, we reported that physically crosslinked GO-gelatin hydrogels had storage moduli of 114.5 kPa and 3.2 kPa with the same composition of RGG10H and RGG5H, respectively. The storage modulus of RGG10H is 50% higher than that of the physically crosslinked counterpart hydrogel, while the value of RGG5H is 27-fold higher than that of its GO counterpart, as shown in Fig. 4.9. The results indicate the covalent bonds considerably enhance the mechanical performance of the RGGHs compared to the physically crosslinked counterpart hydrogels, in particular those weaker hydrogels with a lower gelatin concentration. The storage moduli of these RGO-gelatin nanocomposite hydrogels are comparable with that (7.5 kPa) of adipose tissue (Table 1.1), indicating the possible applications in the relevant tissue engineering.

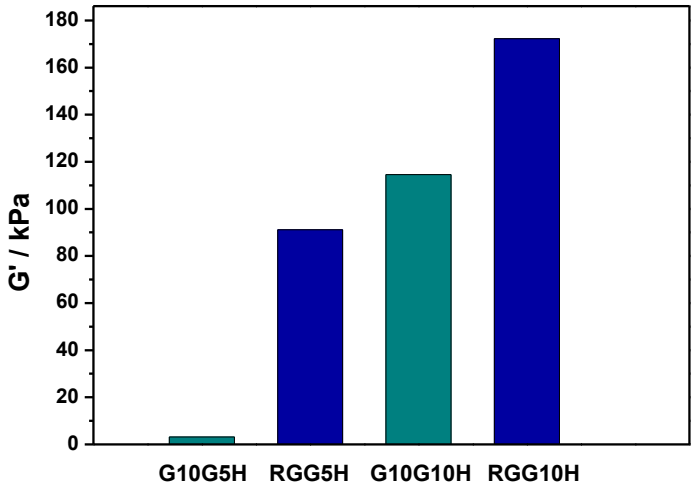

Figure 4.9 Storage moduli comparison between the physically crosslinked GO-gelatin nanocomposite hydrogels (G10G5H and G10G10H) and RGO-gelatin nanocomposite hydrogels (RGG5H and RGG10H).

The rheological data are also used to determine the crosslinking density, *N*, and the number average molecular weight of polymer chains between the crosslinkers in the hydrogel, $\overline{M}_c$. The same rubber elasticity theory [251] and analysis method employed in Chapter 3 is used here. By applying the experimental values of *G'* to equations 3.1 and 3.4, the results are determined and shown in Table 4.1.

Table 4.1 Crosslinking densities and number average molecular weights of polymer chains between the adjacent crosslinking sites in the RGO-gelatin hydrogels with varying compositions.

Sample	Gelatin (mg mL^{-1})	GO (mg mL^{-1})	Storage Modulus, *G'* (kPa)	Crosslinking Density, *N* ($\times 10^{23}$ m^{-3})	Number Average Molecular Weight, $\overline{M}_c$ (g moL^{-1})
RGG2H	2	10	64.4	99	122
RGG5H	5	10	91.1	139	214
RGG10H	10	10	172.3	263	226

For the hydrogels with a fixed graphene content, *N* increases from 99 $\times 10^{23}$ m^{-3} for RGG2H to 139 $\times 10^{23}$ m^{-3} for RGG5H and 263 $\times 10^{23}$ m^{-3} for RGG10H.

Correspondingly, $\overline{M}_c$ between the neighboring crosslinking sites (RGO nanosheets) increases from 122 to 214 and 226 g moL^{-1}. There is a high quantity of covalent and non-covalent crosslinking sites for the formation of the RGO-gelatin hydrogel, due to the abundant functional groups from both GO sheets and gelatin chains. This gives rise to the relatively high values of N and relatively low values of $\overline{M}_c$ presented in Table 4.1. As one would expect, a higher crosslinking density leads to a stiffer hydrogel. The mechanical properties of the hydrogels could be modulated by varying the composition and hence controlling the crosslinking density, similar to our previous observation for GO-gelatin nanocomposite hydrogels in Chapter 3.

Fig. 4.10 shows the morphology of a lyophilised GO suspension and RGO-gelatin hydrogels under SEM. The RGGHs consist of the same concentration of GO in water as the neat GO suspension, regardless the difference in gelatin content. All the lyophilised samples show porous structure despite of the broad variation in the pore size. The porous structure (7.4 ± 3.5 μm) of the lyophilised GO suspension (Fig. 4.10A) was formed due to the structural changes during the drying stage; the GO sheets contact to each other to form the network presumably facilitated by the hydrogen bonding between GO sheets and the residual hydrogen-bonded water molecules between GO sheets [246]. Fig 4.10B shows a lyophilised GO-gelatin suspension, a precursor of RGG2H prior to the gelation process. It has a similar porous structure (7.1 ± 4.1 μm) to the lyophilised GO suspension although the additional gelatin also contributes to the formation of hydrogen bonds in addition to water molecules. In contrast, the lyophilised RGG2H (Fig. 4.10C) possesses much smaller pores, with an average pore size of 2.3 ± 1.1 μm. This is because when the hydrogel is formed, GO sheets crosslink with gelatin chains to form a much finer network structure, and the stable network within the hydrogels restricts the growth of

ice crystals during the freezing process [176]. RGG5H has a slightly lower average pore size (1.7 ± 0.7 μm) to RGG2H, whereas the value of RGG10H is significantly greater (3.2 ± 1.2 μm). The average pore sizes of RGG5H and RGG10H are much smaller than those (6.2 ± 4.5 μm and 7.7 ± 5.4 μm, respectively) of physically crosslinked GO-gelatin nanocomposite hydrogels with the same composition reported in Chapter 3. This may be due to reconstruction of the microstructure of RGO-gelatin nanocomposite triggered by the movement of graphene sheets and gelatin chains during the heating process, though there is no notable volume change before and after hydrogel formation. The finer structure also contributes to the superior mechanical performance of the RGO-gelatin nanocomposite hydrogels as opposed to those of the GO-gelatin nanocomposite hydrogels as previously discussed.

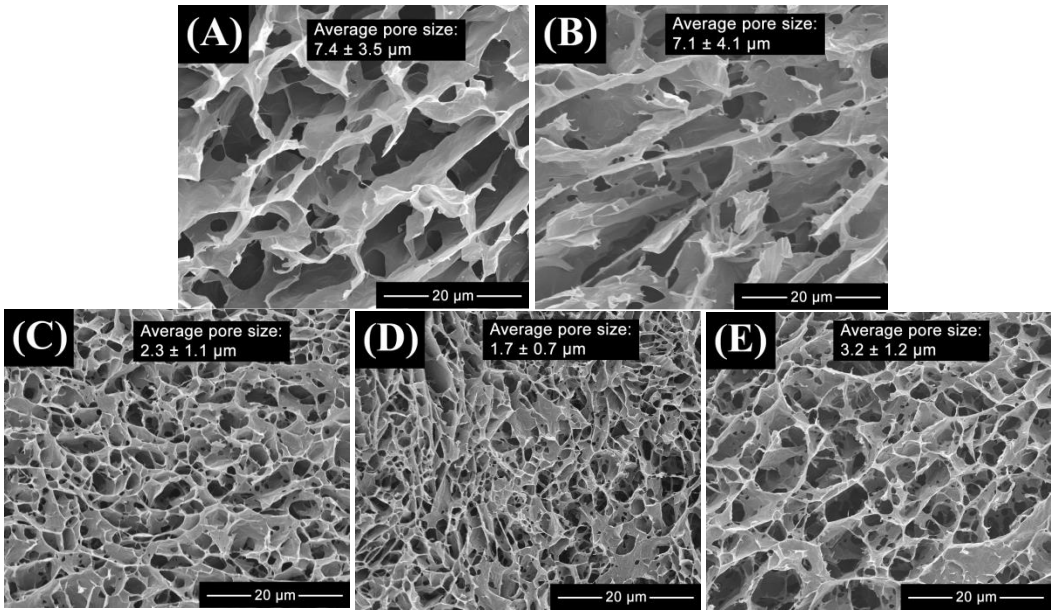

Figure 4.10 SEM images of cross-section surfaces of (A) lyophilised GO suspension (10 mg mL^{-1}), (B) lyophilised precursor mixture of RGG2H before gelation (containing 10 mg mL^{-1} GO and 2 mg mL^{-1} gelatin), (C) lyophilised RGG2H, (D) RGG5H, and (E) RGG10H.

Since the hydrogel RGG10H has the highest storage modulus in the current study, it is used for subsequent investigation of the swelling and degradation behaviour. Fig. 4.11A shows the water swelling behaviour of the lyophilised hydrogel (RGG10H). The swelling curve is steep at the initial state and then turns to a plateau. It reaches equilibrium by 24 h at a swelling weight ratio of 44.7. Fick's law (equation 4.2) [285] was used to describe water swelling behaviour of the RGO-gelatin hydrogel.

$$M_t/M_{eq} = 1 - (8/\pi^2)\sum_{m=0}^{\infty} \frac{exp\left[-\pi^2(2m+1)^2 Dt/L^2\right]}{(2m+1)^2} \qquad (4.2)$$

where M_t is the swelling degree at time t, M_{eq} is the equilibrium swelling degree, D is the diffusion coefficient of water molecules, and L is the thickness of the specimens. The diffusion coefficient, D, derived from equation (4.2), is 8.2×10^{-10} m^2 s^{-1}. It can be seen from Fig. 4.11B that the theoretical values fit the experimental data very well. Thus, one can predict the swelling behaviour of the RGO-gelatin hydrogels by using the Fick's law.

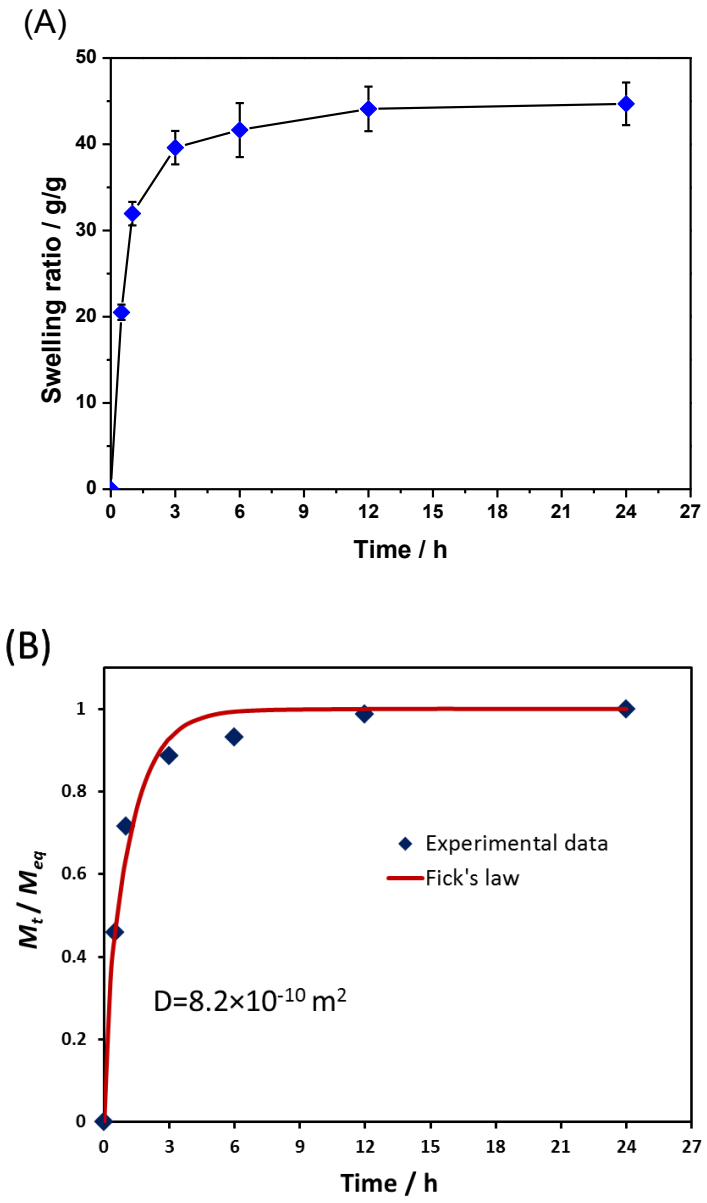

Figure 4.11 (A) Swelling behaviour of a RGO-gelatin hydrogel (RGG10H), and (B) M_t/M_{eq} against time *t* for RGG10H. Error bar indicate standard deviation on three replicate samples.

Fig. 4.12 shows the degradation profiles of the hydrogel RGG10H at body temperature in the PBS solutions with and without the presence of collagenase. In the initial 2 h, the sample undergoes almost the same degradation rate with and without the enzyme, which can be interpreted as weight loss of the loose gelatin molecules due to diffusion. Afterwards, there is a much more considerable weight

loss of the hydrogel with collagenase than that without the enzyme. After 24 h, 29% of the original weight lost in the collagenase degradation, which is 70% higher than the value (17%) obtained without enzyme. These results also show that the RGO-gelatin hydrogel is more stable than GO-gelatin methacrylate hydrogels with only 30% weight [192] remaining after the same period of time. This can be ascribed to the higher crosslinking density in the former. Since the collagenase attacks peptide linkages [192], the main weight loss is mainly due to the degradation of gelatin molecules although there might be a small amount of RGO sheets detached from the bulk hydrogel.

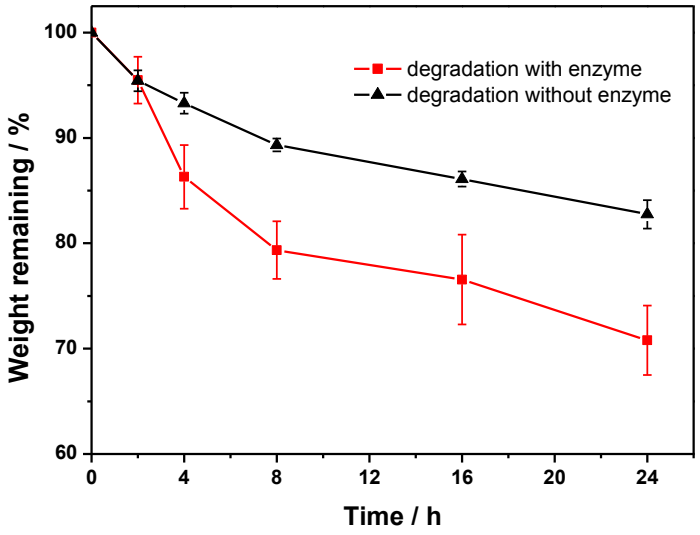

Figure 4.12 Degradation profiles of the same hydrogel with and without collagenase in PBS solution. Error bar indicate standard deviation on three replicate samples.

4.4 Conclusions

RGO-gelatin nanocomposite hydrogels were synthesised by heating the mixture of a GO suspension and a gelatin solution at various weight ratios at 95 ℃ for 24 h, without using a chemical crosslinker. GO acted as a multifunctional crosslinker to connect the surrounding gelatin chains to form a 3D network, while gelatin acted

simultaneously as a reducing agent and a biocompatibiliser for GO, as well as a building component of the hydrogel. The chemical (mainly) and physical crosslinking between graphene sheets and gelatin chains within the hydrogel was confirmed by FT-IR, Raman spectroscopy, AFM, TGA and UV-Vis spectroscopy. SEM image revealed the internal porous morphology of the hydrogels. The storage modulus of the hydrogel was tuneable by changing the gelatin concentration in the precursor mixture. With the concentration of gelatin of 10 mg mL^{-1} and the water content of 98 wt.%, the highest storage modulus of RGO-gelatin hydrogels was 172.3 kPa, 50% higher than that of physical crosslinked GO-gelatin nanocomposite hydrogels in Chapter 3. The freeze-dried hydrogel reached equilibrium in 24 h at a swelling weight ratio of 44.7, and the water swelling behaviour follows Fick's diffusion law. The hydrogels demonstrated an enzyme-favourite degradation with 71% weight remained after degradation with collagenase for 24 h. The biodegradable RGO-gelatin hydrogels could have potential in tissue engineering and drug delivery.

Chapter 5. Graphene oxide-polyamidoamine dendrimer nanocomposite hydrogels

5.1 Introduction

In Chapter 3, GO was used as a physical crosslinker to form physically crosslinked GO-gelatin nanocomposite hydrogels. And the resulting hydrogels exhibited high mechanical properties. To develop new physically crosslinked hydrogels with a higher mechanical performance, GO-PAMAM nanocomposite hydrogels were synthesised through a facile and fast one-step self-assembly method without any organic crosslinkers involved. PAMAM dendrimer could possess a high charge density on its globular surface when it was protonated, and so the multiple electrostatic interactions between GO sheets and PAMAM molecules could provide stronger driving force for network formation and exhibiting self-healing ability, compared to that between GO sheets and gelatin molecules. The PAMAM dendrimers were synthesised, and their chemical structure was characterised by mass spectrometry (MS), nuclear magnetic resonance spectroscopy (NMR) and potentiometric titration. The chemical structure, morphology, mechanical properties and gelation mechanisms of GO-PAMAM nanocomposite hydrogels were investigated by FT-IR, Raman spectroscopy, XRD, SEM and rheometry. Their self-healing property was also demonstrated.

5.2 Experimental section

5.2.1 Materials

Graphite powder and the other chemicals used for GO preparation were the same as in Chapter 3. Ethylenediamine (EDA) (≥ 99.5%), methanol (≥ 99.9%),

methylacrylate (MA) (99%) and deuterium oxide (D_2O) (99.9 atom% D) were all obtained from Sigma-Aldrich Corporation.

5.2.2 Preparation of PAMAM dendrimer G4.0

The PAMAM dendrimer Generation 4.0 (G4.0) was prepared following a method described in the literature [200]. Briefly, an EDA methanol solution was prepared and cooled to −20 ℃, to which methanolic MA was added by drop-wise under agitation. The resultant solution was reacted at 25 ℃ for 2 days and at 40 ℃ for 4 days. The excess MA and solvent were removed by vacuum distillation below 40 ℃, leading to a half-generation dendrimer (multi-ester) [201]. Then the multi-ester methanol solution was prepared and cooled down to −20 ℃. The solution was slowly added to the pre-cooled EDA methanol solution, which was kept below −10 ℃. The resulting mixture solution was kept at 25 ℃ reacting for 2 days and afterwards at 40 ℃ for 4 days, before the removal of excess EDA and solvent. As a result, a pale amber-coloured syrup, a full-generation dendrimer [201], was obtained. This whole process was further replicated four times to achieve the PAMAM dendrimer G4.0 for subsequent studies.

5.2.3 Preparation of GO-PAMAM nanocomposite hydrogels

GO was synthesised using graphite powder by the modified Hummers' method [152,155], and subsequently washed and purified as described in Chapter 3. GO-PAMAM nanocomposite hydrogels were synthesised by one-step self-assembly. Typically, a PAMAM water solution (0.5 mL) with a desired concentration was added drop by drop into a GO suspension (5.5 mL) under stirring to form a hydrogel in about 30 s. Two sets of hydrogels were prepared. In one set, the GO concentration in the hydrogel was 10 mg mL^{-1}, and the PAMAM concentration varied as 0.5, 1, 5,

10, 20 and 30 mg mL^{-1}. In the other set, PAMAM was kept at 10 mg mL^{-1}, while GO varied as 6, 8 and 10 mg mL^{-1}. The hydrogel products were denoted as G*m*D*n*H, in which *m* and *n* defined the concentrations of graphene oxide and PAMAM, respectively.

5.2.4 Structural characterisation

The dendrimer (5 mg mL^{-1}) was dissolved in D_2O and analysed on a NMR spectrometer (Bruker DRX-500) at 25 ℃ for ^1H with the solvent proton signal as an internal reference. The spectrometer was equipped with an inverse geometry 5 mm VSP probe with a single z-gradient. The operation software version was TOPSPIN 1.3. The mass spectrum of the PAMAM dendrimer was obtained on a Bruker Reflex III MALDI-TOF mass spectrometer. The matrix solution was sinapic acid (10 mg mL^{-1}) in acetonitrile: water: trifluoroacetic acid (weight ratio, 50: 50: 0.1). The concentration of PAMAM dendrimer in the matrix solution was 1 mg mL^{-1}. Before testing, the mass spectrometer was calibrated with the matrix solution containing known peptides. Titrations were performed on a Multiparameter (SevenExcellence™) and an INLAB Expert Pro-ISM pH electrode (Mettler Toledo) at ambient temperature (23 ± 1 ℃) in nitrogen environment. PAMAM dendrimer (13 mg) firstly was dissolved in a 10 mL 0.1 M NaCl solution. Here, 0.1001 M HCl and 0.0999 M NaOH were used for forward and back titrations, respectively. GO (40 mg) was dispersed in 10 mL 0.1 M NaCl solution by 30 min sonication before the suspension was tuned using the standard NaOH solution to pH = 10, and then titrated by the standard HCl solution to pH = 2.30. The titrant was added by 0.03 mL portions using a pipet (Eppendorf Research Plus, Eppendorf, Germany). Laser scattering particle sizing was performed on a Coulter LS130 (ranging from 0.1 to

900 μm) by 3 runs on graphite powder and a fully exfoliated GO aqueous suspension of 0.5 mg mL^{-1}, respectively.

FT-IR, XRD, SEM and Raman spectroscopy were carried on a set of same instruments using the same settings as described in Chapter 3. Freeze-dried samples were used for these structural and morphological analyses, and they were prepared by the same method as in Chapter 3. In SEM analysis, the pore sizes were averaged from at least 40 pores using ImageJ software. Rheological tests were conducted on a rheometer (MCR 301, Anton Paar) using 25 mm parallel plates at the angular frequency range of 0.1–100 rad s^{-1}. The strain was set at 0.1% within the linear viscoelastic zone, while the test gap was fixed at 2.0 mm.

5.3 Results and discussion

5.3.1 Characterisation of PAMAM dendrimer G4.0

Synthesis of the PAMAM dendrimer was a two-step process, using an initiator core, EDA. After a continuous process, the PAMAM dendrimer with $–NH_2$ terminal groups was obtained. The ^1H NMR spectrum (500 MHz, D_2O) of the prepared PAMAM dendrimer (Fig. 5.1) shows the chemical shifts at δ = 2.36 (H_c), 2.55 (H_a and H_e), 2.66 (H_g), 2.75 (H_b), 3.18 (H_f) and 3.22 ppm (H_d), which can be identified with the protons assigned with the same letters in the theoretical PAMAM dendrimer fragment. These chemical shifts are consistent with the results reported in the previous papers [286,287], initially verifying the molecular structure and confirming the successful synthesis of the PAMAM dendrimer G4.0.

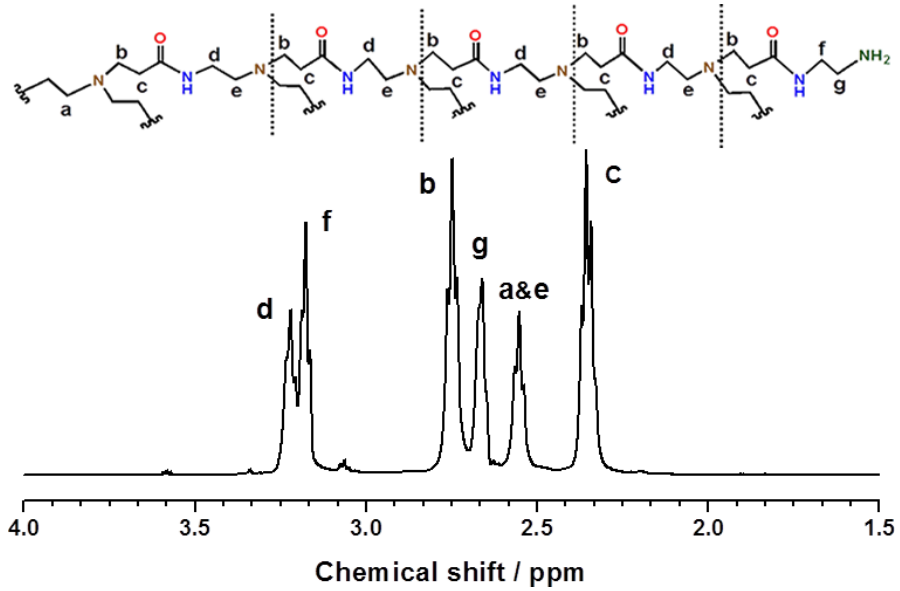

Figure 5.1 ^{1}H NMR spectrum of the PAMAM dendrimer G4.0 and peak assignments corresponding to the protons denoted in the fragment of a PAMAM dendrimer.

The molecular weight of the PAMAM dendrimer G4.0 prepared, determined by MS, is 9,534 Dalton (Fig. 5.2), which is lower than the theoretical value of 14,196 for PAMAM dendrimer G4.0 with an ideal structure [200]. The deviation of the resultant molecular weight from the original synthesis design was presumably due to incomplete Michael addition, intramolecular cyclisation, and fragmentation arising from the retro-Michael reaction [200]. This deviation could also be partially attributed to the measurement system as reported in the literature [288].

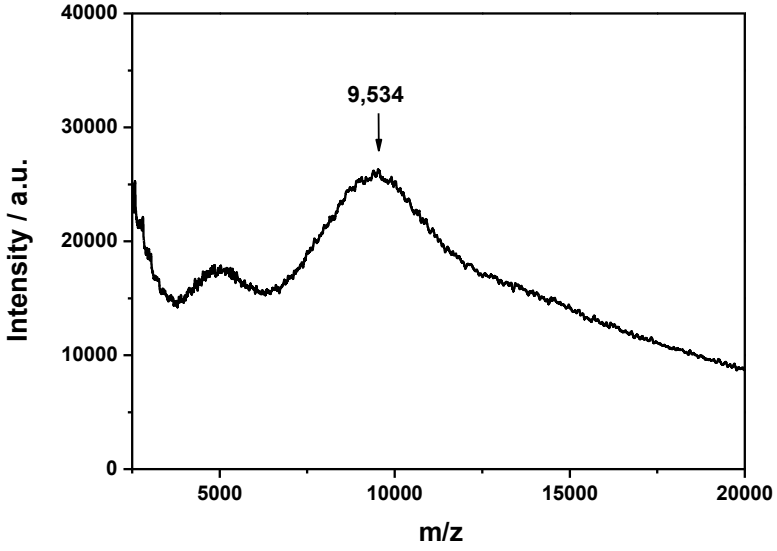

Figure 5.2 MALDI-TOF mass spectrum of PAMAM dendrimer G4.0.

Curve a in Fig. 5.3 shows that the PAMAM dendrimer is basic (pH = 9.26) in an aqueous solution (1.3 mg mL^{-1}) before titration. The turning points during the back-titration (curve b) show the distinctive start and end points of protonation, which is consistent with the previous report [200] for PAMAM dendrimers. According to the first derivative peaks, the start and end points of deprotonation are at pH = 4.05 and pH = 7.51 for tertiary amines and at pH = 7.51 and pH = 10.51 for primary amines, respectively. Because the geometric structure of the PAMAM dendrimer G4.0 is globular, only the peripheral primary amine ($-NH_2$) groups can participate in electrostatic attractions with GO sheets. The number of $-NH_2$ groups present in the dendrimer can be calculated according to the consumption of OH^- ions during deprotonation of $-NH_2$ groups and the molecular weight estimated from MS [289]. Considering the minimum volumetric addition (0.03 mL) during the titration, the number of in $-NH_2$ groups our PAMAM dendrimer is 46 ± 2. This number is lower than the theoretical value (64) of PAMAM dendrimer G4.0, because of the defects and incomplete reactions as described earlier [200].

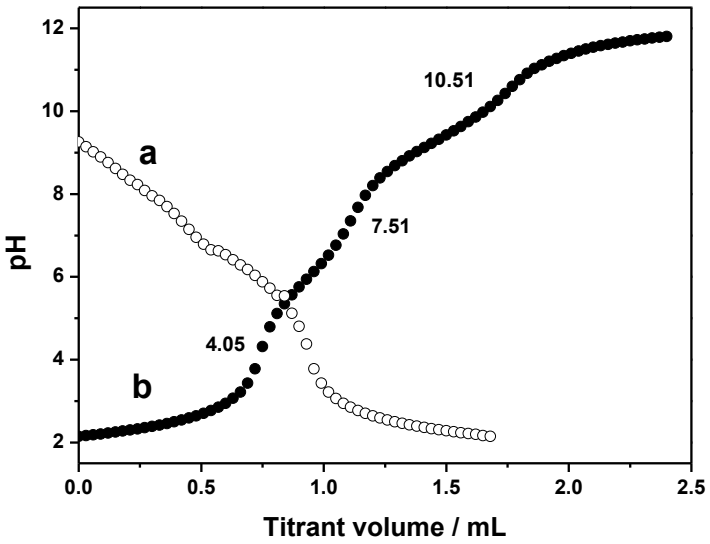

Figure 5.3 Potentiometric acid-base titration of PAMAM. The forward titration (curve a) and the back titration (curve b) were performed using a 0.1001 M HCl solution and a 0.0999 M NaOH solution, respectively.

5.3.2 Characterisation of GO

The GO nanosheets used to synthesise the nanocomposite hydrogels have been characterised by AFM and TGA in Chapter 3. The single GO nanosheets have a thickness of 1.0 nm and a typical length of one to several microns (with a new AFM profile inset shown in Fig. 5.4). The content of oxygenated groups in GO was approximately 55 wt.% according to TGA analysis. As shown in Fig. 5.4, the raw material, graphite powder, was measured to be between 1.8 and 50 μm in particle size. The majority of the GO nanosheets range in size from 2.2 to 20 μm with a mean of 5.5 μm. This laser sizing measurement records the hydrodynamic diameter of particles by assuming these particles are spherical in shape.

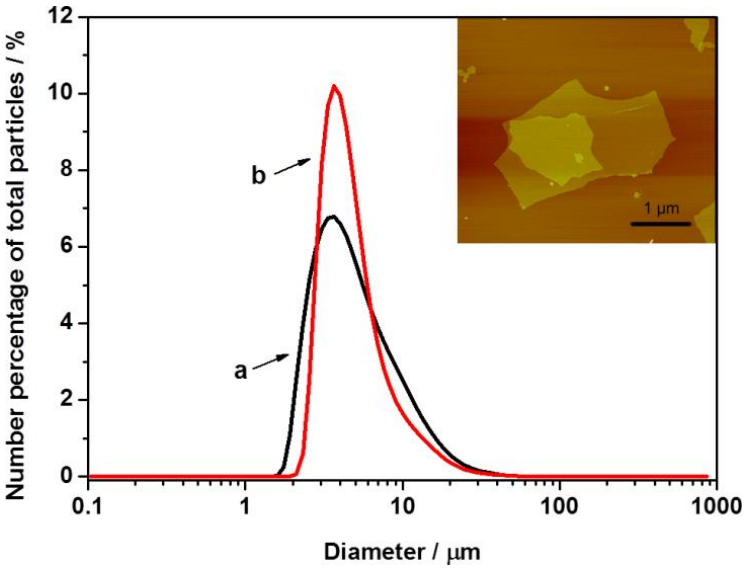

Figure 5.4 Laser scattering particle sizing profiles of (a) graphite powder and (b) GO nanosheets in an aqueous solution, with an inset of the tapping mode AFM topographic image of two layers of GO.

The result of GO titration is shown in Fig. 5.5. The titrant (HCl) consumption is mainly attributed to the protonation of hydroxyl and carboxyl groups [290]. The start point of protonation (at pH = 8.24) is attributed to hydroxyl groups while the end point (at pH = 4.76) is due to more acidic carboxyl groups. However, there is no clear transition point between the two steps, probably because of the surface heterogeneity of GO [290,291]. This result indicates that the GO suspension is negatively charged above pH = 4.76.

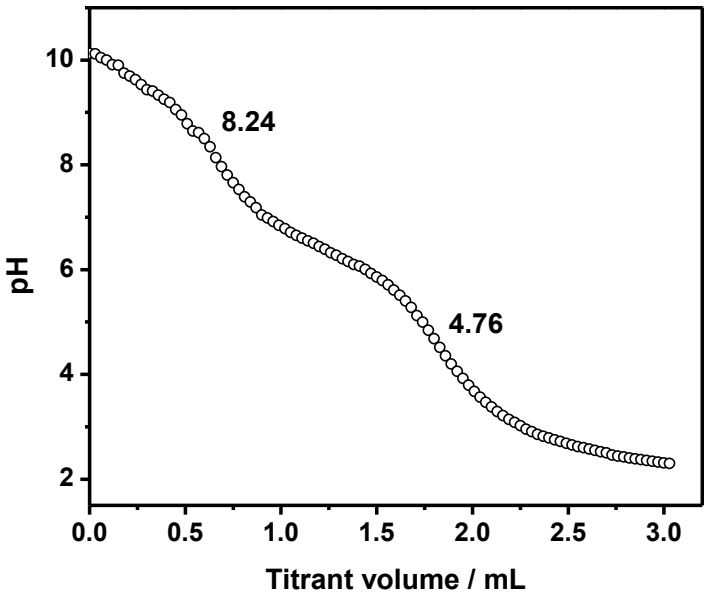

Figure 5.5 Acid-base titration of GO, using a 0.1001 M HCl solution.

5.3.3 Characterisation of GO-PAMAM nanocomposite hydrogels

The GO-PAMAM nanocomposite hydrogels with a fixed concentration of GO were prepared by adding a small portion of a PAMAM solution into an aqueous GO suspension under stirring. Stable hydrogels, G10D1H, G10D5H, G10D10H and G10D20H, were formed and confirmed by the tube inversion test [248] (Fig. 5.S1). Incorporation of less PAMAM dendrimer, G10D0.5H, failed to form a hydrogel, but a sol (Fig. 5.S1). FT-IR spectra of graphite, GO, neat PAMAM and lyophilised GO-PAMAM nanocomposite hydrogels are presented in Fig. 5.6. Graphite only possesses a weak O–H stretching at 3400 cm^{-1} which is from residual water. GO (curve b) shows the absorption peaks of C=O (1731 cm^{-1}), C=C (1619 cm^{-1}), C–O–C (1276 cm^{-1}) and C–O (1050 cm^{-1}), as well as O–H (3200–3400 cm^{-1}) [271,292]. The spectrum g shows typical characteristics of PAMAM: the vibration peaks for C=O stretching (1631 cm^{-1}), C(O)NH (1545 cm^{-1}) and C–H stretching (2933 cm^{-1}), as well as N–H stretching of primary amine (3263 cm^{-1}) and anti-symmetric substituted primary amine (3071 cm^{-1}) [293]. This further confirms that the PAMAM dendrimer

was successfully synthesised. After incorporation of PAMAM, the C=O peak of GO (1731 cm^{-1}) diminishes and vanishes completely in G10D20H (curve f) and G10D30H (curve g) containing 67 wt.% and 75 wt.% PAMAM, respectively. This may be explained by the transformation of carboxyl functional groups from GO to carboxylate complex *via* associating with the amino groups from PAMAM [238,239]. Emergence of the C(O)NH bending at 1545 cm^{-1} and C=O amide I vibration at 1631 cm^{-1} in curves b-e for the nanocomposites also confirms the incorporation of PAMAM into the hydrogels.

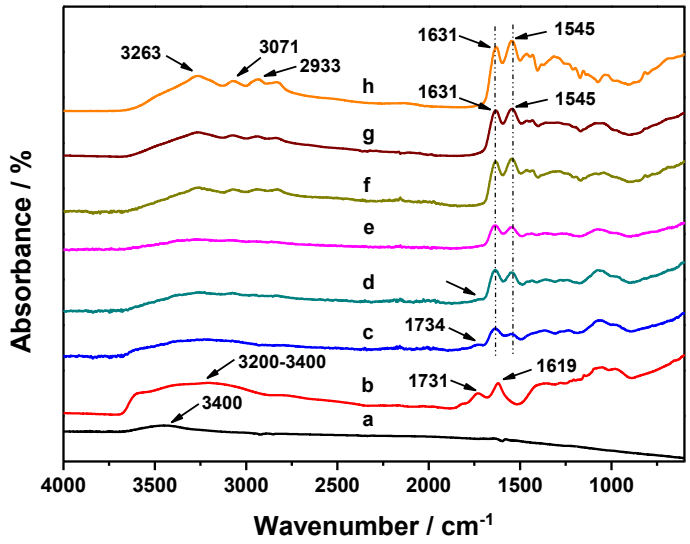

Figure 5.6 FT-IR spectra of (a) graphite, (b) lyophilised GO and GO-PAMAM nanocomposite hydrogels: (c) G10D1H, (d) G10D5H, (e) G10D10H, (f) G10D20H, (g) G10D30H, and (h) neat PAMAM dendrimer.

Fig. 5.7 illustrates Raman spectra of each sample. The intense G band (at 1580 cm^{-1}) of graphite (curve a) is ascribed to in-phase vibration of the E_{2g} mode of the lattice, while a small D band at1353 cm^{-1} is contributed to the A_{1g} mode [240,294,295]. After oxidation and exfoliation, both bands turn broader (curve b). The intensity ratio (I_D/I_G) increases significantly from 0.08 for graphite to 0.79 in

GO, implying a much higher degree of lattice disorder and defects in the latter [241,296]. Furthermore, the G band of graphite moves to 1598 cm^{-1}, and a new D' band at 1620 cm^{-1} appears in GO, because of the isolation of double bonds from higher-energy functional groups in GO sheets [241,296]. GO-PAMAM nanocomposite hydrogels possess similar spectra (curves c-g) to GO. With an increasing PAMAM content, the G band gradually shifts from 1598 cm^{-1} in GO to 1587 cm^{-1} in G10D30H, attributable to the charge transfer from PAMAM to GO sheets [181]. These results indicate the electrostatic interactions between GO and PAMAM.

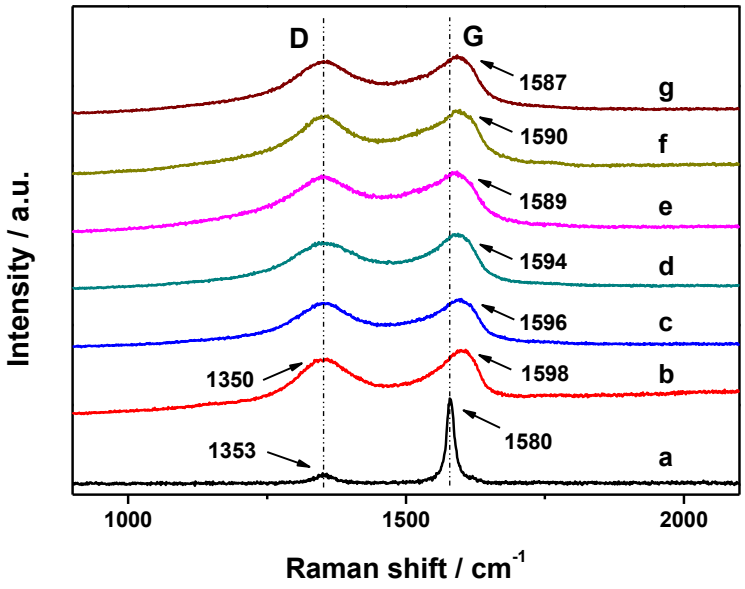

Figure 5.7 Raman spectra of (a) graphite, (b) lyophilised GO and GO-PAMAM nanocomposite hydrogels: (c) G10D1H, (d) G10D5H, (e) G10D10H, (f) G10D20H, (g) G10D30H, and (h) neat PAMAM dendrimer.

Figure 5.8 depicts XRD traces of the samples. A strong peak is observed at 26.4 ° for graphite corresponding to an interlayer distance (d_{002}) of 0.34 nm. After oxidation, a typical diffraction peak of graphite oxide is observed at 10.6 ° corresponding to a

d_{002} of 0.83 nm, ascribed to the formation of oxygenated groups on graphene [297]. However, the GO diffraction peak disappears in the XRD traces of lyophilised GO-PAMAM nanocomposite hydrogels, indicating an excellent dispersion and exfoliation of GO in the nanocomposites, noting the high contents of GO in the nanocomposites [298].

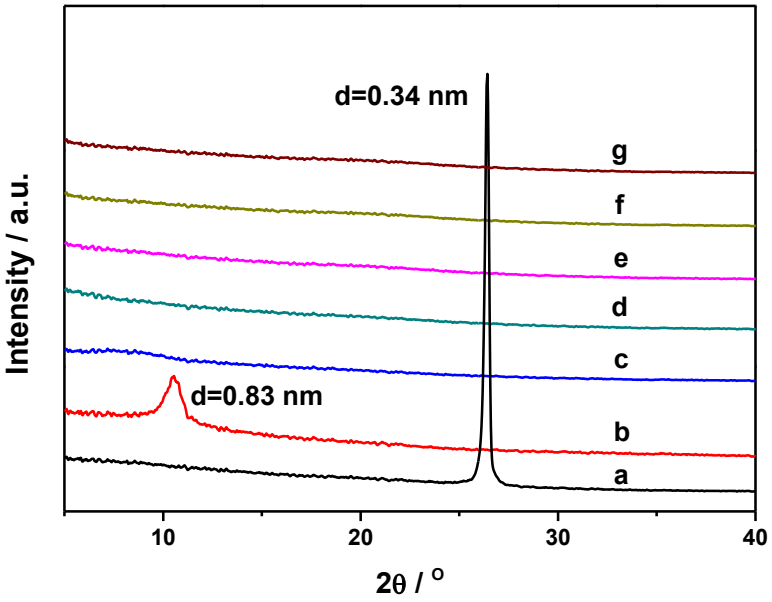

Figure 5.8 XRD traces of (a) graphite, (b) lyophilised GO, and lyophilised GO-PAMAM nanocomposite hydrogels: (c) G10D1H, (d) G10D5H, (e) G10D10H, (f) G10D20H, and (g) G10D30H.

The interior morphologies of the lyophilised samples were observed by SEM, as illustrated in Fig. 5.9. The nanocomposite hydrogels possess interconnected open porous microstructures which vary with the PAMAM content. The morphology of the nanocomposite with the least PAMAM (G10D1H in Fig. 5.9B, pore size 6.1 ± 2.5 μm) has the least change compared to the structure (7.2 ± 3.7 μm) of the lyophilised GO suspension (Fig. 5.9A). In contrast, more changes occur to G10D5H and G10D10H which exhibit much smaller pore sizes (2.4 ± 1.2 and 2.0 ± 0.9 μm, respectively). At higher PAMAM contents, G10D20H (pore size 3.4 ± 1.6 μm) and

G10D30H (pore size 4.9 ± 2.2 μm) show significantly different morphological profiles, with more integral and less porous structures. G10D30H possesses less uniform porous structure than G10D20H, presumably due to the higher dendrimer content. Excess dendrimer may cause inhomogeneous crosslinking between GO and PAMAM in the hydrogel, leaving some regions with more solid contents than others. The porous microstructure in the hydrogel has an important effect on its mechanical properties, which is discussed further subsequently.

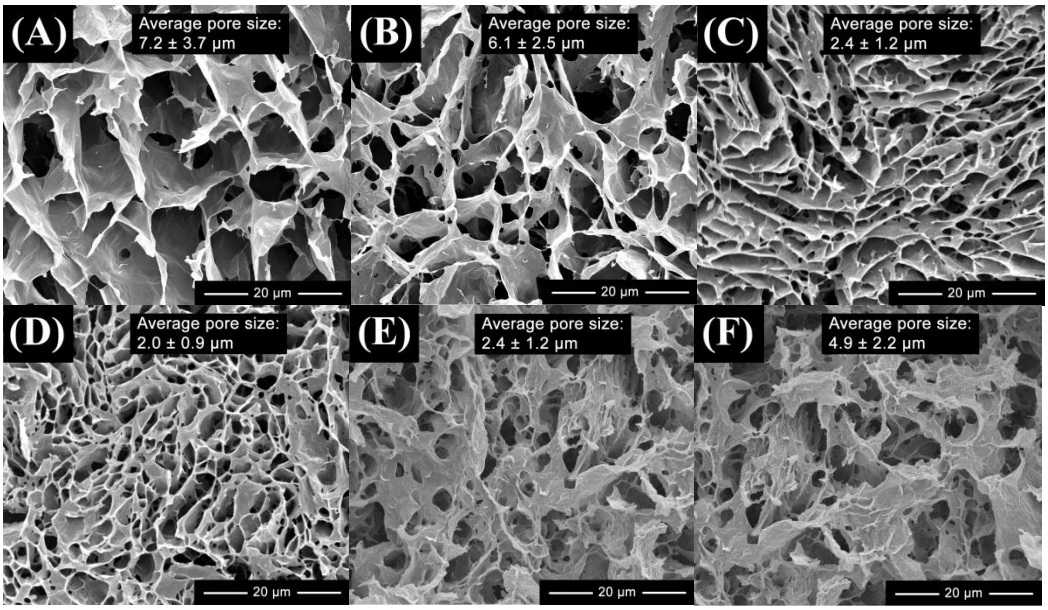

Figure 5.9 SEM images of lyophilised (A) GO suspension and GO-PAMAM nanocomposite hydrogels: (B) G10D1H, (C) G10D5H, (D) G10D10H, (E) G10D20H, and (F) G10D30H.

The hydrogel network is assembled by physically crosslinking positively charged PAMAM dendrimer (mainly $-NH_2$ groups) and negatively charged GO nanosheets (mainly carboxyl groups). Based on the consumption of the acid or the base by GO or PAMAM during their back-titrations (as shown in Fig. 5.5 and 5.3), the ratio of the charge moles per unit weight between GO and PAMAM, is

calculated to be 0.6. The strong electrostatic attractions between $-NH_2$ groups at the edge of globular PAMAM and –COOH groups from GO result in the formation of a robust hydrogel (Scheme 5.1). The charge capacity ratios of GO to PAMAM in the hydrogels are 6/1, 6/5, 6/10, 6/20 and 6/30 for G10D1H, G10D5H, G10D10H, G10D20H and G10D30H, respectively. Since G10D0.5H cannot form a hydrogel, 6/1 is considered as the approximate critical gelation ratio for this system. As expected for many physically crosslinked hydrogels these GO-PAMAM nanocomposite hydrogels demonstrated self-healing capability, and the self-healing process was relatively fast (Fig. 5.S2) due to the multiple physical crosslinks, *e.g.*, electrostatic interactions [299].

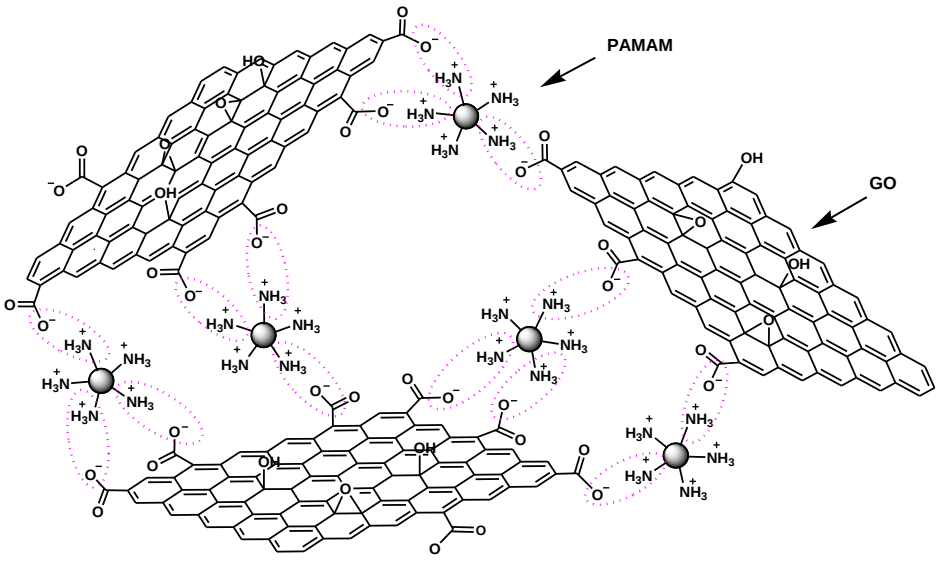

Scheme 5.1 Illustration of 3D-network GO-PAMAM nanocomposite hydrogel formed mainly by the electrostatic interactions between the deprotonated carboxyl groups of GO and protonated amino groups of PAMAM.

Rheological measurements (Fig. 5.10) show that storage moduli (*G′*) and loss moduli (*G″*) of GO-PAMAM nanocomposite hydrogels are nearly independent of angular frequency between 0.1–100 rad s^{-1}, confirming the highly elastic characteristic of the hydrogels [181]. Furthermore, *G′* is about one order higher than *G″* and the damping factors (tan δ) are almost independent of frequency, suggesting the formation of stable hydrogels (Fig. 5.10B and 5.11B) [300]. Comprising the least PAMAM concentration of 1 mg mL^{-1}, G10D1H has a storage modulus of 17 kPa at 10 rad s^{-1}. The storage modulus of G10D5H, 42 kPa, is 147% higher than that of G10D1H. A more than 5-fold increase is seen in the storage modulus of G10D10H (108 kPa) compared with that of G10D1H, and more significantly, an about 16-fold increase is found for G10D20H with a storage modulus of 284 kPa. This signifies that up to a certain PAMAM concentration (20 mg mL^{-1}) the hydrogel becomes more elastic with increasing PAMAM content; a higher fraction of PAMAM results in more effective crosslinks which significantly improves the elasticity of the 3D network. However, a further increase of PAMAM content sees a decrease in the storage modulus to 128 kPa for G10D30H, which may owe to its less uniform porous structure compared to G10D20H as discussed previously. Containing 97 wt.% water, G10D20H is still impressive in its mechanical property; the presence of copious crosslinking points on every GO nanosheet and every PAMAM macromolecule (shown in Scheme 5.1), leads to the strong crosslinking interactions. Their storage moduli are comparable to those (Table 1.1) of natural skin and adipose tissues, suggesting that they might be used for relevant tissue engineering apart from drug delivery.

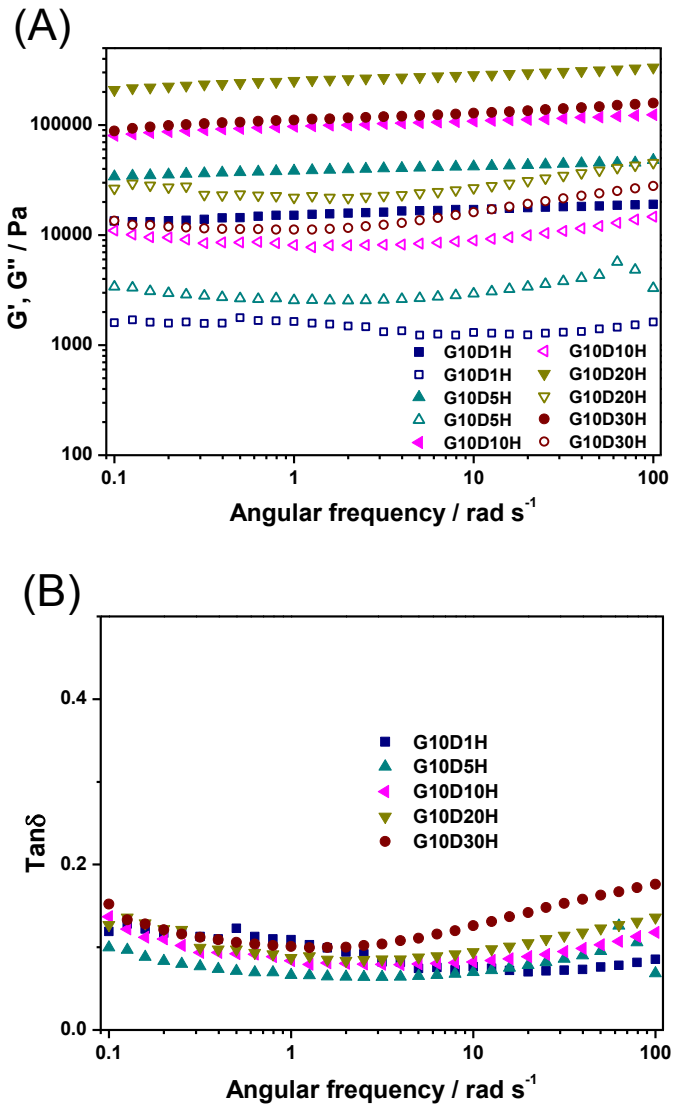

Figure 5.10 (A) *G′* (solid), *G″* (hollow), and (B) tan *δ* of GO-PAMAM hydrogels: G10D1H, G10D5H, G10D10H, G10D20H and G10D30H.

To examine the influence of GO on the viscoelastic parameters, rheological measurements were also undertaken on a series of hydrogels with various GO contents at a fixed concentration of PAMAM (20 mg mL^{-1}). In Fig. 5.11A, the results show a monotonous rise in the storage moduli of the hydrogels with increasing GO content to 10 mg mL^{-1}, being 12, 44 and 284 kPa for G6D20H, G8D20H and G10D20H, respectively. A higher GO content (12 mg mL^{-1}) resulted in an unsuccessful preparation of hydrogel, which was observed during experiments

due to the poor dispersion of GO nanosheets in the mixture (not shown). An increase in the GO content by 67% from G6D20H to G10D20H leads to an enhancement in the storage modulus by 23-fold. In contrast, an increase in the dendrimer content by 19-fold from G10D1H to G10D20H only induces an increase in the storage modulus by 16-fold. It is also noted, by comparing G10D10H, G10D5H with G6D20H, and G10D10H with G8D20H, that while the total content of GO and PAMAM in the hydrogel is lower, the hydrogel composing of a higher GO content exhibits a higher storage modulus. All of these results (Table 5.1) suggest that GO with a higher modulus than PAMAM contributes more significantly to the storage modulus of the nanocomposite hydrogel. Beside the content, the characteristics of GO, *e.g.*, the lateral size and oxidation degree, will also influence the mechanical performance of the nanocomposite hydrogels. For instance, a decrease in the lateral size of GO nanosheets leads to a lower aspect ratio, which makes GO less efficient in reinforcing polymers [301]. It may also impact the dispersion of GO and the crosslinking density at a given GO content, again influencing the mechanical performance of the hydrogel. Similarly, a change to the oxidation degree of GO may affect the dispersion, crosslinking density and the mechanical properties of GO.

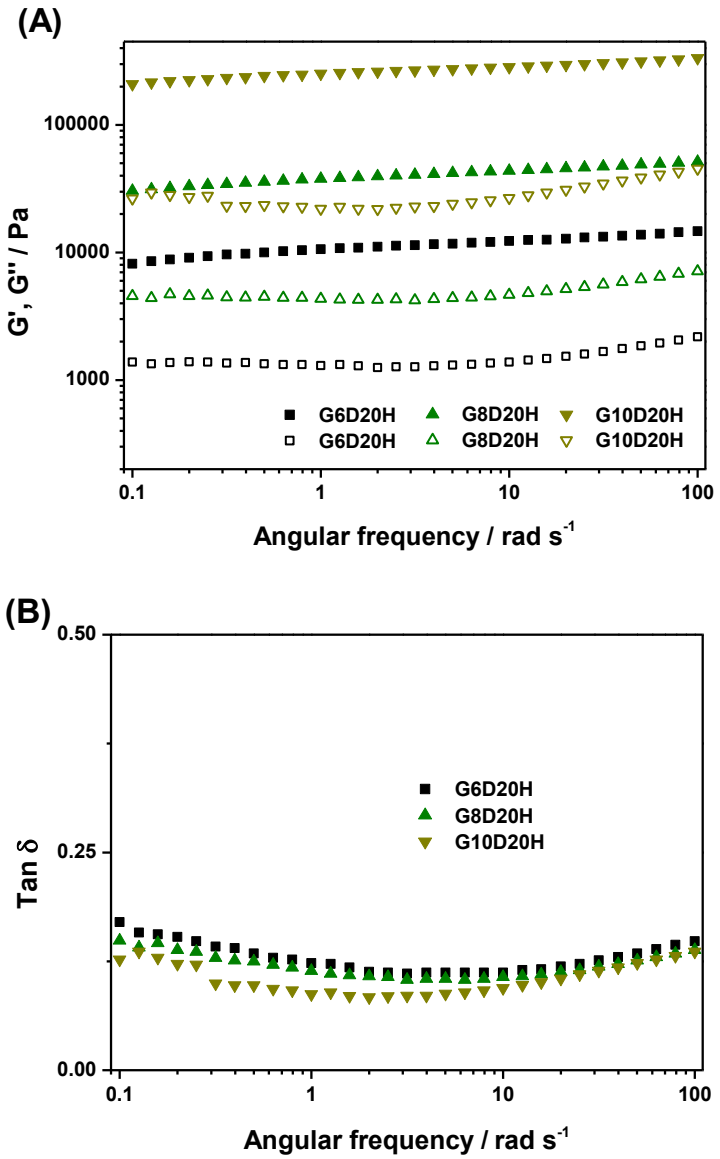

Figure 5.11 (A) *G′* (solid), *G″* (hollow) and (B) tan δ of GO-PAMAM hydrogels: G6D20H, G8D20H and G10D20H.

The highest storage modulus of 284 kPa reported herein for GO-PAMAM nanocomposite hydrogels is 247% of the highest modulus (115 kPa) for self-assembled GO-gelatin nanocomposite hydrogel in Chapter 3, and 165% of the highest value (172 kPa) for the reduced GO-gelatin nanocomposite hydrogels in Chapter 4. The storage moduli of these GO-PAMAM nanocomposite hydrogels are comparable to the values (10–400 kPa) of the GO-chitosan hydrogels reported by

other researchers [224]. Both GO and PAMAM dendrimer possess abundant functional groups which induce multiple strong crosslinks on each GO nanosheet and each PAMAM macromolecule. Furthermore, the inherent high stiffness of GO also contributes to the excellent mechanical properties of these hydrogels.

The crosslinking density (N) and the number average molecular weight of the polymer chains between two neighbouring crosslinks ($\overline{M}_c$) are important parameters of a hydrogel [302]. Assuming GO-PAMAM hydrogels as homogeneous Gaussian networks, these parameters can be calculated from the static shear modulus (G) data according to the rubber elasticity theory (equation 3.1) [251]. Here, the polymer is PAMAM dendrimer instead of gelatin as in Chapter 3 and 4. Thus, M is molecular weight of the PAMAM dendrimer (9,534). By inserting the known data into equations 3.1 and 3.4, N and $\overline{M}_c$ for the hydrogels are determined and shown in Table 5.1.

Table 5.1 Rheological and crosslinking data of GO−PAMAM nanocomposite hydrogels

Sample	PAMAM (mg mL^{-1})	GO (mg mL^{-1})	Storage modulus, G' (kPa)	Crosslinking density, N ($\times 10^{23}$ m^{-3})	Number average molecular weight, $\overline{M}_c$ (g mol^{-1})
G10D1H	1	10	17	26.0	221
G10D5H	5	10	42	64.2	426
G10D10H	10	10	108	165.1	338
G10D20H	20	10	284	434.2	262
G10D30H	30	10	128	195.7	771
G8D20H	20	8	44	67.0	1299
G6D20H	20	6	12	18.8	2703

As shown in Table 5.1, N raises from 26.0 $\times 10^{23}$ m^{-3} for G10D1H to 434.2 $\times 10^{23}$ m^{-3} for G10D20H, having the same varying trend as that for G'. $\overline{M}_c$ values are

calculated to be 221, 426, 338 and 262 g mol^{-1} for G10D1H, G10D5H, G10D10H and G10D20H, respectively. For those hydrogels with a fixed PAMAM content, N enhances from 18.8 × 10^{23} to 67.0 × 10^{23} and 434.2 × 10^{23} m^{-3} for G6D20H, G8D20H and G10D20H, respectively. Correspondingly, $\overline{M}_c$ drops from 2,703 to 1,299 and 262 g mol^{-1}. The results illustrate a structure-property correlation that the hydrogel with a higher modulus possesses a higher crosslinking density, which is consistent with the results in Chapter 3 and Chapter 4.

5.4 Conclusions

GO-PAMAM dendrimer nanocomposite hydrogels with different concentrations of GO and PAMAM were synthesised through self-assembly in one step. The multiple electrostatic interactions between GO sheets and PAMAM molecules, determined by FT-IR and Raman spectroscopy, provided the driving force for network formation.

These strong interactions rendered the nanocomposite hydrogels a high mechanical performance, with a storage modulus of up to 284 kPa at 10 mg mL^{-1} GO and 20 mg mL^{-1} PAMAM. At a fixed GO concentration (10 mg mL^{-1}), the storage modulus improved with PAMAM content first and then dropped under the studied range (up to 30 mg mL^{-1}). The critical concentration for PAMAM to construct a self-assembled GO-PAMAM nanocomposite hydrogel at this GO concentration was approximately 1.0 mg mL^{-1}. In contrast, the modulus of the self-assembled GO-PAMAM hydrogel increased with increasing GO content up to 10 mg mL^{-1} at a fixed PAMAM content of 20 mg mL^{-1}, after which a hydrogel could not be formed. Compared to PAMAM, GO contributed more significantly to the storage modulus of the nanocomposite hydrogel. This kind of GO-PAMAM nanocomposite hydrogels might be explored for the applications in soft tissue engineering and drug delivery.

Chapter 6. Double crosslinked graphene oxide-gelatin hydrogels

6.1 Introduction

We developed chemically crosslinked RGO-gelatin nanocomposite hydrogels in Chapter 4. However, the water content in those hydrogels is very high, which limit their mechanical performance. To develop chemically crosslinked nanocomposite hydrogels with a higher mechanical performance, double crosslinked GO-gelatin nanocomposite hydrogels were synthesised in one pot using glutaraldehyde (GTA) and GTA-grafted GO as double chemical crosslinkers. The resulted nanocomposite hydrogels contain a much lower water content (90 wt.%), compared to those nanocomposite hydrogels studied in Chapter 4. It is hypothesised that GTA firstly reacts with GO sheets to form GTA-grafted GO with one free end of aldehyde group, then the aldehyde groups from GTA-grafted GO and free GTA further react with amino groups in gelatin chains. Thus, chemically crosslinked GO-gelatin nanocomposite hydrogels could be formed through double crosslinking by GTA molecules and GTA modified multifunctional GO sheets. The significant improvements in mechanical properties were assumed to be down to the novel structure of double crosslinked network and the much lowered water content. FT-IR, SEM, rheometry and the compression tests were performed to characterise the nanocomposite hydrogels. The chemical structure, morphology, gelation mechanisms and mechanical properties of the hydrogels were investigated in depth. Swelling tests were implemented to determine their swelling capabilities.

6.2 Experimental section

6.2.1 Materials

Gelatin, graphite powder and the other chemicals used for GO preparation were the same as described in Chapter 3. Glutaraldehyde (50%) and glycine (1 mol L^{-1}) were all obtained from Sigma-Aldrich Corporation.

6.2.2 Preparation of GO-gelatin hydrogels

GO was synthesised from pristine graphite by a modified Hummers' method [155], and purified and freeze-dried as described in Chapter 3. The GO-gelatin nanocomposite hydrogels were synthesised by crosslinking gelatin using GTA in the presence of GO nanosheets. A typical synthesis of the GO-gelatin nanocomposite hydrogel is described as follows. 0.1 mL of aqueous GTA (0.056 g, 0.56 mg mL^{-1}) solution was mixed with 4.9 mL of aqueous GO (0.001 g, 0.2 mg mL^{-1}) suspension under vigorous stirring at 37 ℃ for 1 h. 0.999 g gelatin was added into 5 mL distilled water and then stirred at 60 ℃ for 1 h. It was then added into the water mixture of GTA and GO under stirring for 3 min before it was cast into a cylindrical mould. The mixture was kept at 20 ℃ for 24 h to complete the gelation of gelatin through chemical crosslinking. In these hydrogels, the concentration of GO increased from zero to 5 mg mL^{-1}, while the weight ratio of both gelatin and GO to water was kept constant at 1:10. After gelation, the remaining aldehyde groups from GTA were blocked by immersing the bulk hydrogel into a glycine solution (100 mM) at 37 ℃ for 1 h, and following triple wash in distilled water. The hydrogels were named as GH*n*, in which *n* denoted ten times of the concentration (mg mL^{-1}) of GO in the final hydrogel.

6.2.3 Structure characterisation

Gelatin, GO and double crosslinked GO-gelatin nanocomposite hydrogels were analysed by FT-IR using the same instrument and specimens preparing method as described in Chapter 3. As a control sample to study the interactions between GO and GTA, the GTA-modified GO was also investigated by FT-IR. This sample was prepared using the same procedure as for nanocomposite hydrogel, namely mixing the same amount of GO suspension and GTA solution at 37 ℃ for 1 h, and subsequently followed by dialysis for 3 days to remove the unreacted GTA and then air-dry at room temperature for 3 days. A neat GO suspension was also air-dried and characterised as a control. Morphologies of the GO-gelatin hydrogels were studied by using SEM (the same as in Chapter 3). The average pore sizes were calculated (at least 100 pores) by using ImageJ software.

6.2.4 Compression tests

Uniaxial compression testing was performed using a mechanical testing system (Model TA500, Lloyd Instruments) equipped with a control and analysis software of NEXYGEN. The hydrogel rods (20 mm high and 10 mm in diameter) were compressed at a speed rate of 1 mm min^{-1} using a load cell of 50 N. Measurement was performed on 5 replicate samples in each group.

6.2.5 Rheological measurements

The rheological properties of the double crosslinked GO-gelatin nanocomposite hydrogels were measured by using the same instrument and method used in Chapter 5.

6.2.6 Swelling tests

Hydrogel discs ($10 \times 10 \times 2$ mm^3) were air-dried for one week at room temperature and then submerged in distilled water at 23 ± 1 ℃ for swelling tests. The samples were weighed after a week when the weights became constant. Three replicate samples were used for the measurements. The swelling ratios of these hydrogels were determined using equation 6.1:

$$SR = \frac{W_s - W_d}{W_d} \tag{6.1}$$

in which W_s and W_d denote the weights of the swollen and dried hydrogel, respectively.

6.3 Results and discussion

GO nanosheets used to synthesise the nanocomposite hydrogels have been characterised by AFM and laser sizing in Chapter 3. The thickness of single-layer GO nanosheets was determined in Chapter 5 to be 1.0 nm and the majority of GO nanosheets ranged in size from 2.2 to 20 μm with a mean of 5.5 μm. When a GO aqueous suspension was utilised for the preparation of GO reinforced hydrogels, the functional groups on the GO nanosheets provided sites for physical and chemical interactions with the polymer matrix [303,304].

As described before [271,305], the spectrum of GO (curve a in Fig. 6.1) shows the existence of different oxygen-containing functional groups: carbonyl groups (C=O, 1729 cm^{-1}), alkoxy groups (C–O, 1044 cm^{-1}) and epoxy groups (C–O–C, 1222 cm^{-1}). O–H stretching bond and C=C vibrations are also observed at 3200–3400 cm^{-1} and 1616 cm^{-1}, respectively. Gelatin is characterised for comparison, and its main characteristic groups are identified in curve h. The absorption bands at 1633,

1522, 1230 and 3285 cm^{-1} are assigned to the amide I vibration (C=O), amide II bending vibration (N–H), amide III and N–H stretching, respectively [236,306]. GH0 has a similar profile to gelatin powder. After incorporation of GO into the gelatin, the C=O peak in GO at 1729 cm^{-1} disappears in the GO-gelatin nanocomposite (curve b-g), which is ascribed to the association between carboxyl groups on GO nanosheets and amino functional groups in gelatin to form ammonium carboxylate complex [239]. The features of the amide I vibration and amide II bending vibration from gelatin dominate in the studied nanocomposites (curves b-g), overshadowing the feature of C=C vibrations from GO.

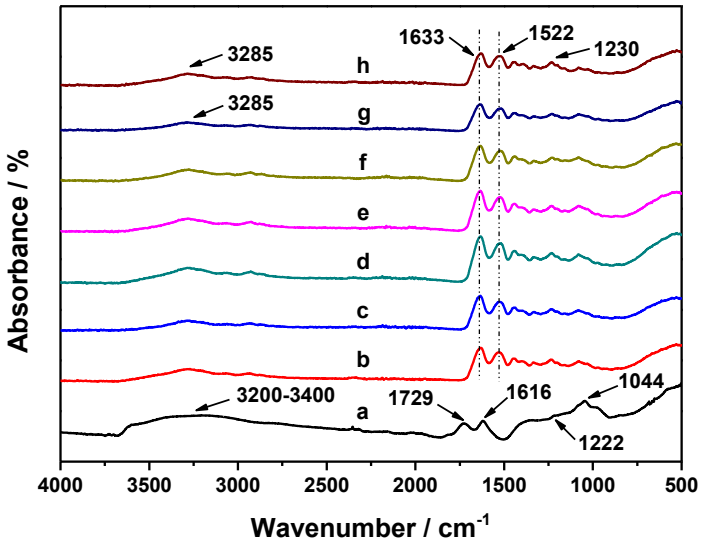

Figure 6.1 FT-IR spectra of the lyophilised (a) GO, (b) GH0, (c) GH1, (d) GH5, (e) GH10, (f) GH30, (g) GH50, and (h) neat gelatin.

To investigate the formation mechanism of the hydrogels further, the FT-IR spectrum of the mixture of GO and GTA, prior to mixing with gelatin solution to form a hydrogel, was also studied. Fig. 6.2 shows the spectra comparison of GO and GTA modified GO. The occurrence of a new shoulder at 2792–2840 cm^{-1}, corresponding to the C–H stretch mode of GTA, initially indicates the presence of

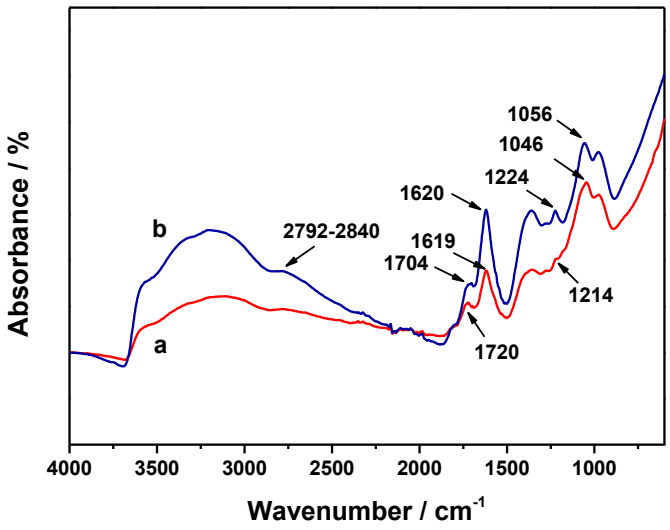

Figure 6.2 FT-IR spectra comparison of (a) GO and (b) GTA surface-modified GO.

GTA on GO sheets. The peaks of C–O and C–O–C show some shifts from 1046 and 1214 to 1056 cm^{-1} and 1224 cm^{-1} respectively, along with significant increases of their intensities, suggesting the formation of hemiacetal structure by reacting the hydroxyl groups of GO sheets with aldehyde groups of GTA [307]. The C=O peak at 1720 cm^{-1} shifts to 1704 cm^{-1} and its intensity increases, which is ascribed to the residual unreacted aldehyde groups of GTA as its one end may still remain free while the other end reacts with GO. These findings are in line with those reported in the literature [307], confirming the reaction between the hydroxyl groups of GO and the aldehyde groups of GTA and their covalent bonding. The proposed chemical reaction is illustrated in Scheme 6.1. The remaining aldehyde groups on the GTA modified GO act as multiple crosslinker points for further reaction with gelatin chains during hydrogel gelation. It is known that the aldehyde groups of GTA react with amino groups in gelatin to yield Schiff bases [308] and crosslink gelatin molecular chains to create a network. Additional crosslinking was also reported *via* the chemical reaction between aldehyde groups of GTA and hydroxyl functional groups of gelatin [308]. Thus, the GO-gelatin nanocomposite hydrogels are formed

through double crosslinking by GTA molecules and GTA modified multifunctional GO sheets, and possibly also with additional physical interactions, including electrostatic interaction and hydrogen bonding, enduring between the carboxyl, epoxy and unreacted hydroxyl functional groups on GO nanosheets and amino groups in gelatin molecules. The mechanism of the formation of double crosslinked structure in the GO-gelatin nanocomposite hydrogel is proposed in Scheme 6.2.

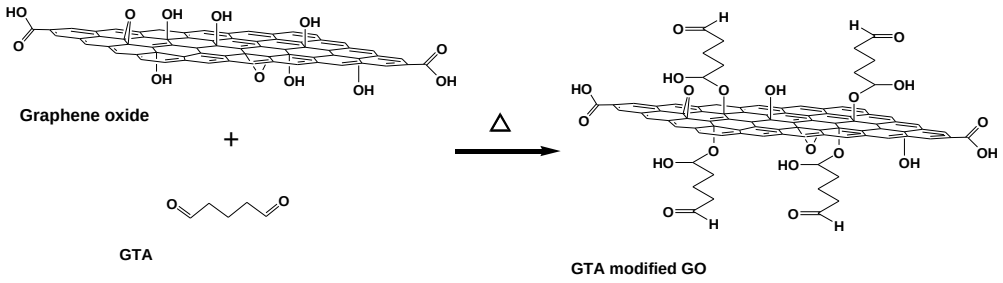

Scheme 6.1 The proposed chemical reaction between GO and GTA.

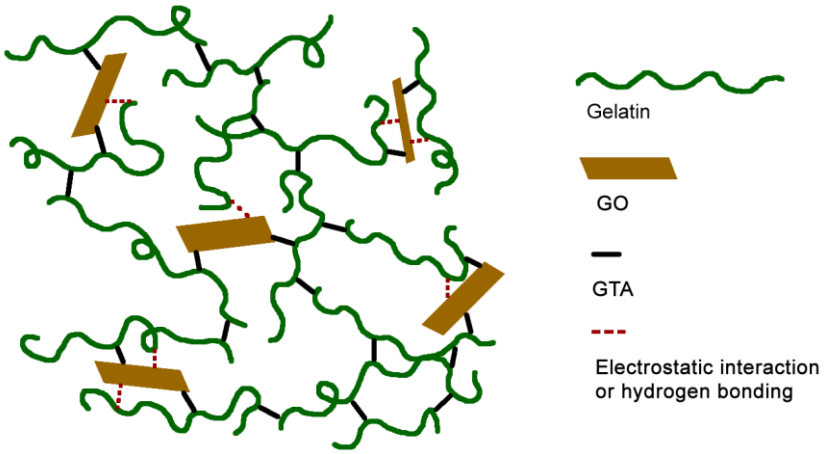

Scheme 6.2 The proposed schematic structure of double crosslinked GO-gelatin nanocomposite hydrogels. Here, double crosslinkers refer to GTA and GTA-modified GO. As the physical interactions are weaker than the two chemical crosslinks, they are not considered in the term of double crosslinks.

The interior morphologies of the double crosslinked GO-gelatin nanocomposite hydrogels were investigated by SEM. The neat gelatin hydrogel crosslinked by GTA, GH0, displayed a porous structure with a pore size of 1.67 ± 0.38 μm (Fig. 6.3A). After incorporation of GO, the GO-gelatin hydrogel is double crosslinked by both GTA and GTA-grafted GO and becomes stiffer, which suppresses the growth of ice crystals during the freezing step. This resulted in a smaller pore size for GO-gelatin hydrogel GH1 (0.74 ± 0.29 μm) with a narrow pore size distribution (Fig. 6.3B), suggesting good distribution of GO sheets within the hydrogel at the low concentration. With increasing GO content, the pores become uneven and shallower (Figs. 6.3C-F). A wider distribution of pore sizes suggests GO is not distributed in localised areas of the hydrogel network as well as in GH1. GH5, GH10, GH30 and GH50 have bigger average pore sizes of 0.89 ± 0.35 μm, 1.21 ± 0.42 μm, 1.38 ± 0.66 μm and 1.27 ± 0.44 μm, respectively.

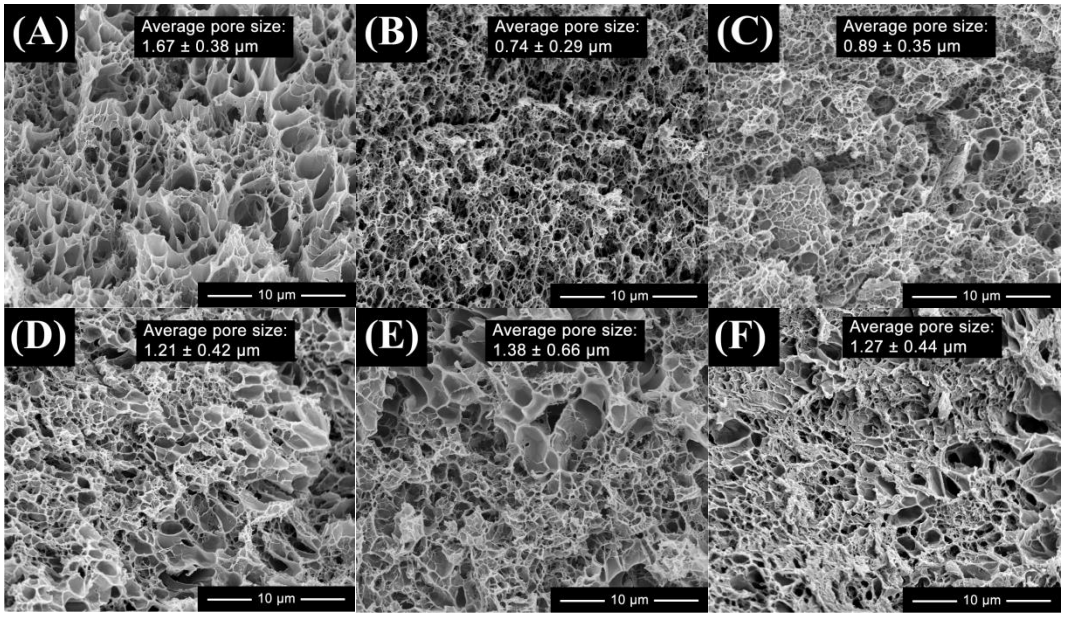

Figure 6.3 SEM images of lyophilised GO-gelatin nanocomposite hydrogels: (a) GH0, (b) GH1, (c) GH5, (d) GH10, (e) GH30 and (f) GH50.

Mechanical properties of the double crosslinked GO-gelatin hydrogels were evaluated by uniaxial compression. The compressive strength of the hydrogel increases upon the increase of the GO concentration (Fig. 6.4). The compressive strength of 566 kPa for GH50 with the highest GO concentration shows a 288% increase compared to 146 kPa for the neat gelatin hydrogel (Table 6.1). These values are comparable to those values (91–501 kPa) of gelatin methacrylate-GO composite hydrogels [192]. The compressive modulus of the GO-gelatin nanocomposite hydrogel increases in general upon the incorporation of GO into the hydrogel. It records the maximum modulus of 62 kPa for GH30 which almost triples the value (21 kPa) of the neat gelatin hydrogel (Table 6.1). These significant improvements in the mechanical performance of the gelatin hydrogel are ascribed to the double crosslinked network structure in the nanocomposite hydrogels in which GO sheets, grafted with GTA, function as multifunctional crosslinkers, and also to the reinforcement effect of GO as an effective nanofiller with a superb fracture strength, a Young's modulus beyond 208 GPa [40], a large surface area and a high aspect ratio. Furthermore, carboxyl, epoxy and unreacted hydroxyl groups on the GO nanosheets are well associated with the polar gelatin by electrostatic interaction and hydrogen bonding [238], also providing effective load transfer between gelatin matrix and GO nanosheets along with the covalent bonds. The compressive fracture energies (the areas under the compressive stress-strain curves) of the nanocomposite hydrogels are also calculated and shown in Table 6.1, increasing from 20.8 kJ m^{-3} for GH0 to 76.3 kJ m^{-3} for GH50. The high flexibility and mobility of GO nanosheets can help effectively dissipate energy that is applied to the hydrogel, and therefore has a prominent effect on the hydrogel toughness [309,310].

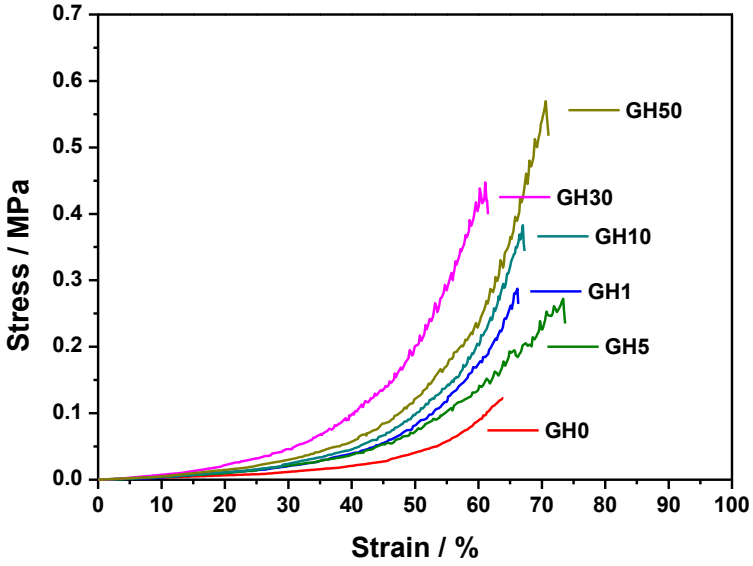

Figure 6.4 Compressive stress-strain curves of hydrogels: GH0, GH1, GH5, GH10, GH30 and GH50.

The compressive tangent moduli of the hydrogels significantly varied upon the change of strain magnitude, indicating nonlinear and viscoelastic material behaviour (Fig. 6.5). The tangent moduli of all GO-gelatin hydrogels are higher than those of the neat gelatin hydrogel at strain magnitudes greater than 10%. The tangent modulus of GH30 is higher than that of GH50 at strain magnitudes greater than 10%, in line with their compressive moduli. This may be due to the worse distribution of GO sheets in GH50. The content of GO sheets has two opposing effects on modulus: on one side, a higher GO concentration increases the modulus of the hydrogel; but on the other side, it causes worse distribution which leads to aggregation of some GO sheets and so overall reduces the crosslinking density and the modulus. In contrast, the compressive strains at break of GO-gelatin hydrogels are all similar except for GH5. Overall, the compressive strength, stiffness and toughness of the gelatin hydrogel are improved by the GO effect, which plays a critical part in enhancing their mechanical properties.

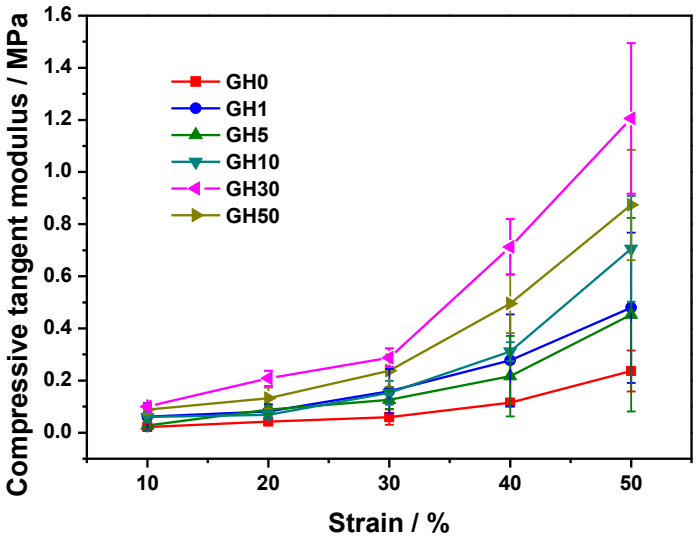

Figure 6.5 Compressive tangent modulus versus compressive strain of hydrogels: GH0, GH1, GH5, GH10, GH30 and GH50. Error bar indicate standard deviation on five replicate samples.

Table 6.1 Compressive properties of the double crosslinked GO-gelatin nanocomposite hydrogels.

Sample	Compressive strength (kPa)	Young's modulus (kPa)	Fracture strain (%)	Fracture energy (kJ m^{-3})
GH0	146 ±11	21 ±10	67.9 ±4.4	20.8 ±14.9
GH1	286 ±25	31 ±12	67.5 ±11.4	37.3 ±4.4
GH5	253 ±55	31 ±14	77.0 ±4.4	40.9 ±6.0
GH10	377 ±68	42 ±9	70.2 ±2.4	49.7 ±6.7
GH30	509 ±118	62 ±18	65.9 ±5.0	74.2 ±20.7
GH50	566 ±56	58 ±11	70.0 ±2.5	76.3 ±4.7

Rheological measurements (Fig. 6.6) reveal viscoelastic characteristics of the hydrogels. Their storage moduli are always greater than their counterpart loss moduli, indicating elastic behaviour is dominant in these hydrogels [181]. In Fig. 6.6A, G' is about one to two magnitude orders higher than its corresponding G'' (Fig. 6.6B). So, the values of the damping factor, tan δ, are much lower than 1, suggesting the formation of highly elastic hydrogels (Fig. 6.6C) [300]. The storage modulus of the

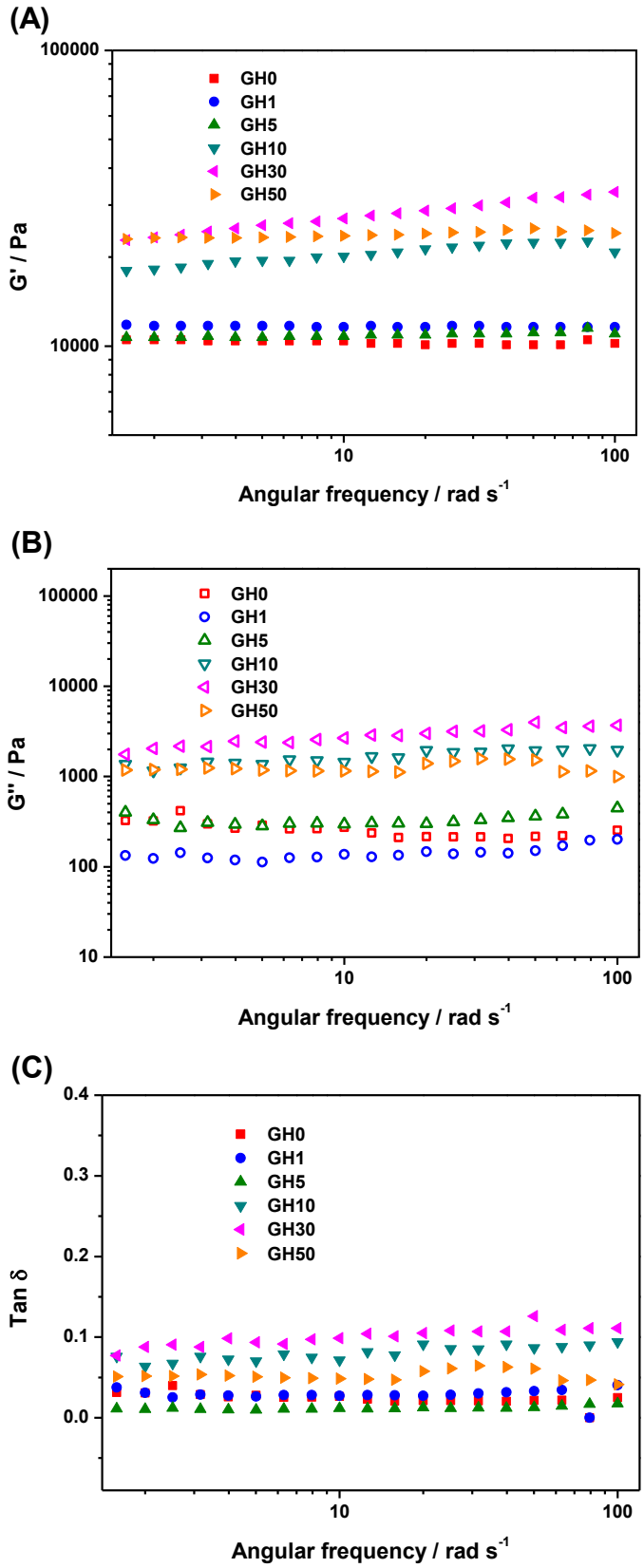

Figure 6.6 (A) *G′* (solid), (B) *G″* (hollow) and (C) damping factor (tan *δ*) of hydrogels: GH0, GH1, GH5, GH10, GH30 and GH50.

neat gelatin hydrogel (GH0) is 10.4 kPa (at 10 rad s^{-1}). With the incorporation of GO into the gelatin hydrogels, their storage modulus increases. A 12% increase has been observed in the hydrogel GH1 (11.6 kPa), compared to that of GH0. The storage modulus of GH10 (20.1 kPa) increases more significantly, showing 93% increase in contrast to GH0. The storage modulus reaches the highest value of 27.0 kPa (at 10 rad s^{-1}) for GH30 which shows a 160% increase, though it is lower than that of GH50 below the crossover point at 2 rad s^{-1}. A further increase in the concentration of GO leads to a decrease in the storage modulus to 23.6 kPa (at 10 rad s^{-1}) for GH50, indicating the structure weakening, which may be owing to the aggregation of GO and a lower crosslinking density as previously discussed. The strong mechanical properties of these nanocomposite hydrogels provide them possibility to be used in a broad biomedical area, such as artificial skin, wound dressing and etc., referencing to mechanical properties of some natural tissues (Table 1.1).

The crosslinking density (*N*) of the hydrogels, an important parameter to characterise the structure-property relationship of hydrogels, was investigated. It is useful for the design of the new hydrogels and manipulation of their properties. The double crosslinked GO-gelatin nanocomposite hydrogel is considered as a Gaussian network and *N* is related to the static shear modulus (*G*) [251]. The correlation between them was depicted by the rubber elasticity theory, as shown in equation 3.1 [251]. $\overline{M}_c$ is the average molecular weight of polymer chain segments between the crosslinking sites, and $\overline{M}$ is the molecular weight of the polymer (gelatin). By substituting the experimental data of *G'* in equations 3.1 and 3.4, the crosslinking density and $\overline{M}_c$ are determined and shown in Table 6.2.

The crosslinking density, *N*, of the hydrogels increases upon the increase in the GO concentration, from 15.9 $\times 10^{23}$ m^{-3} for GH0 up to 41.3 $\times 10^{23}$ m^{-3} for GH30 before dropping to 36.1 $\times 10^{23}$ m^{-3} for GH50. The hydrogel with a higher modulus

Table 6.2 *N* and $\overline{M}_c$ in the double crosslinked GO-gelatin nanocomposite hydrogels with different compositions.

Sample	Gelatin (wt.%)	GO (mg mL^{-1})	GTA (g)	G' (kPa)	*N* ($\times 10^{23}$ m^{-3})	$\overline{M}_c$ (g mol^{-1})
GH0	10	0	0.056	10.4	15.9	15057
GH1	10	0.1	0.056	11.6	17.7	14396
GH5	10	0.5	0.056	10.8	16.5	14830
GH10	10	1	0.056	20.1	30.7	10983
GH30	10	3	0.056	27.0	41.3	9210
GH50	10	5	0.056	23.6	36.1	10006

possesses a higher crosslinking density, which is consistent with the literature [311]. Considering the same amount of chemical crosslinker (GTA) was used in the synthesis of hydrogels, it is GO that induces the higher crosslinking density; it acts as both a multifunctional crosslinker, when grafted with multiple GTA, and a reinforcing nanofiller. Like the case with compressive or storage modulus, the decrease of *N* for GH50, which has the highest GO content, can be explained by less effective crosslinks between GO nanosheets and gelatin molecules due to increased aggregation of GO sheets. The values of $\overline{M}_c$ obtained vary in reverse to the crosslinking density, decreasing from 15,057 to 9,210 g mol^{-1} for GH0 and GH30 respectively before increasing to 10,006 g mol^{-1} for GH50.

To better understand the GO effect on the crosslinking of the networks, the swelling property of the lyophilised GO-gelatin nanocomposite hydrogels with

different GO contents was investigated, and illustrated in Fig. 6.7. The swelling reached equilibrium in distilled water after a week. All the hydrogels basically maintained their original shape, and there was no migration of GO nanosheets from the hydrogel into water throughout the swelling tests. With the increase of the amount of GO, the swelling ratio of GO-gelatin nanocomposite generally decreases. The equilibrium swelling ratio decreases from 8.3 g g^{-1} for GH0 to 7.4 g g^{-1} for GH50. This confirms a higher crosslink degree in the nanocomposite hydrogel. More specially, GO sheets, grafted with multiple GTA, can function as multifunctional crosslinking agents to form multiple junctions in the network and inhibit their swelling, resulting in the decrease in swelling capability. Similar phenomena have been reported for different nanofiller-enhanced hydrogels in the literature [171,312]. However, the swelling ratio (7.4 g g^{-1}) of GH50 is higher than that (7.0 g g^{-1}) of GH30 presumably due to increased aggregation of GO sheets. It is well known that there is a strong correlation between the swelling capability and the crosslink density. Thus, the crosslinking density of GH50 is lower than that of GH30. The results are in line with the corresponding crosslinking densities derived from mechanical properties and presented in the Table 6.2.

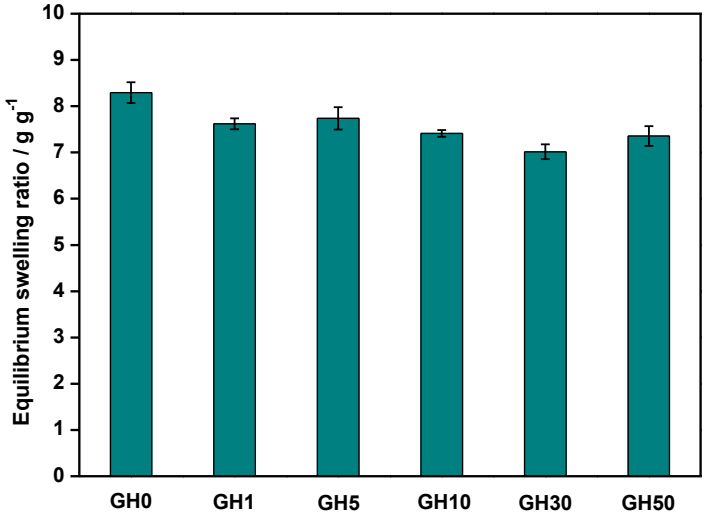

Figure 6.7 Equilibrium swelling of the double crosslinked GO-gelatin nanocomposite hydrogels with various GO contents: GH0, GH1, GH5, GH10, GH30 and GH50. Error bar indicate standard deviation on three replicate samples.

6.4 Conclusions

Double crosslinked GO-gelatin nanocomposite hydrogels have been successfully synthesised by using both GTA and GTA modified GO sheets as crosslinking agents. The hydrogels with varying amounts of GO display improved mechanical strength, stiffness and toughness, which is ascribed to the double crosslinked network structure and also the contribution of GO sheets as multifunctional crosslinkers and effective reinforcing nanofillers. At a fixed GTA concentration, the compressive strength of the hydrogel increases with increasing GO content. GH50, containing 5 mg mL^{-1} GO, shows the highest compressive strength of 566 kPa at a strain of 70%, exhibiting a 288% increase compared to the neat gelatin hydrogel. However, the highest elastic modulus of 62 kPa is observed for GH30 with 3 mg mL^{-1} GO, which has a compressive strength of 509 kPa at a strain of 65.9%. The elastic modulus value of GH30 doubles that of the neat gelatin hydrogel. The shear storage modulus generally increases with increasing GO content, apart from the highest GO content.

The highest value of shear storage modulus is 27.0 kPa for GH30, showing a 160% increase to 10.4 kPa for GH0. The swelling capability of the GO-gelatin hydrogel decreases with increasing crosslink degree and mechanical strength. The novel nanocomposite hydrogels could have the potential in the applications for biomedical engineering.

Chapter 7. Overall conclusions and suggestions for future work

7.1 Overall conclusions

This thesis has focused on the synthesis and characterisation of novel graphene-based polymer nanocomposite hydrogels with strong mechanical properties, using GO and a biocompatible cationic polymer (*i.e.*, gelatin and PAMAM dendrimer) as the raw materials. The four types of nanocomposite hydrogels were developed by different methods and were studied individually in depth, though some common characterisation techniques were used throughout the thesis. GO (or RGO) acted as both an effective multifunctional crosslinking agent and a strong reinforcing agent of the nanocomposite hydrogels. The mechanical properties of the hydrogel increased with increasing GO or polymer concentration and GO provided a higher contribution than the polymer at a comparable concentration.

Both physically crosslinked GO-gelatin nanocomposite hydrogels and GO-PAMAM dendrimer nanocomposite hydrogels were synthesised based on self-assembly utilising mainly electrostatic interactions. This technique was facile and green, avoiding involving an organic crosslinker, and thus benefited the high biocompatibility. The multiple crosslinking sites on each GO nanosheet and gelatin chain rendered the physically crosslinked GO-gelatin hydrogels a high mechanical performance. These hydrogels were pH-sensitive and exhibited pH-controlled drug release behaviour. PAMAM dendrimer could possess a higher charge density on its globular surface when it was protonated, leading to stronger electrostatic interactions with opposite charged GO nanosheets. The optimal charge capacity ratios of GO to PAMAM in the hydrogels resulted in the formation of a robust hydrogel. The highest

storage modulus of GO-PAMAM nanocomposite hydrogels was 2.5 times of that for physically crosslinked GO-gelatin nanocomposite hydrogel. These GO-PAMAM nanocomposite hydrogels demonstrated self-healing capability, due to their strong and reversible physical crosslinks, *i.e.*, electrostatic interactions.

RGO-gelatin nanocomposite hydrogels were further synthesised from physically crosslinked GO-gelatin nanocomposite hydrogels through reaction between GO sheets and gelatin molecules, where gelatin molecules reduced GO to RGO. The gelation forces included both chemical (mainly) and physical crosslinking between graphene sheets and gelatin chains. The highest storage modulus of RGO-gelatin hydrogels was 50% higher than the value of physical crosslinked GO-gelatin nanocomposite hydrogels. The degradation tests showed that the hydrogels were enzyme favourable.

The double crosslinked GO-gelatin nanocomposite hydrogels were developed containing a much lower water content compared to the hydrogels studied in Chapter 3, 4, and 5. These nanocomposite hydrogels exhibited significant increases in mechanical properties compared to the neat gelatin hydrogel, which was ascribed to the double crosslinked structure and also the contribution of GO sheets as multifunctional crosslinkers and effective reinforcing nanofillers. The swelling capability of GO-gelatin hydrogel decreased with increasing the crosslink degree, while their mechanical properties increase.

The mechanical properties of RGO-gelatin nanocomposite hydrogels, GO-PAMAM nanocomposite hydrogels and double crosslinked GO-gelatin nanocomposite hydrogels are comparable or higher than that of some natural tissue, such as skin and adipose tissue as shown in Table 1.1. Thanks to the improvements in the mechanical properties, pH sensitivity and self-healing property, these novel

nanocomposite hydrogels could have potential for drug delivery and tissue engineering. Their mechanical properties are shown in Table 7.1, and their potential applications are also suggested.

Table 7.1 Mechanical properties of the prepared different hydrogels and their potential applications.

Prepared hydrogels	Maximum Storage modulus (kPa)	Maximum Compressive strength (kPa)	Maximum Young's modulus (kPa)	Potential applications
GO-gelatin nanocomposite hydrogels	114.5	-	-	Drug delivery
RGO-gelatin nanocomposite hydrogels	172.3	-	-	Drug delivery, adipose tissue
GO-PAMAM nanocomposite hydrogels	284.0	-	-	Drug delivery, skin
Double crosslinked GO-gelatin nanocomposite hydrogels	27.0	566 ±56	62 ±18	skin, wound dressing, etc.

7.2 Suggestions for future work

GO with the same average size was used in the preparation of the nanocomposite hydrogels throughout this project. As we know, the size of the reinforcement filler is a key influential factor to the mechanical properties of composites. Hence, the effect of GO particle size on mechanical properties of the nanocomposite hydrogels could be studied to optimise the size of GO in the synthesis of the hydrogels.

Increasing the electrical field density on the GO sheet surface by modification or functionalisation is another possible method to enhance the mechanical performance of the physically crosslinked nanocomposite hydrogels, *i.e.*, GO-gelatin nanocomposite hydrogels and GO-PAMAM nanocomposite hydrogels. The increased electrical field density could strengthen the electrostatic interactions

between negatively charged GO sheets and positively charged gelatin or PAMAM dendrimer macromolecules. Therefore, the mechanically improved hydrogels could be obtained.

Another strategy to improve the mechanical performance is to increase the solid content per unit volume in the hydrogels, *i.e.*, the concentration of GO (or RGO) and the polymer (gelatin or PAMAM dendrimer). Considering the solid content is still low, further increasing their proportion to the whole hydrogel could benefit their mechanical strength, particularly for GO-gelatin nanocomposite hydrogels, RGO-gelatin nanocomposite hydrogels and GO-PAMAM nanocomposite hydrogels. The morphology studies in this research suggest that beyond the optimal GO or the polymer concentration the inhomogeneity of the microstructure of the nanocomposite hydrogel increases, which leads to the decline in the mechanical properties. The inhomogeneity of the microstructure may be owing to the quick gelation of the nanocomposite developed, which restricts the uniform distribution of GO sheets in the gelatin matrix. The possible solution could be to tune pH value of the starting solutions prior to mixing to supress the electrostatic interaction between the two components and slow down the gelation process, and then reverse the pH value afterwards.

To improve the double crosslinked GO-gelatin hydrogels, this might be through introducing a second polymer network into the existing hydrogel to form an interpenetrating structure, like DN hydrogels. Interpenetrating network is a reasonable strategy to improve the mechanical performance of the hydrogels. By controlling the proportion of the initiator, crosslinker and monomer, the polymerised chains of the second polymer could be long and flexible, which can enhance the entanglement effect in the hydrogel.

Bibliography

[1] X. Yang, L. Qiu, C. Cheng, Y. Wu, Z.-F. Ma, D. Li, Ordered gelation of chemically converted graphene for next-generation electroconductive hydrogel films, Angew. Chem. Int. Ed. 50 (2011) 7325-7328.

[2] K. Haraguchi, Nanocomposite hydrogels, Curr. Opin. Solid State Mater. Sci. 11 (2007) 47-54.

[3] A.S. Hoffman, Hydrogels for biomedical applications, Adv. Drug Delivery Rev. 54 (2002) 3-12.

[4] L. Klouda, A.G. Mikos, Thermoresponsive hydrogels in biomedical applications, Eur. J. Pharm. Biopharm. 68 (2008) 34-45.

[5] A.K. Gaharwar, N.A. Peppas, A. Khademhosseini, Nanocomposite hydrogels for biomedical applications, Biotechnol. Bioeng. 111 (2014) 441-453.

[6] S. Van Vlierberghe, P. Dubruel, E. Schacht, Biopolymer-based hydrogels as scaffolds for tissue engineering applications: A review, Biomacromolecules 12 (2011) 1387-1408.

[7] K.Y. Lee, D.J. Mooney, Hydrogels for tissue engineering, Chem. Rev. 101 (2001) 1869-1880.

[8] J.L. Drury, D.J. Mooney, Hydrogels for tissue engineering: Scaffold design variables and applications, Biomaterials 24 (2003) 4337-4351.

[9] M. Goldberg, R. Langer, X. Jia, Nanostructured materials for applications in drug delivery and tissue engineering, J. Biomater. Sci. Polym. Ed. 18 (2007) 241-268.

[10] M. Hamidi, A. Azadi, P. Rafiei, Hydrogel nanoparticles in drug delivery, Adv. Drug Delivery Rev. 60 (2008) 1638-1649.

[11] N.A. Peppas, J.Z. Hilt, A. Khademhosseini, R. Langer, Hydrogels in biology and medicine: From molecular principles to bionanotechnology, Adv. Mater. 18 (2006) 1345.

[12] B. Singh, L. Pal, Sterculia crosslinked PVA and PVA-poly(AAm) hydrogel wound dressings for slow drug delivery: Mechanical, mucoadhesive, biocompatible and permeability properties, J. Mech. Behav. Biomed. Mater. 9 (2012) 9-21.

[13] K. Laenge, B.E. Rapp, M. Rapp, Surface acoustic wave biosensors: A review, Anal. Bioanal. Chem. 391 (2008) 1509-1519.

[14] S. Burrs, D. Vanegas, M. Bhargava, N. Mechulan, P. Hendershot, H. Yamaguchi, C. Gomes, E. Mclamore, A comparative study of graphene–

hydrogel hybrid bionanocomposites for biosensing, Analyst 140 (2015) 1466-1476.

[15] A. Kerin, M. Wisnom, M. Adams, The compressive strength of articular cartilage, Proc. Inst. Mech. Eng. H 212 (1998) 273-280.

[16] T.A. Wren, S.A. Yerby, G.S. Beaupré, D.R. Carter, Mechanical properties of the human achilles tendon, Clin. Biomech. 16 (2001) 245-251.

[17] A. Race, A.A. Amis, The mechanical properties of the two bundles of the human posterior cruciate ligament, J. Biomech. 27 (1994) 13-24.

[18] I.S. Nash, P.R. Greene, C.S. Foster, Comparison of mechanical properties of keratoconus and normal corneas, Exp. Eye Res. 35 (1982) 413-424.

[19] J.Ø. Hjortdal, Regional elastic performance of the human cornea, J. Biomech. 29 (1996) 931-942.

[20] A.R. Gordon, M.J. Siegman, Mechanical properties of smooth muscle. I. Length-tension and force-velocity relations, Am. J. Physiol. 221 (1971) 1243-1249.

[21] P.B. Dobrin, A.A. Rovick, Influence of vascular smooth muscle on contractile mechanics and elasticity of arteries, Am. J. Physiol. 217 (1969) 1644-1651.

[22] P. Agache, C. Monneur, J. Leveque, J. De Rigal, Mechanical properties and young's modulus of human skin in vivo, Arch. Dermatol. Res. 269 (1980) 221-232.

[23] B. Holt, A. Tripathi, J. Morgan, Viscoelastic response of human skin to low magnitude physiologically relevant shear, J. Biomech. 41 (2008) 2689-2695.

[24] A. Gefen, E. Haberman, Viscoelastic properties of ovine adipose tissue covering the gluteus muscles, J. Biomech. Eng. 129 (2007) 924-930.

[25] M. Geerligs, G.W. Peters, P.A. Ackermans, C.W. Oomens, F. Baaijens, Linear viscoelastic behavior of subcutaneous adipose tissue, Biorheology 45 (2008) 677-688.

[26] S. Naficy, H.R. Brown, J.M. Razal, G.M. Spinks, P.G. Whitten, Progress toward robust polymer hydrogels, Aust. J. Chem. 64 (2011) 1007-1025.

[27] A.M. Costa, J.F. Mano, Extremely strong and tough hydrogels as prospective candidates for tissue repair–A review, Eur. Polym. J. 72 (2015) 344-364.

[28] B. Rybtchinski, Adaptive supramolecular nanomaterials based on strong noncovalent interactions, ACS Nano 5 (2011) 6791-6818.

[29] H. Zhang, H. Xia, Y. Zhao, Poly(vinyl alcohol) hydrogel can autonomously self-heal, ACS Macro Lett. 1 (2012) 1233-1236.

[30] K. Haraguchi, T. Takehisa, Nanocomposite hydrogels: A unique organic-inorganic network structure with extraordinary mechanical, optical, and swelling/de-swelling properties, Adv. Mater. 14 (2002) 1120-1124.

[31] K. Haraguchi, Synthesis and properties of soft nanocomposite materials with novel organic/inorganic network structures, Polym. J. 43 (2011) 223-241.

[32] Q. Wang, J.L. Mynar, M. Yoshida, E. Lee, M. Lee, K. Okuro, K. Kinbara, T. Aida, High-water-content mouldable hydrogels by mixing clay and a dendritic molecular binder, Nature 463 (2010) 339-343.

[33] Y. Liu, M.F. Zhu, X.L. Liu, W. Zhang, B. Sun, Y.M. Chen, H.J.P. Adler, High clay content nanocomposite hydrogels with surprising mechanical strength and interesting deswelling kinetics, Polymer 47 (2006) 1-5.

[34] M.A. Alam, M. Takafuji, H. Ihara, Thermosensitive hybrid hydrogels with silica nanoparticle-cross-linked polymer networks, J. Colloid Interface Sci. 405 (2013) 109-117.

[35] Y. Wang, Z. Li, J. Wang, J. Li, Y. Lin, Graphene and graphene oxide: Biofunctionalization and applications in biotechnology, Trends Biotechnol. 29 (2011) 205-212.

[36] H. Shen, L. Zhang, M. Liu, Z. Zhang, Biomedical applications of graphene, Theranostics 2 (2012) 283-294.

[37] C. Chung, Y.-K. Kim, D. Shin, S.-R. Ryoo, B.H. Hong, D.-H. Min, Biomedical applications of graphene and graphene oxide, Acc. Chem. Res. 46 (2013) 2211-2224.

[38] Y. Shao, J. Wang, H. Wu, J. Liu, I.A. Aksay, Y. Lin, Graphene based electrochemical sensors and biosensors: A review, Electroanalysis 22 (2010) 1027-1036.

[39] C. Lee, X. Wei, J.W. Kysar, J. Hone, Measurement of the elastic properties and intrinsic strength of monolayer graphene, Science 321 (2008) 385-388.

[40] J.W. Suk, R.D. Piner, J. An, R.S. Ruoff, Mechanical properties of monolayer graphene oxide, ACS Nano 4 (2010) 6557-6564.

[41] K. Kabiri, M.J. Zohuriaan-Mehr, Superabsorbent hydrogel composites, Polym. Adv. Technol. 14 (2003) 438-444.

[42] Y. Osada, J.P. Gong, Soft and wet materials: Polymer gels, Adv. Mater. 10 (1998) 827-837.

[43] W.E. Hennink, C.F. Van Nostrum, Novel crosslinking methods to design hydrogels, Adv. Drug Delivery Rev. 54 (2002) 13-36.

[44] A. Katchalsky, Rapid swelling and deswelling of reversible gels of polymeric acids by ionization, Experientia 5 (1949) 319-320.

[45] M.J. Zohuriaan-Mehr, K. Kabiri, Superabsorbent polymer materials: A review, Iran. Polym. J. 17 (2008) 451-477.

[46] M. Chehade, M.J. Elder, Intraocular lens materials and styles: A review, Aust. N. Z. J. Ophthalmol. 25 (1997) 255-263.

[47] C. Paquet, E. Kumacheva, Nanostructured polymers for photonics, Mater. Today 11 (2008) 48-56.

[48] C.D.H. Alarcon, S. Pennadam, C. Alexander, Stimuli responsive polymers for biomedical applications, Chem. Soc. Rev. 34 (2005) 276-285.

[49] R. Bashir, J.Z. Hilt, O. Elibol, A. Gupta, N.A. Peppas, Micromechanical cantilever as an ultrasensitive ph microsensor, Appl. Phys. Lett. 81 (2002) 3091-3093.

[50] N.A. Peppas, P. Bures, W. Leobandung, H. Ichikawa, Hydrogels in pharmaceutical formulations, Eur. J. Pharm. Biopharm. 50 (2000) 27-46.

[51] U. Hasegawa, S.I.M. Nomura, S.C. Kaul, T. Hirano, K. Akiyoshi, Nanogel-quantum dot hybrid nanoparticles for live cell imaging, Biochem. Biophys. Res. Commun. 331 (2005) 917-921.

[52] C.W. Peak, J.J. Wilker, G. Schmidt, A review on tough and sticky hydrogels, Colloid Polym. Sci. 291 (2013) 2031-2047.

[53] B.D. Boyan, C.H. Lohmann, J. Romero, Z. Schwartz, Bone and cartilage tissue engineering, Clin. Plast. Surg. 26 (1999) 629-645.

[54] J. Maitra, V.K. Shukla, Cross-linking in hydrogels-a review, Am. J. Polym. Sci. 4 (2014) 25-31.

[55] Y. Hirokawa, H. Jinnai, Y. Nishikawa, T. Okamoto, T. Hashimoto, Direct observation of internal structures in poly(N-isopropylacrylamide) chemical gels, Macromolecules 32 (1999) 7093-7099.

[56] J.P. Gong, Y. Katsuyama, T. Kurokawa, Y. Osada, Double-network hydrogels with extremely high mechanical strength, Adv. Mater. 15 (2003) 1155-1158.

[57] Y.H. Na, T. Kurokawa, Y. Katsuyama, H. Tsukeshiba, J.P. Gong, Y. Osada, S. Okabe, T. Karino, M. Shibayama, Structural characteristics of double network gels with extremely high mechanical strength, Macromolecules 37 (2004) 5370-5374.

[58] F. Yu, X. Cao, L. Zeng, Q. Zhang, X. Chen, An interpenetrating HA/G/CS biomimic hydrogel via Diels–Alder click chemistry for cartilage tissue engineering, Carbohydr. Polym. 97 (2013) 188-195.

[59] A. Nakayama, A. Kakugo, J.P. Gong, Y. Osada, M. Takai, T. Erata, S. Kawano, High mechanical strength double-network hydrogel with bacterial cellulose, Adv. Funct. Mater. 14 (2004) 1124-1128.

[60] H. Tsukeshiba, M. Huang, Y.H. Na, T. Kurokawa, R. Kuwabara, Y. Tanaka, H. Furukawa, Y. Osada, J.P. Gong, Effect of polymer entanglement on the toughening of double network hydrogels, J. Phys. Chem. B 109 (2005) 16304-16309.

[61] Y. Tanaka, R. Kuwabara, Y.-H. Na, T. Kurokawa, J.P. Gong, Y. Osada, Determination of fracture energy of high strength double network hydrogels, J. Phys. Chem. B 109 (2005) 11559-11562.

[62] Y.-H. Na, Y. Tanaka, Y. Kawauchi, H. Furukawa, T. Sumiyoshi, J.P. Gong, Y. Osada, Necking phenomenon of double-network gels, Macromolecules 39 (2006) 4641-4645.

[63] M. Huang, H. Furukawa, Y. Tanaka, T. Nakajima, Y. Osada, J.P. Gong, Importance of entanglement between first and second components in high-strength double network gels, Macromolecules 40 (2007) 6658-6664.

[64] T. Nakajima, T. Kurokawa, H. Furukawa, Q.M. Yu, Y. Tanaka, Y. Osada, J.P. Gong, Super tough gels with a double network structure, Chin. J. Polym. Sci. 27 (2009) 1-9.

[65] T. Nakajima, H. Furukawa, Y. Tanaka, T. Kurokawa, Y. Osada, J.P. Gong, True chemical structure of double network hydrogels, Macromolecules 42 (2009) 2184-2189.

[66] Y. Hagiwara, A. Putra, A. Kakugo, H. Furukawa, J.P. Gong, Ligament-like tough double-network hydrogel based on bacterial cellulose, Cellulose 17 (2010) 93-101.

[67] S. Ronken, D. Wirz, A. Daniels, T. Kurokawa, J. Gong, M. Arnold, Double-network acrylamide hydrogel compositions adapted to achieve cartilage-like dynamic stiffness, Biomech. Model. Mechanobiol. 12 (2013) 243-248.

[68] J.P. Gong, Why are double network hydrogels so tough?, Soft Matter 6 (2010) 2583-2590.

[69] M.A. Haque, T. Kurokawa, J.P. Gong, Super tough double network hydrogels and their application as biomaterials, Polymer 53 (2012) 1805-1822.

[70] L. Weng, A. Gouldstone, Y. Wu, W. Chen, Mechanically strong double network photocrosslinked hydrogels from N,N-dimethylacrylamide and glycidyl methacrylated hyaluronan, Biomaterials 29 (2008) 2153-2163.

[71] X.Y. Zhang, X.L. Guo, S.G. Yang, S.X. Tan, X.F. Li, H.J. Dai, X.L. Yu, X.L. Zhang, N. Weng, B. Jian, J. Xu, Double-network hydrogel with high mechanical strength prepared from two biocompatible polymers, J. Appl. Polym. Sci. 112 (2009) 3063-3070.

[72] B.J. Dekosky, N.H. Dormer, G.C. Ingavle, C.H. Roatch, J. Lomakin, M.S. Detamore, S.H. Gehrke, Hierarchically designed agarose and poly(ethylene glycol) interpenetrating network hydrogels for cartilage tissue engineering, Tissue Eng. Part C Methods 16 (2010) 1533-1542.

[73] T. Dai, X. Qing, H. Zhou, C. Shen, J. Wang, Y. Lu, Mechanically strong conducting hydrogels with special double-network structure, Synth. Met. 160 (2010) 791-796.

[74] H. Zhang, A. Qadeer, W. Chen, In situ gelable interpenetrating double network hydrogel formulated from binary components: Thiolated chitosan and oxidized dextran, Biomacromolecules 12 (2011) 1428-1437.

[75] X. Wang, H. Wang, H.R. Brown, Jellyfish gel and its hybrid hydrogels with high mechanical strength, Soft Matter 7 (2011) 211-219.

[76] Y. Okumura, K. Ito, The polyrotaxane gel: A topological gel by figure-of-eight cross-links, Adv. Mater. 13 (2001) 485-487.

[77] K. Ito, Novel cross-linking concept of polymer network: Synthesis, structure, and properties of slide-ring gels with freely movable junctions, Polym. J. 39 (2007) 489-499.

[78] T. Karino, Y. Okumura, K. Ito, M. Shibayama, Sans studies on spatial inhomogeneities of slide-ring gels, Macromolecules 37 (2004) 6177-6182.

[79] Y. Shinohara, K. Kayashima, Y. Okumura, C. Zhao, K. Ito, Y. Amemiya, Small-angle X-ray scattering study of the pulley effect of slide-ring gels, Macromolecules 39 (2006) 7386-7391.

[80] C. Katsuno, A. Konda, K. Urayama, T. Takigawa, M. Kidowaki, K. Ito, Pressure-responsive polymer membranes of slide-ring gels with movable cross-links, Adv. Mater. 25 (2013) 4636-4640.

[81] K. Kato, K. Inoue, M. Kidowaki, K. Ito, Organic-inorganic hybrid slide-ring gels: Polyrotaxanes consisting of polydimethylsiloxane and γ-cyclodextrin and subsequent topological cross-linking, Macromolecules 42 (2009) 7129-7136.

[82] A.B. Imran, T. Seki, T. Kataoka, M. Kidowaki, K. Ito, Y. Takeoka, Fabrication of mechanically improved hydrogels using a movable cross-linker based on vinyl modified polyrotaxane, Chem. Commun. (2008) 5227-5229.

[83] A.B. Imran, K. Esaki, H. Gotoh, T. Seki, K. Ito, Y. Sakai, Y. Takeoka, Extremely stretchable thermosensitive hydrogels by introducing slide-ring polyrotaxane cross-linkers and ionic groups into the polymer network, Nat. Commun. 5 (2014) 1-8.

[84] T. Huang, H. Xu, K. Jiao, L. Zhu, H.R. Brown, H. Wang, A novel hydrogel with high mechanical strength: A macromolecular microsphere composite hydrogel, Adv. Mater. 19 (2007) 1622-1626.

[85] J. Zhao, K. Jiao, J. Yang, C. He, H. Wang, Mechanically strong and thermosensitive macromolecular microsphere composite poly(N-isopropylacrylamide) hydrogels, Polymer 54 (2013) 1596-1602.

[86] F. Jiang, T. Huang, C. He, H.R. Brown, H. Wang, Interactions affecting the mechanical properties of macromolecular microsphere composite hydrogels, J. Phys. Chem. B 117 (2013) 13679-13687.

[87] C. He, K. Jiao, X. Zhang, M. Xiang, Z. Li, H. Wang, Nanoparticles, microgels and bulk hydrogels with very high mechanical strength starting from micelles, Soft Matter 7 (2011) 2943-2952.

[88] Y.-N. Sun, G.-R. Gao, G.-L. Du, Y.-J. Cheng, J. Fu, Super tough, ultrastretchable, and thermoresponsive hydrogels with functionalized triblock copolymer micelles as macro-cross-linkers, ACS Macro Lett. 3 (2014) 496-500.

[89] Y. Tan, K. Xu, P. Wang, W. Li, S. Sun, L. Dong, High mechanical strength and rapid response rate of poly(N-isopropyl acrylamide) hydrogel crosslinked by starch-based nanospheres, Soft Matter 6 (2010) 1467-1471.

[90] X. Qin, F. Zhao, Y. Liu, H. Wang, S. Feng, High mechanical strength hydrogels preparation using hydrophilic reactive microgels as crosslinking agents, Colloid Polym. Sci. 287 (2009) 621-625.

[91] Y.T. Wu, M.G. Xia, Q.Q. Fan, M.F. Zhu, Designable synthesis of nanocomposite hydrogels with excellent mechanical properties based on chemical cross-linked interactions, Chem. Commun. 46 (2010) 7790-7792.

[92] T. Sakai, T. Matsunaga, Y. Yamamoto, C. Ito, R. Yoshida, S. Suzuki, N. Sasaki, M. Shibayama, U.-I. Chung, Design and fabrication of a high-strength hydrogel with ideally homogeneous network structure from tetrahedron-like macromonomers, Macromolecules 41 (2008) 5379-5384.

[93] T. Matsunaga, T. Sakai, Y. Akagi, U.-I. Chung, M. Shibayama, Structure characterization of tetra-PEG gel by small-angle neutron scattering, Macromolecules 42 (2009) 1344-1351.

[94] T. Matsunaga, T. Sakai, Y. Akagi, U.-I. Chung, M. Shibayama, SANS and SLS studies on tetra-arm PEG gels in as-prepared and swollen states, Macromolecules 42 (2009) 6245-6252.

[95] Y. Akagi, T. Matsunaga, M. Shibayama, U.-I. Chung, T. Sakai, Evaluation of topological defects in tetra-PEG gels, Macromolecules 43 (2010) 488-493.

[96] T. Sakai, Y. Akagi, T. Matsunaga, M. Kurakazu, U.-I. Chung, M. Shibayama, Highly elastic and deformable hydrogel formed from tetra-arm polymers, Macromol. Rapid Commun. 31 (2010) 1954-1959.

[97] M. Fukasawa, T. Sakai, U.-I. Chung, K. Haraguchi, Synthesis and mechanical properties of a nanocomposite gel consisting of a tetra-PEG/clay network, Macromolecules 43 (2010) 4370-4378.

[98] V.V. Rostovtsev, L.G. Green, V.V. Fokin, K.B. Sharpless, A stepwise huisgen cycloaddition process: copper (I)-catalyzed regioselective "ligation" of azides and terminal alkynes, Angew. Chem. 114 (2002) 2708-2711.

[99] M. Malkoch, R. Vestberg, N. Gupta, L. Mespouille, P. Dubois, A.F. Mason, J.L. Hedrick, Q. Liao, C.W. Frank, K. Kingsbury, Synthesis of well-defined hydrogel networks using click chemistry, Chem. Commun. (2006) 2774-2776.

[100] M. Haque, G. Kamita, T. Kurokawa, K. Tsujii, J.P. Gong, Unidirectional alignment of lamellar bilayer in hydrogel: One-dimensional swelling, anisotropic modulus, and stress/strain tunable structural color, Adv. Mater. 22 (2010) 5110-5114.

[101] M.A. Haque, T. Kurokawa, G. Kamita, J.P. Gong, Lamellar bilayers as reversible sacrificial bonds to toughen hydrogel: Hysteresis, self-recovery, fatigue resistance, and crack blunting, Macromolecules 44 (2011) 8916-8924.

[102] J. Kopecek, J. Yang, Smart self-assembled hybrid hydrogel biomaterials, Angew. Chem. Int. Ed. 51 (2012) 7396-7417.

[103] S.K. Gulrez, G.O. Phillips, S. Al-Assaf, Hydrogels: Methods of preparation, characterisation and applications, InTech Open Access Publisher, 2011.

[104] K. Haraguchi, H.J. Li, Mechanical properties and structure of polymer-clay nanocomposite gels with high clay content, Macromolecules 39 (2006) 1898-1905.

[105] K. Haraguchi, H.J. Li, K. Matsuda, T. Takehisa, E. Elliott, Mechanism of forming organic/inorganic network structures during in-situ free-radical polymerization in PNIPA-clay nanocomposite hydrogels, Macromolecules 38 (2005) 3482-3490.

[106] K. Haraguchi, T. Takehisa, S. Fan, Effects of clay content on the properties of nanocomposite hydrogels composed of poly(N-isopropylacrylamide) and clay, Macromolecules 35 (2002) 10162-10171.

[107] Y. Kaneko, K. Noguchi, J.-I. Kadokawa, Synthesis of temperature-responsive organic-inorganic hybrid hydrogel by free-radical polymerization of methacrylamide using water-soluble rigid polysiloxane having acryamido side-chains as a cross-linking agent, Polym. J. 39 (2007) 1078-1081.

[108] W.F. Lee, Y.C. Chen, Effect of intercalated hydrotalcite on swelling and mechanical behavior for poly(acrylic acid-co-N-isopropylacrylamide)/hydrotalcite nanocomposite hydrogels, J. Appl. Polym. Sci. 98 (2005) 1572-1580.

[109] K. Haraguchi, K. Uyama, H. Tanimoto, Self-healing in nanocomposite hydrogels, Macromol. Rapid Commun. 32 (2011) 1253-1258.

[110] G. Jiang, C. Liu, X. Liu, G. Zhang, M. Yang, F. Liu, Construction and properties of hydrophobic association hydrogels with high mechanical strength and reforming capability, Macromol. Mater. Eng. 294 (2009) 815-820.

[111] G. Jiang, C. Liu, X. Liu, Q. Chen, G. Zhang, M. Yang, F. Liu, Network structure and compositional effects on tensile mechanical properties of hydrophobic association hydrogels with high mechanical strength, Polymer 51 (2010) 1507-1515.

[112] G.Q. Jiang, C. Liu, X.L. Liu, G.H. Zhang, M. Yang, Q.R. Chen, F.Q. Liu, Self-healing mechanism and mechanical behavior of hydrophobic association hydrogels with high mechanical strength, J. Macromol. Sci. Part A Pure Appl. Chem. 47 (2010) 335-342.

[113] M. Yang, C. Liu, Z. Li, G. Gao, F. Liu, Temperature-responsive properties of poly(acrylic acid-co-acrylamide) hydrophobic association hydrogels with high mechanical strength, Macromolecules 43 (2010) 10645-10651.

[114] G. Jiang, C. Liu, X. Liu, G. Zhang, M. Yang, Q. Chen, F. Liu, Swelling behavior of hydrophobic association hydrogels with high mechanical strength, J. Macromol. Sci., A 47 (2010) 663-670.

[115] D.C. Tuncaboylu, M. Sari, W. Oppermann, O. Okay, Tough and self-healing hydrogels formed via hydrophobic interactions, Macromolecules 44 (2011) 4997-5005.

[116] D.C. Tuncaboylu, A. Argun, M. Sahin, M. Sari, O. Okay, Structure optimization of self-healing hydrogels formed via hydrophobic interactions, Polymer 53 (2012) 5513-5522.

[117] D.C. Tuncaboylu, M. Sahin, A. Argun, W. Oppermann, O. Okay, Dynamics and large strain behavior of self-healing hydrogels with and without surfactants, Macromolecules 45 (2012) 1991-2000.

[118] W. Li, H. An, Y. Tan, C. Lu, C. Liu, P. Li, K. Xu, P. Wang, Hydrophobically associated hydrogels based on acrylamide and anionic surface active monomer with high mechanical strength, Soft Matter 8 (2012) 5078-5086.

[119] S.R. Stauffer, N.A. Peppas, Poly(vinyl alcohol) hydrogels prepared by freezing-thawing cyclic processing, Polymer 33 (1992) 3932-3936.

[120] F. Yokoyama, I. Masada, K. Shimamura, T. Ikawa, K. Monobe, Morphology and structure of highly elastic poly(vinyl alcohol) hydrogel prepared by repeated freezing-and-melting, Colloid Polym. Sci. 264 (1986) 595-601.

[121] N.A. Peppas, S.R. Stauffer, Reinforced uncrosslinked poly(vinyl alcohol) gels produced by cyclic freezing-thawing processes: A short review, J.Controlled Release 16 (1991) 305-310.

[122] J.A. Stammen, S. Williams, D.N. Ku, R.E. Guldberg, Mechanical properties of a novel PVA hydrogel in shear and unconfined compression, Biomaterials 22 (2001) 799-806.

[123] K. Kawanishi, M. Komatsu, T. Inoue, Thermodynamic consideration of the sol-gel transition in polymer solutions, Polymer 28 (1987) 980-984.

[124] T. Hatakeyama, A. Yamauchi, H. Hatakeyama, Effect of thermal hysteresis on structural change of water restrained in poly(vinyl alcohol) pseudo-gel, Eur. Polym. J. 23 (1987) 361-365.

[125] J.K. Li, N. Wang, X.S. Wu, Poly(vinyl alcohol) nanoparticles prepared by freezing-thawing process for protein/peptide drug delivery, J. Controlled Release 56 (1998) 117-126.

[126] C.M. Hassan, N.A. Peppas, Cellular PVA hydrogels produced by freeze/thawing, J. Appl. Polym. Sci. 76 (2000) 2075-2079.

[127] X. Tong, J. Zheng, Y. Lu, Z. Zhang, H. Cheng, Swelling and mechanical behaviors of carbon nanotube/poly(vinyl alcohol) hybrid hydrogels, Mater. Lett. 61 (2007) 1704-1706.

[128] M. Kokabi, M. Sirousazar, Z.M. Hassan, PVA-clay nanocomposite hydrogels for wound dressing, Eur. Polym. J. 43 (2007) 773-781.

[129] L. Zhang, Z. Wang, C. Xu, Y. Li, J. Gao, W. Wang, Y. Liu, High strength graphene oxide/poly(vinyl alcohol) composite hydrogels, J. Mater. Chem. 21 (2011) 10399-10406.

[130] K.J. Henderson, T.C. Zhou, K.J. Otim, K.R. Shull, Ionically cross-linked triblock copolymer hydrogels with high strength, Macromolecules 43 (2010) 6193-6201.

[131] Y.-H. Lin, H.-F. Liang, C.-K. Chung, M.-C. Chen, H.-W. Sung, Physically crosslinked alginate/N,O-carboxymethyl chitosan hydrogels with calcium for oral delivery of protein drugs, Biomaterials 26 (2005) 2105-2113.

[132] H.-R. Lin, M.-H. Ling, Y.-J. Lin, High strength and low friction of a PAA-alginate-silica hydrogel as potential material for artificial soft tissues, J. Biomater. Sci., Polym. Ed. 20 (2009) 637-652.

[133] J.-Y. Sun, X. Zhao, W.R. Illeperuma, O. Chaudhuri, K.H. Oh, D.J. Mooney, J.J. Vlassak, Z. Suo, Highly stretchable and tough hydrogels, Nature 489 (2012) 133-136.

[134] T.L. Sun, T. Kurokawa, S. Kuroda, A.B. Ihsan, T. Akasaki, K. Sato, M.A. Haque, T. Nakajima, J.P. Gong, Physical hydrogels composed of polyampholytes demonstrate high toughness and viscoelasticity, Nat. Mater. 12 (2013) 932-937.

[135] A.K. Geim, K.S. Novoselov, The rise of graphene, Nat. Mater. 6 (2007) 183-191.

[136] D. Chung, Review graphite, J. Mater. Sci. 37 (2002) 1475-1489.

[137] K.S. Novoselov, A.K. Geim, S.V. Morozov, D. Jiang, Y. Zhang, S.V. Dubonos, I.V. Grigorieva, A.A. Firsov, Electric field effect in atomically thin carbon films, Science 306 (2004) 666-669.

[138] M.D. Stoller, S. Park, Y. Zhu, J. An, R.S. Ruoff, Graphene-based ultracapacitors, Nano Lett. 8 (2008) 3498-3502.

[139] A.A. Balandin, S. Ghosh, W. Bao, I. Calizo, D. Teweldebrhan, F. Miao, C.N. Lau, Superior thermal conductivity of single-layer graphene, Nano Lett. 8 (2008) 902-907.

[140] K.S. Kim, Y. Zhao, H. Jang, S.Y. Lee, J.M. Kim, K.S. Kim, J.-H. Ahn, P. Kim, J.-Y. Choi, B.H. Hong, Large-scale pattern growth of graphene films for stretchable transparent electrodes, Nature 457 (2009) 706-710.

[141] Y. Hernandez, V. Nicolosi, M. Lotya, F.M. Blighe, Z. Sun, S. De, I. Mcgovern, B. Holland, M. Byrne, Y.K. Gun'ko, High-yield production of graphene by liquid-phase exfoliation of graphite, Nat. Nanotech. 3 (2008) 563-568.

[142] D.R. Dreyer, S. Park, C.W. Bielawski, R.S. Ruoff, The chemistry of graphene oxide, Chem. Soc. Rev. 39 (2010) 228-240.

[143] S. Park, R.S. Ruoff, Chemical methods for the production of graphenes, Nat. Nanotech. 4 (2009) 217-224.
[144] S. Mao, H. Pu, J. Chen, Graphene oxide and its reduction: Modeling and experimental progress, RSC Adv. 2 (2012) 2643-2662.
[145] C. Soldano, A. Mahmood, E. Dujardin, Production, properties and potential of graphene, Carbon 48 (2010) 2127-2150.
[146] O.C. Compton, S.T. Nguyen, Graphene oxide, highly reduced graphene oxide, and graphene: Versatile building blocks for carbon-based materials, Small 6 (2010) 711-723.
[147] P. Wei, W. Bao, Y. Pu, C.N. Lau, J. Shi, Anomalous thermoelectric transport of dirac particles in graphene, Phys. Rev. Lett. 102 (2009) 166808 (1-16).
[148] J. Zhu, M. Chen, Q. He, L. Shao, S. Wei, Z. Guo, An overview of the engineered graphene nanostructures and nanocomposites, RSC Adv. 3 (2013) 22790-22824.
[149] A. Lerf, H.Y. He, M. Forster, J. Klinowski, Structure of graphite oxide revisited, J. Phys. Chem. B 102 (1998) 4477-4482.
[150] B.C. Brodie, On the atomic weight of graphite, Philos. Trans. R. Soc. 149 (1859) 249-259.
[151] L. Staudenmaier, Method for the preparation of graphitic acid, Ber. Dtsch. Chem. Ges. 31 (1898) 1481-1487.
[152] W.S. Hummers, R.E. Offeman, Preparation of graphitic oxide, J. Am. Chem. Soc. 80 (1958) 1339-1339.
[153] M. Mermoux, Y. Chabre, Formation of graphite oxide, Synth. Met. 34 (1989) 157-162.
[154] T. Nakajima, Y. Matsuo, Formation process and structure of graphite oxide, Carbon 32 (1994) 469-475.
[155] D.C. Marcano, D.V. Kosynkin, J.M. Berlin, A. Sinitskii, Z.Z. Sun, A. Slesarev, L.B. Alemany, W. Lu, J.M. Tour, Improved synthesis of graphene oxide, ACS Nano 4 (2010) 4806-4814.
[156] F. Kim, L.J. Cote, J. Huang, Graphene oxide: Surface activity and two-dimensional assembly, Adv. Mater. 22 (2010) 1954-1958.
[157] A. Sahu, W.I. Choi, G. Tae, A stimuli-sensitive injectable graphene oxide composite hydrogel, Chem. Commun. 48 (2012) 5820-5822.
[158] Y. Zhang, T.R. Nayak, H. Hong, W. Cai, Graphene: A versatile nanoplatform for biomedical applications, Nanoscale 4 (2012) 3833-3842.

[159] K.-H. Liao, Y.-S. Lin, C.W. Macosko, C.L. Haynes, Cytotoxicity of graphene oxide and graphene in human erythrocytes and skin fibroblasts, ACS Appl. Mater. Interfaces 3 (2011) 2607-2615.

[160] O.N. Ruiz, K.S. Fernando, B. Wang, N.A. Brown, P.G. Luo, N.D. Mcnamara, M. Vangsness, Y.-P. Sun, C.E. Bunker, Graphene oxide: A nonspecific enhancer of cellular growth, ACS Nano 5 (2011) 8100-8107.

[161] A. Sasidharan, L.S. Panchakarla, P. Chandran, D. Menon, S. Nair, C.N.R. Rao, M. Koyakutty, Differential nano-bio interactions and toxicity effects of pristine versus functionalized graphene, Nanoscale 3 (2011) 2461-2464.

[162] J. Kim, Y.-R. Kim, Y. Kim, K.T. Lim, H. Seonwoo, S. Park, S.-P. Cho, B.H. Hong, P.-H. Choung, T.D. Chung, Graphene-incorporated chitosan substrata for adhesion and differentiation of human mesenchymal stem cells, J. Mater. Chem. B 1 (2013) 933-938.

[163] K.P. Liu, J.J. Zhang, F.F. Cheng, T.T. Zheng, C.M. Wang, J.J. Zhu, Green and facile synthesis of highly biocompatible graphene nanosheets and its application for cellular imaging and drug delivery, J. Mater. Chem. 21 (2011) 12034-12040.

[164] K. Yang, S. Zhang, G. Zhang, X. Sun, S.-T. Lee, Z. Liu, Graphene in mice: Ultrahigh in vivo tumor uptake and efficient photothermal therapy, Nano Lett. 10 (2010) 3318-3323.

[165] K. Yang, J. Wan, S. Zhang, Y. Zhang, S.-T. Lee, Z. Liu, In vivo pharmacokinetics, long-term biodistribution, and toxicology of pegylated graphene in mice, ACS Nano 5 (2010) 516-522.

[166] K. Yang, H. Gong, X. Shi, J. Wan, Y. Zhang, Z. Liu, In vivo biodistribution and toxicology of functionalized nano-graphene oxide in mice after oral and intraperitoneal administration, Biomaterials 34 (2013) 2787-2795.

[167] V. Alzari, D. Nuvoli, S. Scognamillo, M. Piccinini, E. Gioffredi, G. Malucelli, S. Marceddu, M. Sechi, V. Sanna, A. Mariani, Graphene-containing thermoresponsive nanocomposite hydrogels of poly(N-isopropylacrylamide) prepared by frontal polymerization, J. Mater. Chem. 21 (2011) 8727-8733.

[168] Y.X. Xu, K.X. Sheng, C. Li, G.Q. Shi, Self-assembled graphene hydrogel via a one-step hydrothermal process, ACS Nano 4 (2010) 4324-4330.

[169] Y. Xu, X. Huang, Z. Lin, X. Zhong, Y. Huang, X. Duan, One-step strategy to graphene/Ni(OH)2 composite hydrogels as advanced three-dimensional supercapacitor electrode materials, Nano Res. 6 (2013) 65-76.

[170] H. Wang, H. Yi, X. Chen, X. Wang, One-step strategy to three-dimensional graphene/VO2 nanobelt composite hydrogels for high performance supercapacitors, J. Mater. Chem. A 2 (2014) 1165-1173.

[171] S. Das, F. Irin, L. Ma, S.K. Bhattacharia, R.C. Hedden, M.J. Green, Rheology and morphology of pristine graphene/polyacrylamide gels, ACS Appl. Mater. Interfaces 5 (2013) 8633-8640.

[172] C. Hou, Y. Duan, Q. Zhang, H. Wang, Y. Li, Bio-applicable and electroactive near-infrared laser-triggered self-healing hydrogels based on graphene networks, J. Mater. Chem. 22 (2012) 14991-14996.

[173] H. Zhou, W. Yao, G. Li, J. Wang, Y. Lu, Graphene/poly(3, 4-ethylenedioxythiophene) hydrogel with excellent mechanical performance and high conductivity, Carbon (2013). 495-502.

[174] B. Adhikari, A. Banerjee, Short peptide based hydrogels: Incorporation of graphene into the hydrogel, Soft Matter 7 (2011) 9259-9266.

[175] Y. Wang, P. Zhang, C.F. Liu, C.Z. Huang, A facile and green method to fabricate graphene-based multifunctional hydrogels for miniature-scale water purification, RSC Adv. 3 (2013) 9240-9246.

[176] N. Zhang, R. Li, L. Zhang, H. Chen, W. Wang, Y. Liu, T. Wu, X. Wang, W. Wang, Y. Li, Y. Zhao, J. Gao, Actuator materials based on graphene oxide/polyacrylamide composite hydrogels prepared by in situ polymerization, Soft Matter 7 (2011) 7231-7239.

[177] Y. Huang, M. Zeng, J. Ren, J. Wang, L. Fan, Q. Xu, Preparation and swelling properties of graphene oxide/poly(acrylic acid-co-acrylamide) super-absorbent hydrogel nanocomposites, Colloids Surf. A 401 (2012) 97-106.

[178] W. Cai, R.D. Piner, F.J. Stadermann, S. Park, M.A. Shaibat, Y. Ishii, D. Yang, A. Velamakanni, S.J. An, M. Stoller, J. An, D. Chen, R.S. Ruoff, Synthesis and solid-state NMR structural characterization of 13C-labeled graphite oxide, Science 321 (2008) 1815-1817.

[179] V. Sridhar, I.K. Oh, A coagulation technique for purification of graphene sheets with graphene-reinforced PVA hydrogel as byproduct, J. Colloid Interface Sci. 348 (2010) 384-387.

[180] H. Bai, C. Li, X.L. Wang, G.Q. Shi, A pH-sensitive graphene oxide composite hydrogel, Chem. Commun. 46 (2010) 2376-2378.

[181] Y.X. Xu, Q.O. Wu, Y.Q. Sun, H. Bai, G.Q. Shi, Three-dimensional self-assembly of graphene oxide and DNA into multifunctional hydrogels, ACS Nano 4 (2010) 7358-7362.

[182] Y. Tabata, Y. Ikada, Protein release from gelatin matrices, Adv. Drug Delivery Rev. 31 (1998) 287-301.

[183] S.K. Samal, M. Dash, S. Van Vlierberghe, D.L. Kaplan, E. Chiellini, C. Van Blitterswijk, L. Moroni, P. Dubruel, Cationic polymers and their therapeutic potential, Chem. Soc. Rev. 41 (2012) 7147-7194.

[184] S. Young, M. Wong, Y. Tabata, A.G. Mikos, Gelatin as a delivery vehicle for the controlled release of bioactive molecules, J. Controlled Release 109 (2005) 256-274.

[185] D. Liu, M. Nikoo, G. Boran, P. Zhou, J.M. Regenstein, Collagen and gelatin, in: Doyle MP and Klaenhammer TR, editors, Annual review of food science and technology, vol 6, 2015, pp. 527-557.

[186] K.B. Djagny, Z. Wang, S.Y. Xu, Gelatin: A valuable protein for food and pharmaceutical industries: Review, Crit. Rev. Food Sci. Nutr. 41 (2001) 481-492.

[187] J. Eastoe, The amino acid composition of mammalian collagen and gelatin, Biochem. J. 61 (1955) 589-600.

[188] J.M. Saddler, P.J. Horsey, The new generation gelatins, Anaesthesia 42 (1987) 998-1004.

[189] C. Wan, M. Frydrych, B. Chen, Strong and bioactive gelatin–graphene oxide nanocomposites, Soft Matter 7 (2011) 6159-6166.

[190] S. Faghihi, A. Karimi, M. Jamadi, R. Imani, R. Salarian, Graphene oxide/poly(acrylic acid)/gelatin nanocomposite hydrogel: Experimental and numerical validation of hyperelastic model, Mater. Sci. Eng. C 38 (2014) 299-305.

[191] S. Faghihi, M. Gheysour, A. Karimi, R. Salarian, Fabrication and mechanical characterization of graphene oxide-reinforced poly(acrylic acid)/gelatin composite hydrogels, J. Appl. Phys. 115 (2014) 083513 (1-6).

[192] S.R. Shin, B. Aghaei-Ghareh-Bolagh, T.T. Dang, S.N. Topkaya, X. Gao, S.Y. Yang, S.M. Jung, J.H. Oh, M.R. Dokmeci, X.S. Tang, Cell-laden microengineered and mechanically tunable hybrid hydrogels of gelatin and graphene oxide, Adv. Mater. 25 (2013) 6385-6391.

[193] D.A. Tomalia, A.M. Naylor, W.A. Goddard, Starburst dendrimers: Molecular-level control of size, shape, surface chemistry, topology, and flexibility from atoms to macroscopic matter, Angew. Chem. Int. Ed. 29 (1990) 138-175.

[194] D.A. Tomalia, Birth of a new macromolecular architecture: Dendrimers as quantized building blocks for nanoscale synthetic polymer chemistry, Prog. Polym. Sci. 30 (2005) 294-324.

[195] S. Svenson, Dendrimers as versatile platform in drug delivery applications, Eur. J. Pharm. Biopharm. 71 (2009) 445-462.

[196] M.A. Mintzer, M.W. Grinstaff, Biomedical applications of dendrimers: A tutorial, Chem. Soc. Rev. 40 (2011) 173-190.

[197] N. Joshi, M. Grinstaff, Applications of dendrimers in tissue engineering, Curr. Top. Med. Chem. 8 (2008) 1225-1236.

[198] A.R. Menjoge, R.M. Kannan, D.A. Tomalia, Dendrimer-based drug and imaging conjugates: Design considerations for nanomedical applications, Drug Discov. Today 15 (2010) 171-185.

[199] L.Y. Qiu, Y.H. Bae, Polymer architecture and drug delivery, Pharm. Res. 23 (2006) 1-30.

[200] D.A. Tomalia, H. Baker, J. Dewald, M. Hall, G. Kallos, S. Martin, J. Roeck, J. Ryder, P. Smith, A new class of polymers: starburst-dendritic macromolecules, Polym. J. 17 (1985) 117-132.

[201] D.A. Tomalia, H. Baker, J. Dewald, M. Hall, G. Kallos, S. Martin, J. Roeck, J. Ryder, P. Smith, Dendritic macromolecules: synthesis of starburst dendrimers, Macromolecules 19 (1986) 2466-2468.

[202] C.J. Hawker, J.M.J. Frechet, Preparation of polymers with controlled molecular architecture. A new convergent approach to dendritic macromolecules, J. Am. Chem. Soc. 112 (1990) 7638-7647.

[203] S.K. Choi, T.P. Thomas, M.-H. Li, A. Desai, A. Kotlyar, J.R. Baker, Photochemical release of methotrexate from folate receptor-targeting PAMAM dendrimer nanoconjugate, Photoch. Photobio. Sci. 11 (2012) 653-660.

[204] M. Labieniec, C. Watala, PAMAM dendrimers-Diverse biomedical applications. Facts and unresolved questions, Cent. Eur. J. Biol. 4 (2009) 434-451.

[205] E.B. Bahadır, M.K. Sezgintürk, Polyamidoamine (PAMAM): An emerging material for electrochemical bio(sensing) applications, Talanta 148 (2016) 427-438.

[206] R. Esfand, D.A. Tomalia, Polyamidoamine (PAMAM) dendrimers: From biomimicry to drug delivery and biomedical applications, Drug Discov. Today 6 (2001) 427-436.

[207] D.R. Radu, C.-Y. Lai, K. Jeftinija, E.W. Rowe, S. Jeftinija, V.S.-Y. Lin, A polyamidoamine dendrimer-capped mesoporous silica nanosphere-based gene transfection reagent, J. Am. Chem. Soc. 126 (2004) 13216-13217.

[208] R. Duncan, L. Izzo, Dendrimer biocompatibility and toxicity, Adv. Drug Delivery Rev. 57 (2005) 2215-2237.

[209] K. Jain, P. Kesharwani, U. Gupta, N.K. Jain, Dendrimer toxicity: Let's meet the challenge, Int. J. Pharm. 394 (2010) 122-142.

[210] Y. Cheng, L. Zhao, Y. Li, T. Xu, Design of biocompatible dendrimers for cancer diagnosis and therapy: Current status and future perspectives, Chem. Soc. Rev. 40 (2011) 2673-2703.

[211] S. Zhong, L.Y.L. Yung, Enhanced biological stability of collagen with incorporation of PAMAM dendrimer, J. Biomed. Mater. Res. A 91 (2009) 114-122.

[212] P.N. Desai, Q. Yuan, H. Yang, Synthesis and characterization of photocurable polyamidoamine dendrimer hydrogels as a versatile platform for tissue engineering and drug delivery, Biomacromolecules 11 (2010) 666-673.

[213] H. Yang, P. Tyagi, R.S. Kadam, C.A. Holden, U.B. Kompella, Hybrid dendrimer hydrogel/PLGA nanoparticle platform sustains drug delivery for one week and antiglaucoma effects for four days following one-time topical administration, ACS Nano 6 (2012) 7595-7606.

[214] T. Wu, X. Wang, H. Qiu, J. Gao, W. Wang, Y. Liu, Graphene oxide reduced and modified by soft nanoparticles and its catalysis of the knoevenagel condensation, J. Mater. Chem. 22 (2012) 4772-4779.

[215] J.M. Kim, J. Kim, J. Kim, Covalent decoration of graphene oxide with dendrimer-encapsulated nanoparticles for universal attachment of multiple nanoparticles on chemically converted graphene, Chem. Commun. 48 (2012) 9233-9235.

[216] Z. Luo, L. Yuwen, Y. Han, J. Tian, X. Zhu, L. Weng, L. Wang, Reduced graphene oxide/PAMAM–silver nanoparticles nanocomposite modified electrode for direct electrochemistry of glucose oxidase and glucose sensing, Biosens. Bioelectron. 36 (2012) 179-185.

[217] Y. Yuan, G. Zhang, Y. Li, G. Zhang, F. Zhang, X. Fan, Poly (amidoamine) modified graphene oxide as an efficient adsorbent for heavy metal ions, Polym. Chem. 4 (2013) 2164-2167.

[218] F. Zhang, B. Wang, S. He, R. Man, Preparation of graphene-oxide/polyamidoamine dendrimers and their adsorption properties toward some heavy metal ions, J. Chem. Eng. Data 59 (2014) 1719-1726.

[219] Y. Yu, L.C.X. De Andrade, L. Fang, J. Ma, W. Zhang, Y. Tang, Graphene oxide and hyperbranched polymer-toughened hydrogels with improved absorption properties and durability, J. Mater. Sci. 50 (2015) 3457-3466.

[220] X. Yang, Y. Tu, L. Li, S. Shang, X.-M. Tao, Well-dispersed chitosan/graphene oxide nanocomposites, ACS Appl. Mater. Interfaces 2 (2010) 1707-1713.

[221] R. Justin, B. Chen, Characterisation and drug release performance of biodegradable chitosan–graphene oxide nanocomposites, Carbohydr. Polym. 103 (2014) 70-80.

[222] V.K. Rana, M.-C. Choi, J.-Y. Kong, G.Y. Kim, M.J. Kim, S.-H. Kim, S. Mishra, R.P. Singh, C.-S. Ha, Synthesis and drug-delivery behavior of chitosan-functionalized graphene oxide hybrid nanosheets, Macromol. Mater. Eng. 296 (2011) 131-140.

[223] R. Justin, B. Chen, Body temperature reduction of graphene oxide through chitosan functionalisation and its application in drug delivery, Mater. Sci. Eng. C 34 (2014) 50-53.

[224] Y. Chen, L. Chen, H. Bai, L. Li, Graphene oxide–chitosan composite hydrogels as broad-spectrum adsorbents for water purification, J. Mater. Chem. A 1 (2013) 1992-2001.

[225] D. Han, L. Yan, Supramolecular hydrogel of chitosan in the presence of graphene oxide nanosheets as 2D cross-linkers, ACS Sustainable Chem. Eng. 2 (2013) 296-300.

[226] S. Sayyar, E. Murray, B. Thompson, J. Chung, D.L. Officer, S. Gambhir, G.M. Spinks, G.G. Wallace, Processable conducting graphene/chitosan hydrogels for tissue engineering, J. Mater. Chem. B 3 (2015) 481-490.

[227] Y.M. Chen, J.J. Yang, J.P. Gong, Adhesion, spreading, and proliferation of endothelial cells on charged hydrogels, J. Adhes. 85 (2009) 839-868.

[228] T. Szabó, O. Berkesi, P. Forgó, K. Josepovits, Y. Sanakis, D. Petridis, I. Dékány, Evolution of surface functional groups in a series of progressively oxidized graphite oxides, Chem. Mater. 18 (2006) 2740-2749.

[229] J. Shen, Y. Hu, M. Shi, X. Lu, C. Qin, C. Li, M. Ye, Fast and facile preparation of graphene oxide and reduced graphene oxide nanoplatelets, Chem. Mater. 21 (2009) 3514-3520.

[230] A. Gupta, G. Chen, P. Joshi, S. Tadigadapa, P. Eklund, Raman scattering from high-frequency phonons in supported n-graphene layer films, Nano Lett. 6 (2006) 2667-2673.

[231] M.J. Mcallister, J.-L. Li, D.H. Adamson, H.C. Schniepp, A.A. Abdala, J. Liu, M. Herrera-Alonso, D.L. Milius, R. Car, R.K. Prud'homme, Single sheet functionalized graphene by oxidation and thermal expansion of graphite, Chem. Mater. 19 (2007) 4396-4404.

[232] J. Shen, B. Yan, T. Li, Y. Long, N. Li, M. Ye, Study on graphene-oxide-based polyacrylamide composite hydrogels, Composites Part A 43 (2012) 1476-1481.

[233] J. Paredes, S. Villar-Rodil, A. Martinez-Alonso, J. Tascon, Graphene oxide dispersions in organic solvents, Langmuir 24 (2008) 10560-10564.

[234] T. Yang, L.-H. Liu, J.-W. Liu, M.-L. Chen, J.-H. Wang, Cyanobacterium metallothionein decorated graphene oxide nanosheets for highly selective adsorption of ultra-trace cadmium, J. Mater. Chem. 22 (2012) 21909-21916.

[235] J. Oh, J.-H. Lee, J.C. Koo, H.R. Choi, Y. Lee, T. Kim, N.D. Luong, J.-D. Nam, Graphene oxide porous paper from amine-functionalized poly(glycidyl methacrylate)/graphene oxide core-shell microspheres, J. Mater. Chem. 20 (2010) 9200-9204.

[236] S. Kim, M.E. Nimni, Z. Yang, B. Han, Chitosan/gelatin–based films crosslinked by proanthocyanidin, J. Biomed. Mater. Res. B: Appl. Biomater. 75 (2005) 442-450.

[237] J. An, Y. Gou, C. Yang, F. Hu, C. Wang, Synthesis of a biocompatible gelatin functionalized graphene nanosheets and its application for drug delivery, Mater. Sci. Eng. C, Mater. Biol. Appl. 33 (2013) 2827-2837.

[238] A.B. Bourlinos, D. Gournis, D. Petridis, T. Szabó, A. Szeri, I. Dékány, Graphite oxide: Chemical reduction to graphite and surface modification with primary aliphatic amines and amino acids, Langmuir 19 (2003) 6050-6055.

[239] S. Park, D.A. Dikin, S.T. Nguyen, R.S. Ruoff, Graphene oxide sheets chemically cross-linked by polyallylamine, J. Phys. Chem. C 113 (2009) 15801-15804.

[240] F. Tuinstra, J.L. Koenig, Raman spectrum of graphite, J. Chem. Phys. 53 (1970) 1126-1130.

[241] A.C. Ferrari, Raman spectroscopy of graphene and graphite: Disorder, electron–phonon coupling, doping and nonadiabatic effects, Solid State Commun. 143 (2007) 47-57.

[242] S. Berciaud, S. Ryu, L.E. Brus, T.F. Heinz, Probing the intrinsic properties of exfoliated graphene: Raman spectroscopy of free-standing monolayers, Nano Lett. 9 (2008) 346-352.

[243] K.N. Kudin, B. Ozbas, H.C. Schniepp, R.K. Prud'homme, I.A. Aksay, R. Car, Raman spectra of graphite oxide and functionalized graphene sheets, Nano Lett. 8 (2008) 36-41.

[244] A.C. Ferrari, J. Robertson, Interpretation of Raman spectra of disordered and amorphous carbon, Phys. Rev. B 61 (2000) 14095-14107.

[245] R.J. Nemanich, S.A. Solin, First- and second-order Raman scattering from finite-size crystals of graphite, Phys. Rev. B 20 (1979) 392-401.

[246] D.A. Dikin, S. Stankovich, E.J. Zimney, R.D. Piner, G.H. Dommett, G. Evmenenko, S.T. Nguyen, R.S. Ruoff, Preparation and characterization of graphene oxide paper, Nature 448 (2007) 457-460.

[247] C. Huang, H. Bai, C. Li, G. Shi, A graphene oxide/hemoglobin composite hydrogel for enzymatic catalysis in organic solvents, Chem. Commun. 47 (2011) 4962-4964.

[248] T. Kataoka, M. Kidowaki, C. Zhao, H. Minamikawa, T. Shimizu, K. Ito, Local and network structure of thermoreversible polyrotaxane hydrogels based on poly(ethylene glycol) and methylated α-cyclodextrins, J. Phys. Chem. B 110 (2006) 24377-24383.

[249] D. Burgess, J. Carless, Microelectrophoretic studies of gelatin and acacia for the prediction of complex coacervation, J. Colloid Interface Sci. 98 (1984) 1-8.

[250] S. Haider, S.-Y. Park, K. Saeed, B.L. Farmer, Swelling and electroresponsive characteristics of gelatin immobilized onto multi-walled carbon nanotubes, Sens. Actuator B-Chem. 124 (2007) 517-528.

[251] L.R.G. Treloar, The physics of rubber elasticity, 3rd ed., Clarendon Press, Oxford, 1975.

[252] J. Sabbagh, J. Vreven, G. Leloup, Dynamic and static moduli of elasticity of resin-based materials, Dent. Mater. 18 (2002) 64-71.

[253] T.K.L. Meyvis, B.G. Stubbe, M.J. Van Steenbergen, W.E. Hennink, S.C. De Smedt, J. Demeester, A comparison between the use of dynamic mechanical analysis and oscillatory shear rheometry for the characterisation of hydrogels, Int. J. Pharm. 244 (2002) 163-168.

[254] C.W. Macosko, R.G. Larson, Rheology: Principles, measurements, and applications, Wiley-VCH Publishers, New York, 1994.

[255] C.-C. Lin, A.T. Metters, Hydrogels in controlled release formulations: Network design and mathematical modeling, Adv. Drug Delivery Rev. 58 (2006) 1379-1408.

[256] R. Censi, T. Vermonden, M.J. Van Steenbergen, H. Deschout, K. Braeckmans, S.C. De Smedt, C.F. Van Nostrum, P. Di Martino, W. Hennink, Photopolymerized thermosensitive hydrogels for tailorable diffusion-controlled protein delivery, J. Controlled Release 140 (2009) 230-236.

[257] A. Montembault, C. Viton, A. Domard, Rheometric study of the gelation of chitosan in aqueous solution without cross-linking agent, Biomacromolecules 6 (2005) 653-662.

[258] C. Yan, D.J. Pochan, Rheological properties of peptide-based hydrogels for biomedical and other applications, Chem. Soc. Rev. 39 (2010) 3528-3540.

[259] S. Miyazaki, H. Endo, T. Karino, K. Haraguchi, M. Shibayama, Gelation mechanism of poly(N-isopropylacrylamide)-clay nanocomposite gels, Macromolecules 40 (2007) 4287-4295.

[260] A. Malkin, S. Ilyin, T. Roumyantseva, V. Kulichikhin, Rheological evidence of gel formation in dilute polyacrylonitrile solutions, Macromolecules 46 (2012) 257-266.

[261] R. Justin, B. Chen, Strong and conductive chitosan–reduced graphene oxide nanocomposites for transdermal drug delivery, J. Mater. Chem. B 2 (2014) 3759-3770.

[262] B. Amsden, Solute diffusion within hydrogels. Mechanisms and models, Macromolecules 31 (1998) 8382-8395.

[263] D. Evans, G. Pye, R. Bramley, A. Clark, T. Dyson, J. Hardcastle, Measurement of gastrointestinal pH profiles in normal ambulant human subjects, Gut 29 (1988) 1035-1041.

[264] N.A. Peppas, K.M. Wood, J.O. Blanchette, Hydrogels for oral delivery of therapeutic proteins, Expert Opin. Biol. Ther. 4 (2004) 881-887.

[265] H. He, X. Cao, L.J. Lee, Design of a novel hydrogel-based intelligent system for controlled drug release, J. controlled release 95 (2004) 391-402.

[266] S. Kim, J.H. Kim, O. Jeon, I.C. Kwon, K. Park, Engineered polymers for advanced drug delivery, Eur. J. Pharm. Biopharm. 71 (2009) 420-430.

[267] Y. Tabata, A. Nagano, Y. Ikada, Biodegradation of hydrogel carrier incorporating fibroblast growth factor, Tissue Eng. 5 (1999) 127-138.

[268] O.C. Compton, D.A. Dikin, K.W. Putz, L.C. Brinson, S.T. Nguyen, Electrically conductive “alkylated” graphene paper via chemical reduction of amine-functionalized graphene oxide paper, Adv. Mater. 22 (2010) 892-896.

[269] J.S. Chung, E.J. Kim, S.H. Hur, The molecular level control of three-dimensional graphene oxide hydrogel structure by using various diamines, Chem. Eng. J. 246 (2014) 64-70.

[270] Y. Matsuo, T. Miyabe, T. Fukutsuka, Y. Sugie, Preparation and characterization of alkylamine-intercalated graphite oxides, Carbon 45 (2007) 1005-1012.

[271] Y.-P. Zhang, J.-J. Xu, Z.-H. Sun, C.-Z. Li, C.-X. Pan, Preparation of graphene and TiO2 layer by layer composite with highly photocatalytic efficiency, Prog. Nat. Sci. 21 (2011) 467-471.

[272] M. Mermoux, Y. Chabre, A. Rousseau, FTIR and 13C NMR study of graphite oxide, Carbon 29 (1991) 469-474.

[273] C. Yang, L. Xu, Y. Zhou, X. Zhang, X. Huang, M. Wang, Y. Han, M. Zhai, S. Wei, J. Li, A green fabrication approach of gelatin/CM-chitosan hybrid hydrogel for wound healing, Carbohydr. Polym. 82 (2010) 1297-1305.

[274] A.C. Ferrari, J.C. Meyer, V. Scardaci, C. Casiraghi, M. Lazzeri, F. Mauri, S. Piscanec, D. Jiang, K.S. Novoselov, S. Roth, A.K. Geim, Raman spectrum of graphene and graphene layers, Phys. Rev. Lett. 97 (2006) 187401 (1-4).

[275] K. Sato, R. Saito, Y. Oyama, J. Jiang, L. Can çado, M. Pimenta, A. Jorio, G.G. Samsonidze, G. Dresselhaus, M. Dresselhaus, D-band Raman intensity of graphitic materials as a function of laser energy and crystallite size, Chem. Phys. Lett. 427 (2006) 117-121.

[276] K.-X. Sheng, Y.-X. Xu, C. Li, G.-Q. Shi, High-performance self-assembled graphene hydrogels prepared by chemical reduction of graphene oxide, New Carbon Mater. 26 (2011) 9-15.

[277] S. Stankovich, D.A. Dikin, R.D. Piner, K.A. Kohlhaas, A. Kleinhammes, Y. Jia, Y. Wu, S.T. Nguyen, R.S. Ruoff, Synthesis of graphene-based nanosheets via chemical reduction of exfoliated graphite oxide, Carbon 45 (2007) 1558-1565.

[278] H.-K. Jeong, H.-J. Noh, J.-Y. Kim, M. Jin, C. Park, Y. Lee, X-ray absorption spectroscopy of graphite oxide, Europhys. Lett. 82 (2008) 67004 (1-5).

[279] A. Bigi, S. Panzavolta, K. Rubini, Relationship between triple-helix content and mechanical properties of gelatin films, Biomaterials 25 (2004) 5675-5680.

[280] E.-Y. Choi, T.H. Han, J. Hong, J.E. Kim, S.H. Lee, H.W. Kim, S.O. Kim, Noncovalent functionalization of graphene with end-functional polymers, J. Mater. Chem. 20 (2010) 1907-1912.

[281] D. Zhang, X. Liu, X. Wang, Green synthesis of graphene oxide sheets decorated by silver nanoprisms and their anti-bacterial properties, J. Inorg. Biochem. 105 (2011) 1181-1186.

[282] D. Li, M.B. Muller, S. Gilje, R.B. Kaner, G.G. Wallace, Processable aqueous dispersions of graphene nanosheets, Nat. Nanotechnol. 3 (2008) 101-105.

[283] G. Eda, J. Ball, C. Mattevi, M. Acik, L. Artiglia, G. Granozzi, Y. Chabal, T.D. Anthopoulos, M. Chhowalla, Partially oxidized graphene as a precursor to graphene, J. Mater. Chem. 21 (2011) 11217-11223.

[284] R. Larciprete, P. Lacovig, S. Gardonio, A. Baraldi, S. Lizzit, Atomic oxygen on graphite: Chemical characterization and thermal reduction, J. Phys. Chem. C 116 (2012) 9900-9908.

[285] J. Crank, The mathematics of diffusion, 2nd ed., Clarendon Press, Oxford, 1975.

[286] J.S. Choi, K. Nam, J.-Y. Park, J.-B. Kim, J.-K. Lee, J.-S. Park, Enhanced transfection efficiency of PAMAM dendrimer by surface modification with L-arginine, J. Controlled Release 99 (2004) 445-456.

[287] X. Shi, I. Bányai, M.T. Islam, W. Lesniak, D.Z. Davis, J.R. Baker, L.P. Balogh, Generational, skeletal and substitutional diversities in generation one polyamidoamine dendrimers, Polymer 46 (2005) 3022-3034.

[288] Y. Kim, A.M. Klutz, K.A. Jacobson, Systematic investigation of polyamidoamine dendrimers surface-modified with poly(ethylene glycol) for drug delivery applications: Synthesis, characterization, and evaluation of cytotoxicity, Bioconjugate Chem. 19 (2008) 1660-1672.

[289] X. Shi, W. Lesniak, M.T. Islam, M.C. Muñiz, L.P. Balogh, J.R. Baker, Comprehensive characterization of surface-functionalized polyamidoamine dendrimers with acetamide, hydroxyl, and carboxyl groups, Colloids Surf., A 272 (2006) 139-150.

[290] T. Szabó, E. Tombácz, E. Illés, I. Dékány, Enhanced acidity and pH-dependent surface charge characterization of successively oxidized graphite oxides, Carbon 44 (2006) 537-545.

[291] C. Petit, M. Seredych, T.J. Bandosz, Revisiting the chemistry of graphite oxides and its effect on ammonia adsorption, J. Mater. Chem. 19 (2009) 9176-9185.

[292] Y. Lin, J. Jin, M. Song, Preparation and characterisation of covalent polymer functionalized graphene oxide, J. Mater. Chem. 21 (2011) 3455-3461.

[293] P. Gautam, A.K. Gupta, A. Sharma, T. Gautam, Synthesis and analytical characterization of ester and amine terminated PAMAM dendrimers, Glob. J. Med. Res. 13 (2013) 7-15.

[294] A. Das, B. Chakraborty, A. Sood, Raman spectroscopy of graphene on different substrates and influence of defects, Bull. Mater. Sci. 31 (2008) 579-584.

[295] Z. Wei, D.E. Barlow, P.E. Sheehan, The assembly of single-layer graphene oxide and graphene using molecular templates, Nano Lett. 8 (2008) 3141-3145.

[296] C. Gómez-Navarro, R.T. Weitz, A.M. Bittner, M. Scolari, A. Mews, M. Burghard, K. Kern, Electronic transport properties of individual chemically reduced graphene oxide sheets, Nano Lett. 7 (2007) 3499-3503.

[297] J. Li, C.-Y. Liu, Y. Liu, Au/graphene hydrogel: Synthesis, characterization and its use for catalytic reduction of 4-nitrophenol, J. Mater. Chem. 22 (2012) 8426-8430.

[298] J. Liang, Y. Huang, L. Zhang, Y. Wang, Y. Ma, T. Guo, Y. Chen, Molecular-level dispersion of graphene into poly(vinyl alcohol) and effective reinforcement of their nanocomposites, Adv. Funct. Mater. 19 (2009) 2297-2302.

[299] M.D. Hager, P. Greil, C. Leyens, S. Van Der Zwaag, U.S. Schubert, Self-healing materials, Adv. Mater. 22 (2010) 5424-5430.

[300] K. Juby, C. Dwivedi, M. Kumar, S. Kota, H. Misra, P. Bajaj, Silver nanoparticle-loaded PVA/gum acacia hydrogel: Synthesis, characterization and antibacterial study, Carbohydr. Polym. 89 (2012) 906-913.

[301] N. Sheng, M.C. Boyce, D.M. Parks, G. Rutledge, J. Abes, R. Cohen, Multiscale micromechanical modeling of polymer/clay nanocomposites and the effective clay particle, Polymer 45 (2004) 487-506.

[302] K.Y. Lee, J.A. Rowley, P. Eiselt, E.M. Moy, K.H. Bouhadir, D.J. Mooney, Controlling mechanical and swelling properties of alginate hydrogels independently by cross-linker type and cross-linking density, Macromolecules 33 (2000) 4291-4294.

[303] Z. Zhao, X. Wang, J. Qiu, J. Lin, D. Xu, C.A. Zhang, M. Lv, X. Yang, Three-dimensional graphene-based hydrogel/aerogel materials, Rev. Adv. Mater. Sci. 36 (2014) 137-151.

[304] S.H. Ku, M. Lee, C.B. Park, Carbon-based nanomaterials for tissue engineering, Adv. Healthcare Mater. 2 (2013) 244-260.

[305] X. Huang, N. Hu, R. Gao, Y. Yu, Y. Wang, Z. Yang, E.S.-W. Kong, H. Wei, Y. Zhang, Reduced graphene oxide–polyaniline hybrid: Preparation, characterization and its applications for ammonia gas sensing, J. Mater. Chem. 22 (2012) 22488-22495.

[306] M.C. Chang, C.-C. Ko, W.H. Douglas, Preparation of hydroxyapatite-gelatin nanocomposite, Biomaterials 24 (2003) 2853-2862.

[307] N. Hu, L. Meng, R. Gao, Y. Wang, J. Chai, Z. Yang, E.S.-W. Kong, Y. Zhang, A facile route for the large scale fabrication of graphene oxide papers and their mechanical enhancement by cross-linking with glutaraldehyde, Nano-Micro Lett. 3 (2011) 215-222.

[308] S. Farris, J. Song, Q. Huang, Alternative reaction mechanism for the cross-linking of gelatin with glutaraldehyde, J. Agric. Food Chem. 58 (2009) 998-1003.

[309] C. Cha, S.R. Shin, X. Gao, N. Annabi, M.R. Dokmeci, X.S. Tang, A. Khademhosseini, Controlling mechanical properties of cell-laden hydrogels by covalent incorporation of graphene oxide, Small 10 (2014) 514-523.

[310] B. Chen, J.R. Evans, Impact strength of polymer-clay nanocomposites, Soft Matter 5 (2009) 3572-3584.

[311] J. Yang, C.-R. Han, J.-F. Duan, M.-G. Ma, X.-M. Zhang, F. Xu, R.-C. Sun, X.-M. Xie, Studies on the properties and formation mechanism of flexible nanocomposite hydrogels from cellulose nanocrystals and poly(acrylic acid), J. Mater. Chem. 22 (2012) 22467-22480.

[312] W.-C. Lin, W. Fan, A. Marcellan, D. Hourdet, C. Creton, Large strain and fracture properties of poly(dimethylacrylamide)/silica hybrid hydrogels, Macromolecules 43 (2010) 2554-2563.

Appendix 1. Supplemental figures

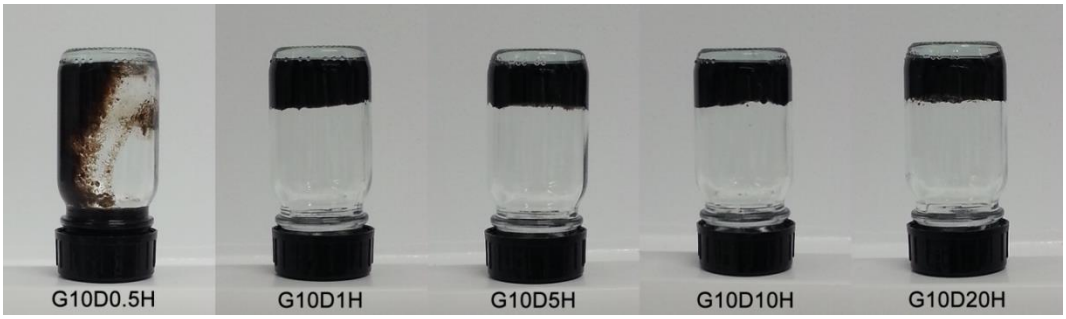

Figure 5.S1 Digital images of the G10D0.5H sol (instead of a hydrogel), and the successfully prepared GO-PAMAM nanocomposite hydrogels: G10D1H, G10D5H, G10D10H and G10D20H. The inner diameter of the container is 28 mm.

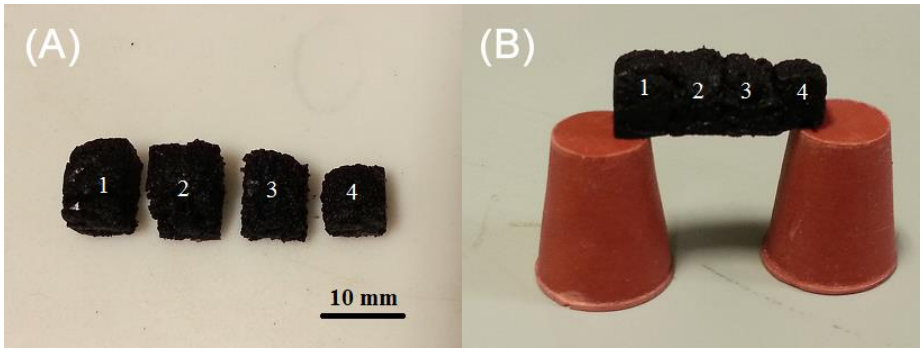

Figure 5.S2 (A) Four pieces of freshly cut free-standing hydrogel blocks; (B) the adhered four blocks can hang on horizontally showing self-healing ability. The hydrogel blocks self-healed after the freshly cut surfaces were gently pressed together and left for 10 min.